



저작자표시-비영리-변경금지 2.0 대한민국

이용자는 아래의 조건을 따르는 경우에 한하여 자유롭게

- 이 저작물을 복제, 배포, 전송, 전시, 공연 및 방송할 수 있습니다.

다음과 같은 조건을 따라야 합니다:



저작자표시. 귀하는 원저작자를 표시하여야 합니다.



비영리. 귀하는 이 저작물을 영리 목적으로 이용할 수 없습니다.



변경금지. 귀하는 이 저작물을 개작, 변형 또는 가공할 수 없습니다.

- 귀하는, 이 저작물의 재이용이나 배포의 경우, 이 저작물에 적용된 이용허락조건을 명확하게 나타내어야 합니다.
- 저작권자로부터 별도의 허가를 받으면 이러한 조건들은 적용되지 않습니다.

저작권법에 따른 이용자의 권리는 위의 내용에 의하여 영향을 받지 않습니다.

이것은 [이용허락규약\(Legal Code\)](#)을 이해하기 쉽게 요약한 것입니다.

[Disclaimer](#)

A THESIS
FOR THE DEGREE OF DOCTOR OF PHILOSOPHY

**Robust hydrophobic coating and deposition of carbon
thin layer for the electrode of energy storage devices
by using atmospheric pressure plasma**

Md. Mokter Hossain

Major of Energy & Chemical Engineering
FACULTY OF APPLIED ENERGY SYSTEM

GRADUATE SCHOOL
JEJU NATIONAL UNIVERSITY

February-- 2019

Robust hydrophobic coating and deposition of carbon thin layer for the electrode of energy storage devices by using atmospheric pressure plasma






Md. Mokter Hossain

(Supervised by Professor Young Sun Mok)

A thesis submitted in partial fulfillment of the requirement for the degree of
Doctor of Philosophy

2018. 11

The thesis has been examined and approved.

	
Prof. Ho Won Lee Thesis Director	Department of Chemical and Biological Engineering, Jeju National University
	
Prof. Sang Jae Kim Thesis Committee Member	Department of Chemical and Biological Engineering, Jeju National University
	
Dr. Iljeong Heo Thesis Committee Member	Korea Research Institute of Chemical Technology (KRICT)
	
Dr. Seung-geon Kim Thesis Committee Member	Department of Mechatronics Engineering, Jeju National University
	
Prof. Young Sun Mok Thesis Committee Member and Supervisor	Department of Chemical and Biological Engineering, Jeju National University

November, 2018

Major of Energy & Chemical Engineering

Plasma Application Laboratory

Faculty of Applied Energy System

Graduate School

Jeju National University



My humble effort
I
Dedicate
To the Father of the Nation
Bangabandhu Sheikh Mujibur Rahman
And
The people who sacrificed their lives in the
Liberation war of Bangladesh in 1971

Acknowledgment

“The highest education is that which does not merely give us information but makes our life in harmony with all existence.”

-----**Rabindranath Tagore**

First and foremost, I would like to thank my advisor Prof. Young Sun Mok for his fundamental role in my doctoral work. Prof. Mok provide me every moment of guidance, assistance, and skill that I needed during my first few semesters. He gave me the freedom to do whatever I wanted, at the same time continuing to contribute valuable feedback, advice, and encouragement. I appreciate all his contributions of time, ideas, and funding to make my Ph.D. experience productive and stimulating. I could not have imagined having a better advisor and mentor for my Ph.D. study.

I would like to thank the rest of my thesis committee members: Prof. Ho Won Lee, Prof. Sang-Jae Kim, Dr. IlJeong Heo, and Dr. Seung-gun Kim, for their valuable comments and encouragement. Once again, I thank to the committee members for their tough questions which incented me to widen my research from various perspectives.

I gratefully acknowledge the funding sources that made my Ph.D. work possible. I was funded by the BK21 that (Brain Korea 21 Program for Leading Universities & Students) is a human resource development program initiated by the Korean government. My work was also supported by the Scientific Promotion Program by Jeju National University.

The thesis would not have come to a successful completion, without the help I received from my colleagues, Dr. Quang Hung Trinh, Dr. Jin Oh Jo, Dr. M.S.P. Sudhakaran, Dr. Duc Nguyen, Mr. Byeong Ju Lee, Lamia Sultana, and all of my lab mates. They all have extended their

support in a very special way, and I gained a lot from them, through their personal and scholarly interactions, their suggestions at various points of my research programme.

I would like to thank people I met at Jeju. My life in Jeju was enjoyable due to the many friends and groups that became a part of my life. I am grateful for time spent with roommates and friends, for my backpacking buddies and our memorable trips into the Hallasan National Park, Seongsan Ilchulbong (Sunrise peak, Jeju).

Last but not the least, I would like to thank my family for all their love and inspiration. With love and respect, I would like to give my unconditional thank to my parents who supported me in each and every step of my study with their love and support. And most of all for my loving, supportive, encouraging, and patient wife Suraiya Akter whose faithful support during the final stages of this Ph.D. is so appreciated.

Above all, I owe it all to Almighty God for granting me the wisdom, health and strength to undertake this research work and allowing me to its completion. Thank you.

Md. Mokter Hossain
Jeju National University
November 2018

CONTENTS

Contents	i
List of Abbreviations	vii
List of Tables	ix
List of Figures	x
Abstract	xiv
CHAPTER-1	1
Literature review	1
1.1. Introduction and literature review	1
1.1.1. Plasma.....	1
1.1.2. Non-thermal plasma	2
1.1.3. Chemical activity of nonthermal plasma	7
1.2. Hydrophobicity, hydrophilicity, and silanes	8
1.2.1. Hydrophobicity and hydrophilicity	8
1.2.2. Theoretical background of hydrophobicity and hydrophilicity	10
1.2.2.1. Young's equation	10
1.2.2.2. Wenzel's equation.....	10
1.2.2.3. Cassie-Baxter's equation	11
1.2.3. Silanes.....	12
1.3. Energy storage devices.....	13

1.3.1. Supercapacitor	13
1.3.2. Energy storage mechanism and classification of supercapacitor	16
1.3.2.1. Electrochemical double layer capacitors (EDLCs) mechanism.....	17
1.3.2.2. Pseudocapacitors.....	19
1.3.2.3. Hybrid	19
1.4. References	20
CHAPTER-2.....	24
Materials, methods and characterization	24
2.1. Introduction	24
2.2. Materials and apparatus.....	25
2.2.1. Materials	25
2.2.2. Apparatus.....	26
2.3. Preparation of coating	27
2.4. Materials synthesis	27
2.5. Materials characterization	28
2.5.1. Atomic Force Microscopy (AFM).....	28
2.5.2. Field-emission scanning electron microscopy (FE-SEM).....	28
2.5.3. X-ray photoelectron spectroscopy (XPS)	29
2.4.4. Raman spectroscopy	30
2.4.5. X-ray diffraction (XRD).....	31

2.4.6. Fourier transform infrared (FT-IR) spectrometer (XRD).....	31
2.4.7. Flow controller units.....	32
2.4.8. Nano View 2400.....	33
CHAPTER-3.....	34
Robust hydrophobic coating on glass surface by an atmospheric-pressure plasma jet for plasma-polymerization of hexamethyldisiloxane conjugated with (3-aminopropyl) triethoxysilane	34
3.1. Introduction	35
3.2. Experimental	36
3.3. Results and discussion.....	40
3.3.1. Water contact angle measurements of the glass substrates	40
3.3.2. Coating stability test	44
3.3.3. Surface morphology and coating thickness	45
3.3.4. Surface modification by APTES	47
3.3.5. FTIR spectroscopy.....	49
3.3.6. XPS results	50
3.3.8. Scratch tests	54
3.4. Conclusions	56
3.5. References	57
CHAPTER-4.....	61

Improvement of mechanical strength of hydrophobic coating on glass surfaces by an atmospheric pressure plasma jet.....	61
4.1. Introduction	62
4.2. Experimental	63
4.3. Results and discussion.....	67
4.3.1. Hydrophobic treatment of glass and water contact angle measurement	67
4.3.2. Coating stability.....	70
4.3.3. Coating thickness and surface morphology.....	72
4.3.4. Gas-phase FTIR analysis	75
4.3.4.1. Gas-phase analysis of the effluent of the Ar/TMS plasma	75
4.3.4.2. Gas-phase analysis of the effluent of Ar/APTES plasma	77
4.3.4.3. Possible reaction routes and mechanism of APTES for the surface modification	77
4.3.5. FTIR analysis of the coating layer.....	79
4.3.6. XPS analysis	80
4.3.7. UV-Vis transmission spectra result	82
4.3.8. Scratch test.....	83
4.4. Conclusions	86
4.5. References	87
CHAPTER-5.....	92

Formation of plasma-polymerized superhydrophobic coating using an atmospheric-pressure plasma jet	92
5.1. Introduction	93
5.2. Experimental	94
5.2.1. Materials	94
5.2.2. Preparation of the plasma reactor and scratch tester	94
5.2.3. Preparation of coating.....	97
5.2.4. Characterizations	97
5.3. Results and discussion.....	98
5.3.1. Water contact angle measurements	98
5.3.2. Surface morphology and roughness	101
5.3.3. Stability tests.....	104
5.3.4. Spectroscopic analyses	105
5.3.5. Scratch test.....	110
5.4. Conclusions	113
5.5. References	114
CHAPTER-6.....	119
Preparation of carbon materials for the supercapacitor using non-thermal atmospheric-pressure plasma jet	119
6.1. Introduction	120

6.2. Experimental methodology	122
6.2.1. Deposition of plasma polymer coatings	122
6.2.2. Characterizations	124
6.3. Results and Discussion.....	125
5.3.1. Surface morphology and roughness	125
6.3.2. Raman shift.....	125
6.4. Conclusions	128
6.5. References	128
CHAPTER-7	131
Conclusion	131
APPENDIX A: List of Publications	133
APPENDIX B: List of Conferences	134

List of Abbreviations

AC	Alternating current
AFM	Atomic force microscopy
APTES	(3-Aminopropyl)triethoxysilane
APDMES	3-Aminopropyl(diethoxy)methylsilane
Ar	Argon
BE	Binding energy
CD	Corona discharge
CV	Cyclic voltammetry
DBD	Dielectric barrier discharge
DW	Distilled water
EDS	Energy dispersive X-ray Spectroscopy
FE-SEM	Field-emission scanning electron microscopy
FT	Fischer-Tropsch
FT-IR	Fourier Transform Infrared
HMDSO	Hexamethyldisiloxane
HV	High voltage
ID	Inner diameter
IR	Infrared
KBr	Potassium bromide
KV	Kilovolt
MFC	Mass flow controller
NiF	Nickel foam
NTP	Non-thermal plasma
OD	Outer diameter
SA	Sliding angle
SAM	Self-assembled monolayer
SCCM	Standard Cubic Centimeters per Minute
SEM	Scanning electron microscopy

TMS	Tetramethylsilane
TMDSO	Tetramethyldisiloxane
TEOS	Tetraethyl orthosilicate
V _p	Pore volume
WCA	Water contact angle
XPS	X-ray photo electron spectroscopy
XRD	X-ray diffraction

List of Tables

Table 2.1.1. List of chemicals used in this thesis.	25
Table 2.1.2. List of apparatus used in this thesis.	26
Table 3.1.1. Operating conditions and WCA measurement results.	42
Table 3.1.2. Thickness and RMS roughness of each sample.	45
Table 3.1.3. Deconvolution of C1s spectra along with binding energies and functional groups.	51
Table 3.1.4. Scratch test results for each sample.	54
Table 4.1.1. Thickness and RMS roughness of each sample.	72
Table 4.1.2. Deconvolution of C1s spectra along with binding energies and functional groups.	82
Table 4.1.3. Scratch test results (breakdown force).	83
Table 5.1.1. Thickness and RMS roughness of each sample.	101
Table 5.1.2. Thickness and RMS roughness of each sample.	107
Table 5.1.3. Scratch test results for each sample.	110

List of Figures

Figure 1.1.1. Typical corona discharge photographic image.....	3
Figure 1.1.2. Historic ozone discharge tube of W. Siemens, 1857, adapted from [11].....	4
Figure 1.1.3. Typical DBD reactor configurations.	5
Figure 1.1.4. WCA results of (a) hydrophilic surface, (b) hydrophobic surface and super (c) hydrophobic surface.....	9
Figure 1.1.5. Liquid droplet on solid rough surface: (a) Young’s mode; (b) Wenzel’s mode; (c) Cassie’s mode.	12
Figure 1.1.6. Ragone plot for various energy storage and conversion devices, adapted from [43].	15
Figure 1.1.7. Taxonomy of supercapacitors.	16
Figure 1.1.8. Schematic of an electrochemical double-layer capacitor.	18
Figure 2.1.1. Principle of X-ray photoelectron spectroscopy.	29
Figure 2.1.2. Simplified block diagram of the FT-Raman spectrometer.	30
Figure 2.1.3. Schematic diagram of FTIR.	31
Figure 2.1.4. (a) Mass flow controller and (b) Pressure & Flow controller.	32
Figure 2.1.5. NV-2400 3D nano-profiler system.....	33
Figure 3.1.1. Schematic diagrams of (a) the experimental setup and (b) home-made scratch tester.....	37
Figure 3.1.2. Dependence of WCA on (a) the treatment time, (b) the applied voltage, (c) the H/A ratio and (d) the gas flow rate.	41

Figure 3.1.3. (a) Aging time effect and (b) annealing temperature.	44
Figure 3.1.4. AFM images of the coated samples. (a) H100; (b) H/A = 3/1; (c) H/A = 1/1; (d) H/A = 1/3; and (e) A100.	46
Figure 3.1.5. SEM images of the coated samples. (a) H100; (b) H/A = 3/1; (c) H/A = 1/1; (d) H/A = 1/3; and (e) A100.	47
Figure 3.1.6. Surface modification and possible reaction routes of APTES: (a) hydrogen bonding due to initial adsorption, (b) surface attachment, and (c) multilayer formation.	48
Figure 3.1.7. FTIR spectra of the coated samples from 500 to 3500 cm^{-1}	49
Figure 3.1.8. Atomic composition (%) of selected sample surfaces.	51
Figure 3.1.9. Deconvolution of C1s spectra (282–290 eV) of the selected coated samples.	52
Figure 3.1.10. UV-visible spectra of the coated samples.	53
Figure 3.1.11. Breakdown forces of the samples obtained by the scratch tests.	55
Figure 3.1.12. Microscope images of the selected samples.	56
Figure 4.1.1. The schematic figure of the experimental setup (a) and custom-built scratch tester (b).	64
Figure 4.1.2. Discharge photograph image of the plasma jet.	65
Figure 4.1.3. Dependence of WCA on (a) treatment time, (b) applied voltage, (c) the TMS/APTES ratio and (d) the flow rate of the carrier gas.	68
Figure 4.1.4. Photograph image of the coated surface in the coated state.	70
Figure 4.1.5. (a) Effect of aging time and (b) annealing temperature on the coating.	71

Figure 4.1.6. AFM images of the coated samples. [TM = TMS and AP = APTES, (a) APTES only, (b) TM/AP = 3, (c) TM/AP = 3.4, (d) TM/AP = 3.7, (e) TM/AP = 4.8, (f) TM/AP = 6, and (g) TMS only].	73
Figure 4.1.7. SEM images of the coated samples. [TM = TMS and AP = APTES, (a) APTES only, (b) TM/AP = 3, (c) TM/AP = 3.4, (d) TM/AP = 3.7, (e) TM/AP = 4.8, (f) TM/AP = 6, and (g) TMS only].	74
Figure 4.1.8. (a) Gas-phase FTIR spectra of the Ar/TMS without (black) and with (red) plasma and (b) gas-phase FTIR spectra of the Ar/APTES without (black) and with (red) plasma from 1000 to 3500 cm^{-1} .	76
Figure 4.1.9. Possible reaction routes and mechanism of APTES for the surface modification: (a) hydrogen bonding due to initial adsorption, (b) surface attachment, and (c) multilayer formation.	78
Figure 4.1.10. FTIR spectra of coated samples from 500 to 4000 cm^{-1} .	79
Figure 4.1.11. Elemental composition (%) of sample surfaces.	80
Figure 4.1.12. Deconvolution of C1s spectra (282–290 eV) of the coated samples.	81
Figure 4.1.13. UV–vis transmission of the coated samples.	82
Figure 4.1.14. Scratch test results sustained by the samples.	84
Figure 4.1.15. Scratch test photographs taken by the microscope.	85
Figure 5.1.1. Schematic diagram of the plasma jet reactor system.	95
Figure 5.1.2. Schematic diagram of the home-made scratch tester.	96

Figure 5.1.3. Dependence of WCA on (a) the treatment time, (b) the applied voltage, (c) the A/T ratio and (d) the total flow rate of the carrier gases.	99
Figure 5.1.4. 3D nano-profiler images of the selected samples. (a) A100; (b) T100; and (c) A/T=1.7.....	102
Figure 5.1.5. FE-SEM images of the selected samples. (a) A100; (b) T100; and (c) A/T=1.7..	103
Figure 5.1.6. Effect of (a) aging time and (b) annealing temperature on the WCA.	104
Figure 5.1.7. FTIR spectra of the samples prepared at different A/T ratios.	105
Figure 5.1.8. Surface elemental composition of the selected samples.	107
Figure 5.1.9. Deconvolution of C1s spectra of the selected coated samples.	108
Figure 5.1.10. (a) UV-visible spectra of the samples prepared at different A/T ratios, and (b) top and side view of the selected sample (A/T=1.7).....	109
Figure 5.1.11. Breakdown forces of the samples obtained by the scratch tests.....	111
Figure 5.1.12. Microscope images of the selected samples.....	112
Figure 6.1.1. Conventional planar DBD configuration.	123
Figure 6.1.2. Photographic images of (a) bare nickel foam (b) after coating and thermal pyrolysis (carbon/nickel foam) and (c) microscopic image of carbon/nickel foam at 100X magnification from Raman spectroscopy.....	124
Figure 6.1.3. FE-SEM image of (a) bare nickel foam, (b) 120 min coated nickel foam, and (c) thickness of the coated thin film.	126
Figure 6.1.4. Raman spectra result of coated sample. [Treatment time 120 min, n-heptane concentration 2000 ppm and Ar gas flow rate 1.6 L/min].....	127

ABSTRACT

This thesis focused on improving the robustness of the thin film for hydrophobic surface and deposition of carbon thin layer for the electrode of energy storage devices by using non-thermal plasma (NTP). NTP can effectively produce a protective or hydrophobic coating layer on the surfaces of various materials, namely glasses, porous surface, fabrics, powders, and polymers with low cost. Thermal coating presents low efficiency with a non-uniform coating layer, and the sol-gel method shows poor visibility along with a non-uniform coating layer. However, the gas phase coating by NTP is an alternative method, that presents a uniform coating layer with excellent visibility. In this study, it is shown that NTP is useful to generate uniform robust thin film on the various surfaces using gas phase precursors at ambient condition.

Hydrophobic surfaces have various applications such as self-cleaning windshields, for anti-contamination, anti-sticking of snow for windows and antennas, anti-biofouling paints for boats, anti-icing, anti-corrosion, etc. The surface wettability is determined by the measurement of the water contact angle (WCA). A surface is said to be wetted if a liquid spread over the surface evenly without forming the droplets. If the water spreads over the surface and it does not form droplets, then the surface is called hydrophilic. Regarding surface static water contact angle, a surface having water contact angle (WCA) $< 90^\circ$ is known as hydrophilic surface but that having WCA $\geq 90^\circ$ is known as hydrophobic. In addition, surface having WCA $> 150^\circ$ and sliding angle (SA) $\leq 10^\circ$ is called super-hydrophobic owing to its outstanding self-cleaning capability. Both, the WCA and the SA show the performance of the thin film surface that how effective it is in the self-cleaning function. The wettability of a solid surface is a property that depends on both surface roughness and surface chemistry and directly related to the surface free energy. Basically, materials with low

surface energies are used to prepare hydrophobic surfaces and materials rich in hydrocarbon are suggested to make anode materials.

Many research groups have tried to make durable superhydrophobic surfaces over metals, organic or inorganic substrates. Long-lasting hydrophobic coatings are not readily achievable with only low surface energy materials, mainly because of their poor adhesion nature to solid surfaces. Low surface energy materials such as hexamethyldisiloxane (HMDSO, $O[Si(CH_3)_3]_2$), pentamethyldisiloxane (PMDSO, $C_5H_{16}OSi_2$), tetramethyldisiloxane (TMDSO, $[(CH_3)_2SiH]_2O$), tetramethylsilane (TMS, $Si(CH_3)_4$), trimethylsilane (TriMS, $HSi(CH_3)_3$) and tetraethyl orthosilicate (TEOS, $Si(OC_2H_5)_4$) are well-known organosilicon precursors capable of forming hydrophobic layers. On the other hand, methane (CH_4), ethylene (C_2H_4), propane (C_3H_6), butane (C_4H_8), pentane (C_5H_{10}), hexane (C_6H_{12}), and heptane (C_7H_{14}) are rich in hydrocarbon. So, these hydrocarbons are good candidates to form a carbon polymer layer on the surfaces. Conventional chemical polymerizations have a drawback of poor adhesion on solid surfaces, and as well, the coating layers created do not function well after several scratches due to their chemical nature. For industrial applications, wear resistance, and adhesive properties are critical factors. The poor adhesive property may be improved by incorporating aminopropylethoxysilanes that are silanating mediators for modifying the silica-based materials' surface. The aminosilanes anchor to the surface and establishing a Si-O-Si covalent bond and hydrogen bonding with the amino group. Among aminosilanes, (3-aminopropyl)triethoxysilane (APTES, $H_2N(CH_2)_3Si(OC_2H_5)_3$) and 3-aminopropyl(diethoxy)methylsilane (APDMES, $CH_3Si(OC_2H_5)_2(CH_2)_3NH_2$) have widely been used along with low surface energy materials. After studying all those chemicals, TMS, HMDSO, APTES, and APDMES were chosen to use as precursors for the robust hydrophobic surfaces and n-heptane and ethylene was used for the anode materials. The plasma reactor was operated with a

high-voltage alternating current (AC) power source whose frequency output was set to 11.5 kHz. In all the cases, noble gas argon (Ar) and the same power source were used to generate plasma. Dielectric barrier discharge (DBD) configuration was used in both hydrophobic coatings and preparing of graphitic carbon materials for the anode cases. The cylindrical plasma jet was used for hydrophobic coatings, but in the case of preparing anode materials, the plasma configuration was changed to planar DBD plasma.

This thesis divided into seven chapters dealing with plasma polymerization of different precursors. Glass substrates have been used to deposit polymer layer for hydrophobic coatings and nickel foams to deposit hydrocarbon to prepare anode materials for the energy storage devices. In chapter one and two, literature review to support this thesis has been discussed widely. In chapter three, robust hydrophobic coating with excellent visibility has been investigated using HMDSO and APTES precursors. In this study, the H/A (HMDSO/APTES) ratio between two precursors has been varied from 3/1 to 1/3 to check the WCA and robustness of the coatings. The highest WCA was measured to be 143° at the ratio of 3/1. The detailed discussion has been done in chapter two.

In chapter four, TMS was used along with APTES and the plasma configuration was changed from dielectric barrier discharge (DBD) to corona discharge so that the surface having any kind of thickness can be treated. But corona discharge has shown noticeable drawback over DBD plasma in terms of treated surface area and treatment time. The treated surface area by the corona discharge is smaller and the treatment time increased from 5 to 6 times with compare to DBD. The T/A (TMS/APTES) ratio has been varied from 3.0 to 7.0 and the obtained WCA angle and coating robustness were almost similar to the DBD case.

Superhydrophobic surface has been investigated in chapter five. DBD configuration has been used in order to treat large surface area within short treatment time. Two precursors namely TMS and APDMES were used in the plasma polymerization process and deposited onto the glass substrate. Despite the hydrophilic nature of APDMES, however, the coatings prepared with the mixture of these two precursors exhibited increases in the WCA from 154 to 163° as the A/T (APDMES/TMS) ratio was increased from 1 to 1.7. But, further increase in the A/T ratio to 2.4 led to a decrease in the WCA, suggesting that the coating layer begins to change toward hydrophilic at around this A/T ratio.

Preparing of carbon material has been studied in chapter six using planar DBD configuration reactor. For this study, n-heptane was used as precursor to deposit hydrocarbon on the nickel foam. The plasma treatment time was varied from 5 to 120 min to find the optimal coating thickness and then pyrolysis was performed under nitrogen environment at 800 °C for 6 hours to convert hydrocarbon to carbon on the nickel foam. The formation of the carbon is confirmed by the Raman spectra. The detailed discussion has been done in chapter six.

The coating films formed under different conditions were characterized by atomic force microscopy (AFM), scanning electron microscopy (SEM), X-ray powder diffraction (XRD), X-ray photoelectron spectroscopy (XPS), cyclic voltammetry (CV), Raman spectroscopy, Fourier transform infrared spectroscopy (FTIR), static water contact angle (WCA), and scratch test.

CHAPTER-1

Literature review

1.1. Introduction and literature review

Plasma polymerization has been gaining the popularity to the researchers as an excellent surface modification technique. There are numerous advantages in this method. Plasma polymerization is a dry and solventless process which is eco-friendly and easy to handle. Furthermore, it is a beneficial technique where a large variety of chemically active species (ions or radicals) create to attach specific functional groups on the surface which can provide a thin layer on the surface that does not damage or change the bulk properties of the substrate. This technique can be used to improve hydrophobicity, biocompatibility, printability, adhesion, and corrosion protection of materials. This technique can also be used to prepare carbon materials that can be used to make the anode for the energy storage devices. The wide discussion to understand about the plasma, hydrophobicity, and energy storage devices has been discussed in the below one by one.

1.1.1. Plasma

Plasma can be described as an ionized gas having approximately equal numbers of negatively charged electrons and positively charged ions. It is also called one of four fundamental states of matter. The negative charge is carried by the electrons while the positive charge is carried by atoms or molecules that are missing those same electrons. It can be generated in the laboratory by heating a gas to an extremely high temperature, which causes such vigorous collisions between

its atoms and molecules that electrons are ripped free, yielding the requisite electrons and ions. Plasma is seen almost every visible matter in the universe such as in the sun and stars. Welding arcs, lighting, and auroras are also kind of plasma that we can see often. Plasma even exists in fluorescent and neon tube and also many other objects. If we think about our beautiful earth that itself immersed in the tenuous plasma called the solar wind and is surrounded by plasma called the ionosphere. In the 1920s, chemist Irving Langmuir first described the plasma. The characteristics of plasmas are significantly different from those of ordinary neutral gases.

1.1.2. Non-thermal plasma

There are many types of plasma can be found but, in this thesis, only NTP will be discussed. NTP is defined by its non-equilibrium state with electron temperature much higher than those of ions and neutral species [1]. For this type of plasma, the gas temperature is virtually equal to the atmospheric temperature, and the electron temperature is of the order of 1-10 eV or several tens of thousands of K [2]. This type of plasma can be generated at atmospheric pressure and room temperature by either corona discharge (CD) or dielectric barrier discharge (DBD).

Corona discharge is kind of self-sustaining discharge happens in the non-uniform electric fields in gas-phase media [3]. CD can be used in surface treatment, electrostatic precipitation, air purification, water treatment, and many other fields [4–8]. Meanwhile, CD has significant negative effect such as corona loss, electromagnetic interference in high-voltage transmission lines, audible noise, and insulation aging damage in large electrical machines [9,10]. So, it should be overcome all those problems. Current researches on corona discharge covered many fields including electrode interface contact potential barrier, charge injection, air molecules ionization, particle movement, parasitic field distribution, etc. However, due to the numerous influencing factors and difficulty of direct observation, the physical nature behind the corona discharge is still unclear and

requires further research. Figure 1.1.1 shows the photographic image of a CD taken by iPhone 6 in the atmospheric environment using argon as a discharge gas at a flow rate of 1.5 L/min.



Figure 1.1.1. Typical corona discharge photographic image.

Dielectric barrier discharge (DBD) is considered as a nonthermal plasma that has received great attention due to its special characteristics. It has been extensively used for various applications such as ozone synthesis, surface modification, and biological and chemical decontamination [11,12]. Scientists have been known about DBD more than a century. In the year 1857, Siemens first introduced experimental investigations about DBD plasma [11,13]. They focused to generate ozone using the flow of oxygen or air to the influence of a DBD maintained in a narrow annular gap between two coaxial glass tubes by an alternating electric field of sufficient amplitude. Figure 1.1.2 shows the novel feature of this discharge apparatus which is that the electrodes are positioned outside the discharge chamber and are not in contact with the plasma.

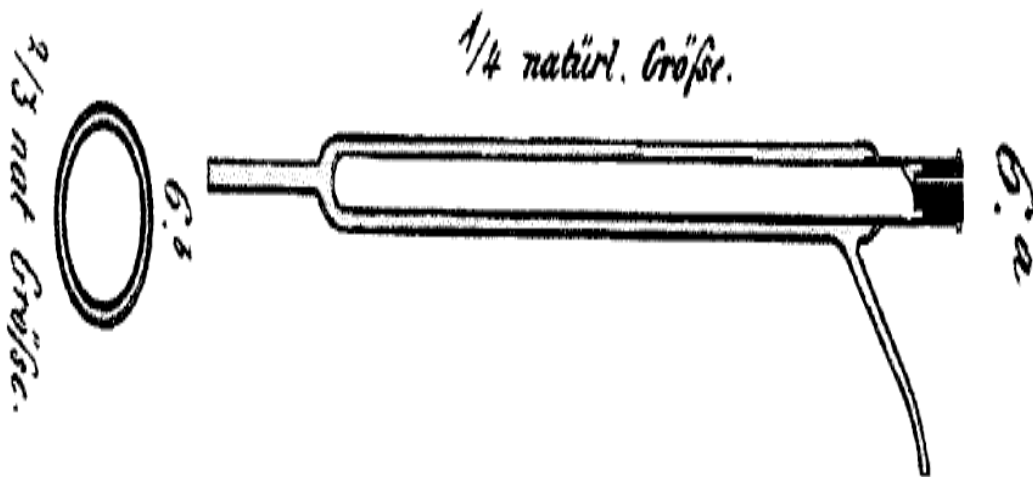


Figure 1.1.2. Historic ozone discharge tube of W. Siemens, 1857, adapted from [11].

Generally, a DBD at atmospheric pressure operates in two different modes, i.e., homogenous and filamentary [14]. In the filamentary mode, a large number of micro-discharges are randomly formed between two electrodes, whereas in the homogeneous discharge, a uniform plasma covers the electrode surface. In spite of the industrial application of filamentary mode, homogenous discharge is most demanded for many applications, particularly for biological and medical applications. DBD has more advantages over CD especially for uniform surface modification. Hence DBD configuration was selected for my study. Basic electrode arrangement of DBD configurations are shown in Figure 1.1.3. They are distinguished by the presence of at least one insulating layer typically glass or ceramic materials between two planar or cylindrical electrodes connected to an AC power supply [15].

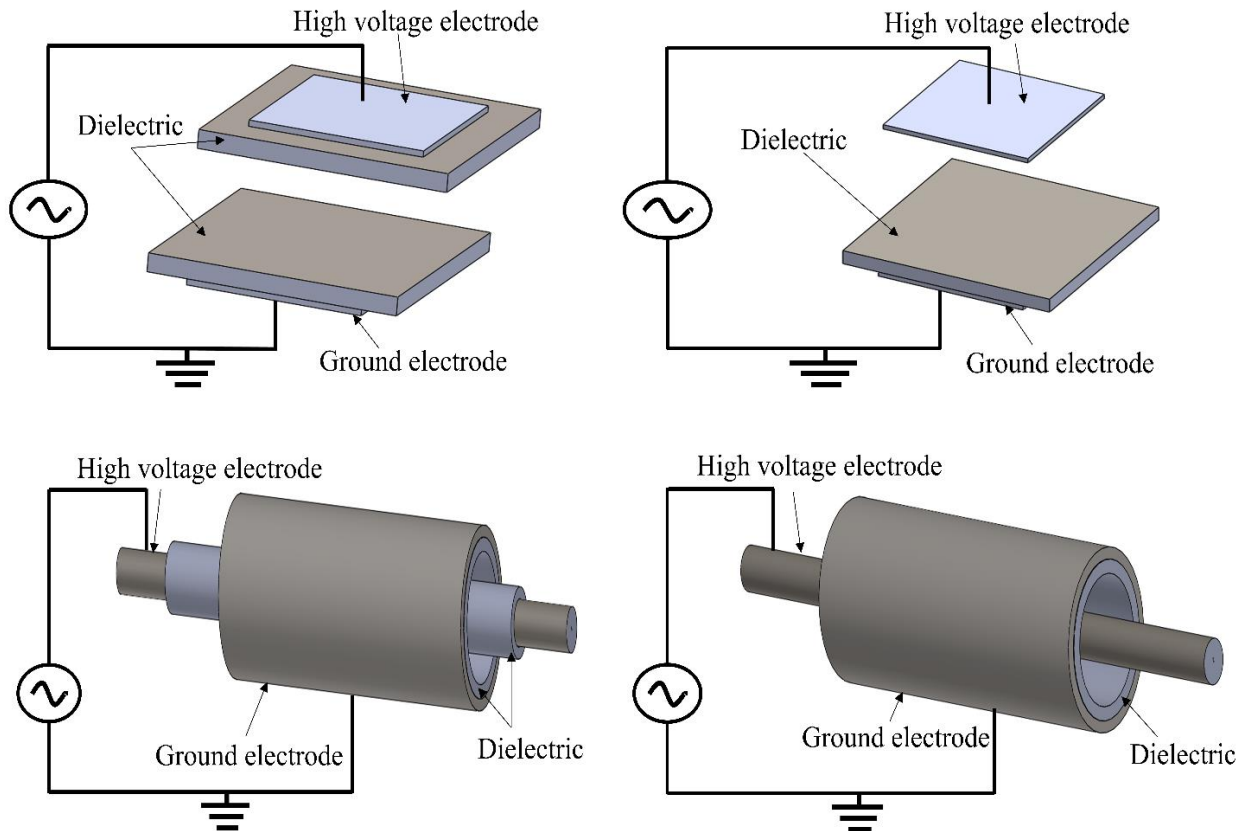


Figure 1.1.3. Typical DBD reactor configurations.

Breakdown in the gas between two electrodes is locally initiated by applying an electric field larger than the breakdown field. The growing electron avalanches quickly produce such a space charge that self-propagating filament streamers are formed. The DBD plasma at atmospheric pressure is characterized by a large number of short-lived micro-discharges. These micro-discharges are almost cylindrical plasma channels and spread into large surface discharges at dielectric surface. The dielectric serves as dual purpose to limit the amount of charge and energy imparted to an individual micro-discharge, and at the same time distributes the micro-discharge over the entire electrode area. The formation of micro-discharges is featured by electron multiplication; excitation, dissociation, and ionization processes and space charge accumulation [11].

The charge transferred in the micro-discharged or accumulated on the dielectric plays an important role in the characteristics of the DBD, since it not only affects the electric field in the gas gap, but also enhances the atomic processes in the discharge [16]. During the rising part of external voltage, additional micro-discharges are initiated at new locations because the presence of residual charges on the dielectric has reduced the electric field at position where micro-discharge have already occurred. On voltage reversal, however, the next micro-discharges will form at old micro-discharge locations. Since the voltage has collapsed at these locations, it takes less external voltage swing to reach breakdown in the following half period of opposite sign. Consequently, high-voltage low-frequency operation tends to reignite the old micro-discharge channels every half period. This memory effect due to charge accumulation on the dielectrics is a dominant feature in all barrier discharges [17].

1.1.3. Chemical activity of nonthermal plasma

High chemical efficiency is the main advantage of NTP with nearly all input energy converted to energetic electrons without significant heating of the bulk gas. The hot electrons can trigger many different chemical processes such as excitation, ionization and dissociation, leading to formation of various active species that can further react with more stable ones. Examples of these species are OH, O, and N radicals; excited N₂ molecules; and atomic and molecular ions (e.g., O⁺, O₂⁺) [18].

The elementary processes NTP can be broadly divided into a primary process and a secondary process on the time-scale of streamer propagation. Ionization; electronic, vibrational, and rotational excitation; fragmentation; light emission; and charge transfer are those processes included in the primary process within a timescale of about 10⁻⁸ s. The secondary process is the subsequent chemical reaction involving the products of primary processes. Some additional radical species and reactive molecules (O₃, HO₂, and H₂O₂) are also formed by radical-neutral recombination in the secondary process [19].

In treating gaseous pollutants in ppm (parts per million by volume) range, it is hard to expect that a direct decomposition of dilute pollutant through collisions with energetic electrons in the primary process play an important role. The majority of the electron energy is transferred to the dominant gas molecules of nitrogen and oxygen through many inelastic collisions and then leads to the formation of radicals. The decomposition of gaseous pollutants starts to occur only after the formation of radicals is initiated [20].

1.2. Hydrophobicity, hydrophilicity, and silanes

1.2.1. Hydrophobicity and hydrophilicity

Surface is a very important branch of science that touches all facets of our lives. The most recognizable definitions in surface science are hydrophobicity and hydrophilicity. In the Greek words, hydro means water, philicity means affinity, and phobicity means lack of affinity. A surface is said to be wetted if a liquid spread over the surface evenly without the formation of droplets. When the liquid is water and it spreads over the surface without the formation of droplets, the surface is said to be hydrophilic. A surface is hydrophilic if it tends to absorb water or be wetted by water. In terms of surface static water contact angle, a surface having water contact angle (WCA) $< 90^\circ$ is known as hydrophilic surface but having $WCA \geq 90^\circ$ is known as hydrophobic surface. On the other hand, surface having $WCA > 150^\circ$ and sliding angle (SA) $\leq 10^\circ$ is called super-hydrophobic surface due to its excellent self-cleaning ability. Generally, WCA and SA indicate the performance of the surface how much it will be effective in self-cleaning function. Figure 1.1.4 shows WCA results of (a) hydrophilic surface, (b) hydrophobic surface and (c) superhydrophobic surface. Our goal is to use NTP to generate hydrophobic coating layer on the surface. Hence, we have more discussion about hydrophobicity than hydrophilicity. Researchers found the idea to make hydrophobic surface from nature [21–23] to use it for various purposes as self-cleaning windows, anti-icing, out-door textiles, self-cleaning of antennas, ultra-dry surface applications, protection of circuits and grids, medical devices, and other optical apparatuses [24–28]. Basically, the thin films deposited by plasma polymerization are pinhole free, have good adhesion, and have better mechanical and chemical stabilities. To get hydrophobic characteristics the surface requires nano- to micro-scale roughness. Both the surface roughness and the surface chemistry affect the hydrophobicity [29]. Up to now, several methods have been proposed to

generate surface roughness, including plasma treatment, sol-gel deposition, anodization, electrodeposition, chemical treatment, hot-water immersion, and lithography. Low surface energy materials such as hexamethyldisiloxane (HMDSO, $O[Si(CH_3)_3]_2$), pentamethyldisiloxane (PMDSO, $C_5H_{16}OSi_2$), tetramethyldisiloxane (TMDSO, $[(CH_3)_2SiH]_2O$), tetramethylsilane (TMS, $Si(CH_3)_4$), trimethylsilane (TriMS, $HSi(CH_3)_3$), tetraethyl orthosilicate (TEOS, $Si(OC_2H_5)_4$), and fluorocarbons are well-known organosilicon precursors capable of forming hydrophobic layers [30–32]. The plasma polymerization of silicon-based compounds is more environmentally friendly.

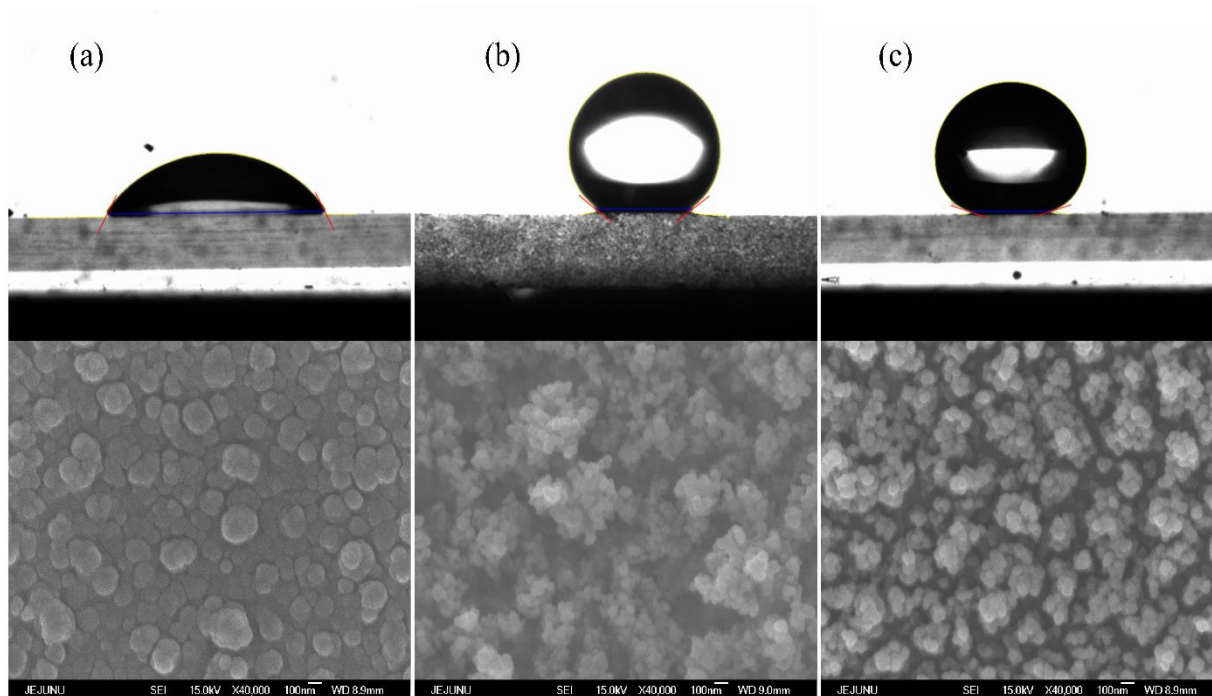


Figure 1.1.4. WCA results of (a) hydrophilic surface, (b) hydrophobic surface and super (c) hydrophobic surface.

1.2.2. Theoretical background of hydrophobicity and hydrophilicity

1.2.2.1. Young's equation

If a drop of liquid is put on the solid surface, it forms a contact angle (θ). Measuring the contact angle of liquid by using Young's equation is only applicable for flat surface and not to a rough one. The contact angle of a liquid on a perfectly smooth and chemically homogeneous solid surface is given by Young's equation [33]:

$$\cos\theta = \frac{(\gamma_{sv} - \gamma_{sl})}{\gamma_{lv}} \quad (1.1.1)$$

where, γ_{sv} , γ_{sl} , and γ_{lv} are the interfacial tensions of the solid-vapor, solid-liquid and the liquid-vapor interface, respectively. Figure 1.1.5(a) shows the wetting behavior of a liquid droplet on flat solid surface ((a) Young's mode). Wetting of realistic surfaces which are rough and chemically heterogeneous is more complex. The earliest work on the effect of surface roughness on contact angle was done by Wenzel and Cassie & Baxter.

1.2.2.2. Wenzel's equation

An equation has been developed by Wenzel [34] where the liquid may completely penetrate into the rough grooves (Figure 1.1.5(b)), and the contact angle on rough surfaces is given by the following equation:

$$\cos\theta_w = \frac{r(\gamma_{sv} - \gamma_{sl})}{\gamma_{lv}} = r \cos\theta \quad (1.1.2)$$

where, θ is the Young's contact angle on a similar smooth surface, θ_w is the contact angle on a rough surface, and r is the surface roughness factor, defined as the ratio between the actual and projected surface area ($r = 1$ for a perfectly smooth surface, and $r > 1$ for a rough one). Using the Wenzel equation, it can predict that wetting is enhanced by roughness, when θ is $< 90^\circ$; and the

wetting is lessened by roughness, when θ is $> 90^\circ$. However, when $\theta > 90^\circ$, under some roughness condition, air bubbles may be trapped in the rough grooves. In this case, the liquid droplet is actually situated on a composite surface, and the wetting behavior is described by Cassie & Baxter.

1.2.2.3. Cassie-Baxter's equation

The Cassie-Baxter is a wetting state where, the grooves under the droplet are filled with vapor instead of fluid/liquid, as schematically shown in Figure 1.1.5(c). This regime was first described by Cassie and Baxter in 1944 [35]. In this case, the liquid-surface interface is actually an interface consisting of two phases, namely a liquid-solid interface and a liquid-vapor interface. And the apparent contact angle is the sum of all the contributions of the different phases as described below:

$$\cos\theta_c = f_1 \cos\theta_1 + f_2 \cos\theta_2 \quad (1.1.3)$$

here, θ_1 and θ_2 are the contact angles on phase 1 and phase 2, respectively. θ_c is the apparent contact angle and f_1 and f_2 are the surface fractions of phase 1 and phase 2, respectively. This is the general form of equation, which also can apply when there is no roughness. If one of these surfaces is the air-liquid interface, f is the solid fraction, defined as the fraction of the solid surface that is wetted by the liquid. Then the air fraction is $(1 - f)$. With $\theta = 180^\circ$ for air, the resulting contact angle can be calculated by the following equation:

$$\cos\theta_c = f \cos\theta + (1 - f)\cos 180^\circ = f \cos\theta + f - 1 \quad (1.1.4)$$

The parameter f ranges from 0 to 1, where at $f = 0$ the liquid droplet does not touch the surface at all and at $f = 1$ the surface is completely wetted, the same as the behavior of a flat surface. When

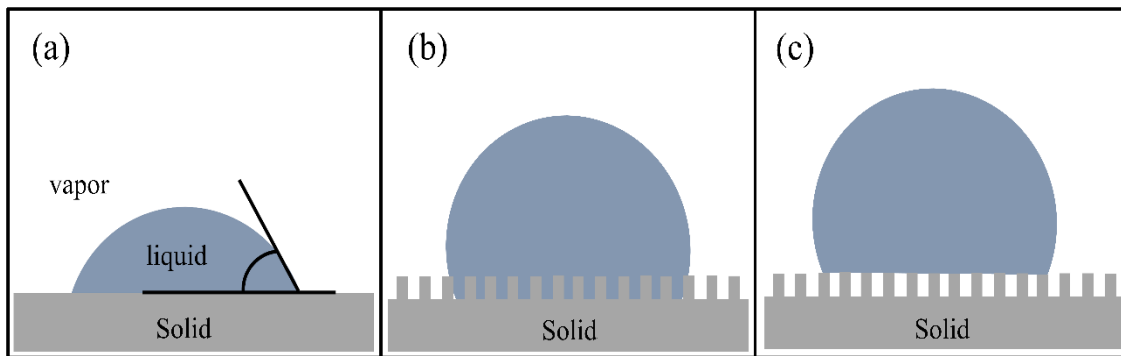


Figure 1.1.5. Liquid droplet on solid rough surface: (a) Young's mode; (b) Wenzel's mode; (c) Cassie's mode.

a droplet is in the Cassie- Baxter state, the small contact area between the liquid droplet and solid surface allows the droplet to roll easily over the surface.

1.2.3. Silanes

Silanes are silicon chemicals that possess a hydrolytically sensitive center that can react with inorganic substrates such as glass to form stable covalent bonds and organic substitution that alters the physical interactions of treated substrates. Unlike than most additives, which have a limited performance range, they can achieve surface properties ranging from hydrophilic to hydrophobic. They may be a sole active ingredient or a component in a coatings formulation, controlling the interaction of water over a broad spectrum of requirements. In order to understand how silanes can affect hydrophobicity and hydrophilicity, it is important to understand some of the fundamentals of the interaction of water with surfaces.

The aminosilanes anchor to the surface, forming Si-O-Si covalent bond and hydrogen bonding with the amino group. Among aminosilanes, (3-aminopropyl)triethoxysilane (APTES,

$\text{H}_2\text{N}(\text{CH}_2)_3\text{Si}(\text{OC}_2\text{H}_5)_3$ and 3-aminopropyl(diethoxy)methylsilane (APDMES, $\text{CH}_3\text{Si}(\text{OC}_2\text{H}_5)_2(\text{CH}_2)_3\text{NH}_2$) have widely been used along with low surface energy materials.

1.3. Energy storage devices

Energy storage devices are such devices used to store electric energy when needed and releasing it when required. These devices have been playing a major role within energy harvesting technology and wireless sensor networks to monitor the equipment due to its ability to store and slowly release harvested energy at ultra-low power over extended time periods.

Overall there are two types of energy storage devices. Firstly, there are electrical storage devices such as batteries, capacitors, and superconducting magnetic energy storage. Secondly, there are non-electrical energy devices which convert thermal and kinetic energy into electrical energy using flywheels, pumped hydro, and pumped air storage systems. In this study, anode materials are being prepared to use in supercapacitor study and hence supercapacitor has been discussed briefly.

1.3.1. Supercapacitor

A supercapacitor (SC) also known as electrochemical capacitor is a very high-capacity capacitor with plentiful higher capacitance values than other ordinary capacitors consist of two electrodes composed of a high surface area material, placed either side of the thin charge layer that contain the electrolyte. This supercapacitor is able to achieve very high specific capacitance and can maintain the much faster rate of charge and discharge with compare to typical capacitors [36]. A supercapacitor consists of two electrodes, an electrolyte, and a separator which isolates the two electrodes electrically. Basically, the most important component of a supercapacitor is its electrode

materials [37,38]. The benefits of the supercapacitors over other energy storage devices are long life, high power, wide thermal range (-40 °C to 70 °C), flexible packaging, low weight, and low maintenance [39]. The best utilization of supercapacitor can be in the areas that required applications with short load cycle and high reliability such as electric vehicles, load cranes, and power quality improvement [40]. Among the promising applications of supercapacitors is in fuel cell vehicles and low emission hybrid vehicles[41]. The unique qualities of the supercapacitors are when used with batteries or fuel cells they serve as temporary energy storage devices providing high power capability to store energy from braking [42].

The improvement of performance of a supercapacitor is shown in Figure 1.1.6, which is known is a “Ragone plot.” This graph (Figure 1.1.6) presents the power densities of various energy storage devices such as fuel cells, batteries, supercapacitors, typical capacitors, etc, measured along the vertical axis, versus their energy densities, measured along the horizontal axis. According to the graph, the supercapacitors occupy a region between batteries and conventional capacitors [43].

A bank of supercapacitors (several capacitors of the same rating that are connected in series or parallel with each other to store electrical energy) can be used as bridge the short time duration between a power failure and the startup of backing power generations due to its high-power capability. However, the energy density of supercapacitor is greater than that of typical capacitors but it is still considerably lower than batteries or fuel cells. Electrochemical performances of an electrode material strongly rely on factors like surface area, electrical conductivity, wetting of electrode and permeability of electrolyte solutions [44].

A lot of challenges are faced by supercapacitors including low energy density, low voltage per cell, high self-discharge, and production cost. Developing the new electrode materials can be

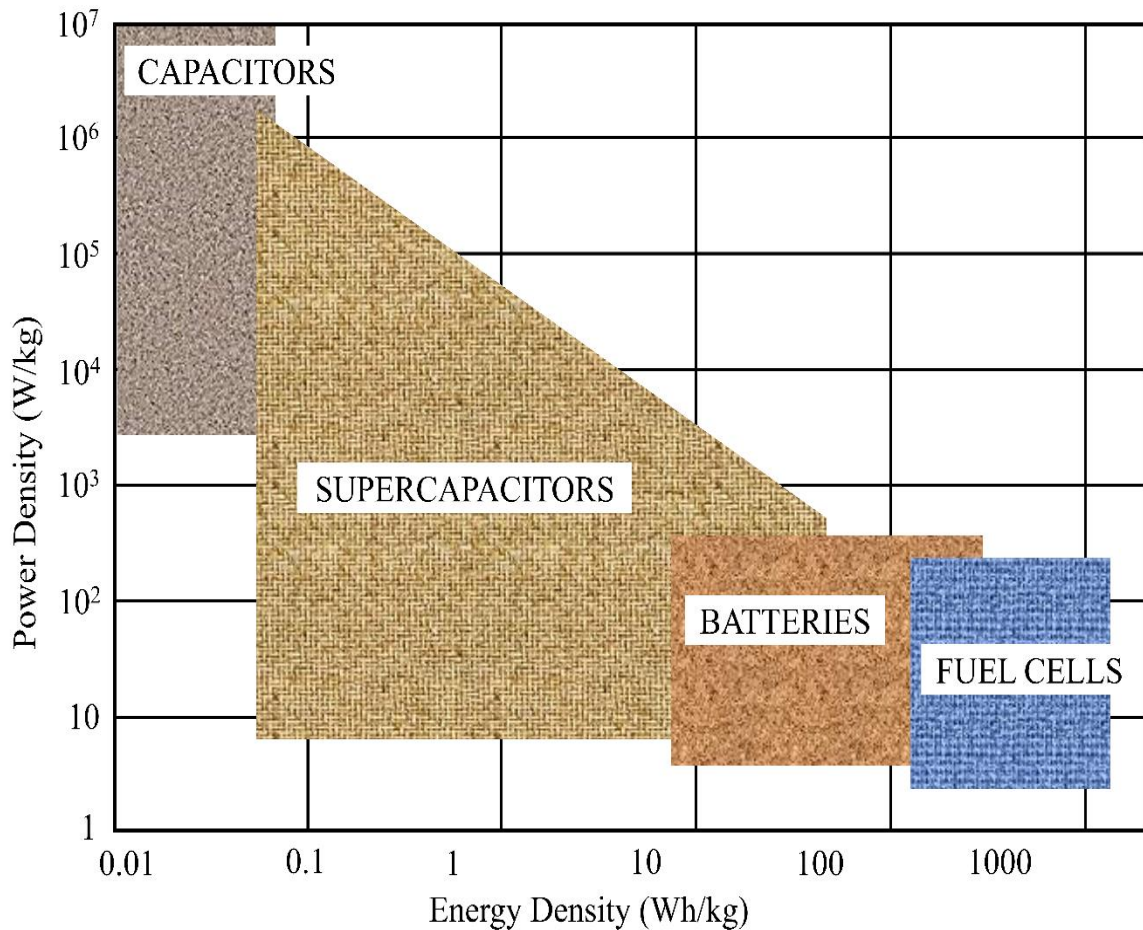


Figure 1.1.6. Ragone plot for various energy storage and conversion devices, adapted from [43].

a strong candidate to overcome the obstacle of low energy density problem. Nowadays, carbon materials, metal oxides and conducting polymers are the most popular materials for using as electrode materials to the researchers. Fabrication of carbon materials have been used from the beginning of the supercapacitor due to their high surface area properties. On the other hand, metal oxides offer excellent choice as electrode material due to its high specific capacitance and low resistance, making it easier to construct high energy and power supercapacitors. In the case of conducting polymers reduction-oxidation process is used to store and release charge [45].

1.3.2. Energy storage mechanism and classification of supercapacitor

The operation principle of supercapacitor is based on energy storage and distribution of the ions coming from the electrolyte to surface area of the electrodes. The mechanism of energy storage of supercapacitors can be divided into three classes: (a) Electrochemical double-layer capacitors, (b) pseudocapacitors, and (c) hybrid supercapacitors as shown in Figure 1.1.7 below.

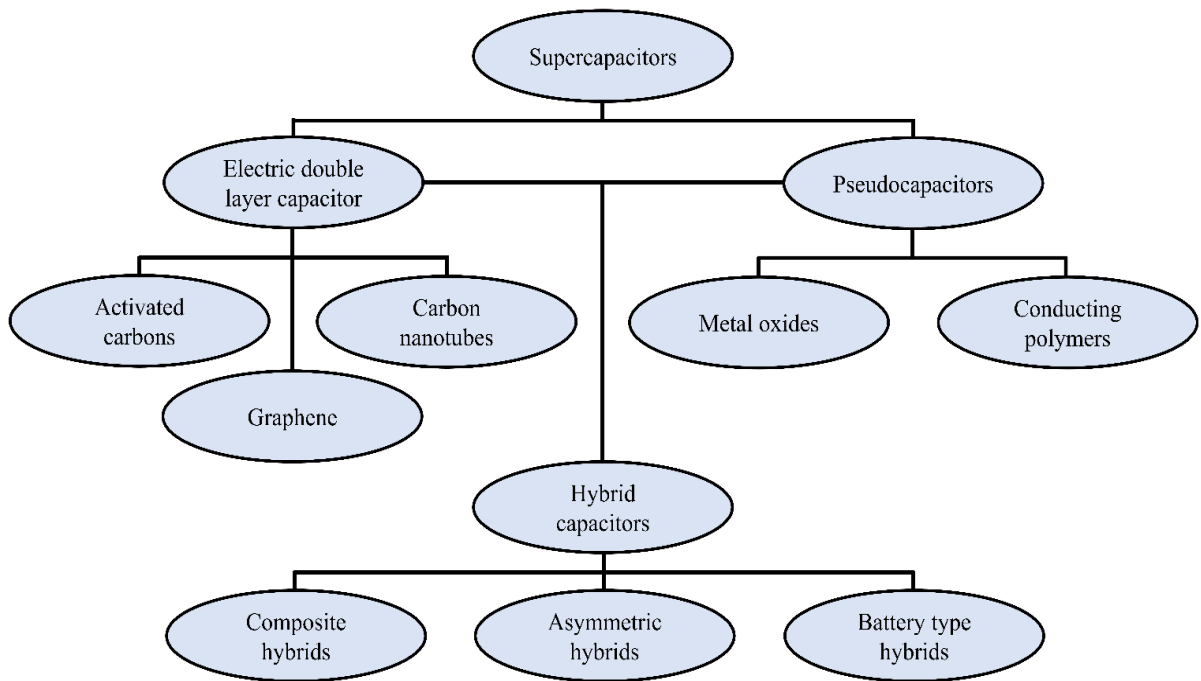


Figure 1.1.7. Taxonomy of supercapacitors.

1.3.2.1. Electrochemical double layer capacitors (EDLCs) mechanism

Figure 1.1.8 shows the schematic of an electrochemical double-layer capacitor. The general construction process of electrochemical double-layer capacitors (EDLCs) are based on two carbon-based electrodes/materials, an electrolyte, and a separator. EDLCs can store charge either electrostatically or non-Faradaically but also make sure that the charge should not be allowed to transfer between electrode and electrolyte. To store energy, EDLCs use an electrochemical double-layer. After applying the voltage, the accumulation of charges on the electrode surfaces is started due to the potential difference. Following the natural attraction of unlike charges, ions in the electrolyte solution diffuse across the separator into the pores of the electrode of opposite charge. However, to prevent the recombination of the ions at electrodes, a double layer of charge is formed. These double-layers, coupled with an increase in surface area and a decrease in the distance between electrodes, allow EDLCs to achieve higher energy densities than conventional capacitors [43,46,47].

EDLCs can be operated with stable performance characteristics for many charge-discharge cycles, numerically it is almost 10^6 cycles but for the electrochemical batteries, this number reduced to only about 10^3 cycles. Due to the excellent cycling stability of EDLCs, these can be well suited for applications that involve non-user serviceable locations, such as deep sea or mountain environments [43,46,47].

The EDLC performance characteristics depend on both electrode materials and electrolytes. An EDLC can utilize either an aqueous or organic electrolyte. Aqueous electrolytes, such as KOH, and H_2SO_4 , usually have lower ESR and lower minimum pore size requirements compared to organic electrolytes, such as acetonitrile. One more thing that aqueous electrolytes also have lower breakdown voltages. Therefore, for choosing between an aqueous or organic

electrolyte, one should consider the adjustments between capacitance, ESR, and voltage [43,46–48]. Because of these adjustments, the choice of electrolyte often depends on the intended application of the supercapacitor.

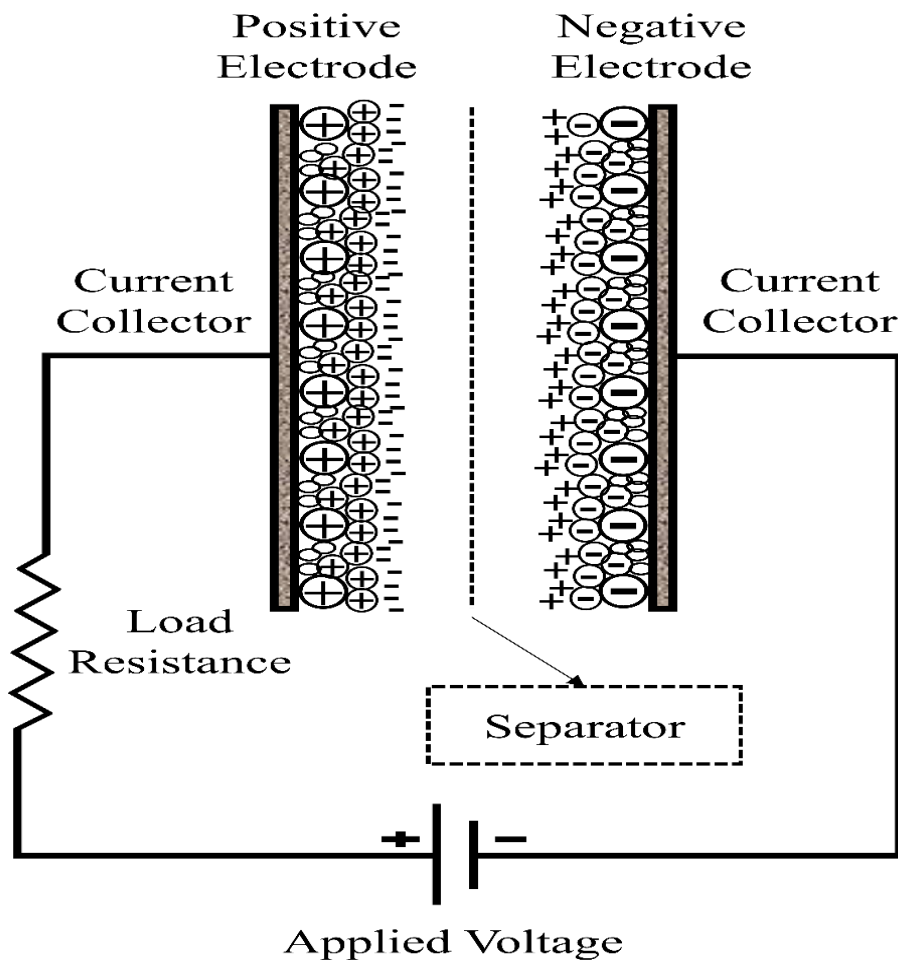


Figure 1.1.8. Schematic of an electrochemical double-layer capacitor.

The nature of the electrolyte is one of the great importance in supercapacitor design. The EDLCs subclasses are prominent mainly by the form of carbon they use as an electrode material. The carbon electrode materials got huge advantages over other materials due to the higher surface area, lower cost, and more traditional fabrication techniques are available, such as conducting polymers and metal oxides [43,46–48]. There are also some different forms of carbon materials available that can be used to store charge in EDLC electrodes are called activated carbons, carbon aerogels, and carbon nanotubes.

1.3.2.2. Pseudocapacitors

Generally, the EDLCs store charge electrostatically but pseudocapacitors store charge Faradaically through the transfer of charge between electrode and electrolyte. This is performed through reduction-oxidation reactions, electrosorption, and intercalation processes [46,49,50]. All of these Faradaic processes allow pseudocapacitors to gain greater capacitances and energy densities than EDLCs [51–53]. Two electrode materials namely conducting polymers and metal oxides are used to store charge in pseudocapacitors.

1.3.2.3. Hybrid

Hybrid capacitors are introduced to achieve the relative advantages and mitigate the relative disadvantages of EDLCs and pseudocapacitors to get better performance characteristics. Hybrid capacitor utilizes both Faradaic and non-Faradaic processes to store charge. As it can utilize both processes, hence, hybrid capacitors have achieved energy and power densities greater than EDLCs without the sacrifices in cycling stability and affordability that have limited the success of pseudocapacitors. Nowadays, research has focused on three different types of hybrid capacitors,

distinguished by their electrode configuration: composite, asymmetric, and battery-type respectively.

1.4. References

- [1] Nehra V, Kumar A, Dwivedi HK. Atmospheric Non-Thermal Plasma Sources. *Int. J. Eng.* 2008;2:53–68.
- [2] Kuwahara T, Okubo M, Kuroki T, et al. Odor removal characteristics of a laminated film-electrode packed-bed nonthermal plasma reactor. *Sensors.* 2011;11:5529–5542.
- [3] Pérès I, Pitchford LC. Current pulses in dc glow discharges in electronegative gas mixtures. *J. Appl. Phys.* 1995;78:774–782.
- [4] Mizuno A. Electrostatic precipitation. *IEEE Trans. Dielectr. Electr. Insul.* 2000;7:615–624.
- [5] Locke BR, Sato M, Sunka P, et al. Electrohydraulic discharge and nonthermal plasma for water treatment. *Ind. Eng. Chem. Res.* 2006. p. 882–905.
- [6] Jaworek A, Balachandran W, Krupa A, et al. Wet electroscrubbers for state of the art gas cleaning. *Environ. Sci. Technol.* 2006. p. 6197–6207.
- [7] Van Durme J, Dewulf J, Leys C, et al. Combining non-thermal plasma with heterogeneous catalysis in waste gas treatment: A review. *Appl. Catal. B Environ.* 2008;78:324–333.
- [8] Kumar S, Singh R, Singh TP, et al. Surface modification by electrical discharge machining: A review. *J. Mater. Process. Technol.* 2009;209:3675–3687.
- [9] Trichel GW. The mechanism of the negative point to plane corona near onset. *Phys. Rev.* 1938;54:1078.
- [10] El-Kishky H, Nindra BS, Abdel-Salam M, et al. Experience with development and evaluation of corona-suppression systems for HV rotating machines. *IEEE Trans. Dielectr. Electr. Insul.* 2002;9:569–576.
- [11] Kogelschatz U. Dielectric-barrier discharges: Their History, Discharge Physics, and Industrial Applications. *Plasma Chem. Plasma Process.* 2003;23:1–44.
- [12] Fridman G, Friedman G, Gutsol A, et al. Applied plasma medicine. *Plasma Process. Polym.* 2008;5:503–533.
- [13] Siemens W. Ueber die elektrostatische Induction und die Verzögerung des Stroms in Flaschendrähnten. *Ann. Phys.* 1857;178:66–122.

- [14] Rajasekaran P, Mertmann P, Bibinov N, et al. Filamentary and homogeneous modes of dielectric barrier discharge (DBD) in air: Investigation through plasma characterization and simulation of surface irradiation. *Plasma Process. Polym.* 2010;7:665–675.
- [15] Everaert K, Baeyens J. Catalytic combustion of volatile organic compounds. *J. Hazard. Mater.* 2004;109:113–139.
- [16] Xu X. Dielectric barrier discharge - Properties and applications. *Thin Solid Films.* 2001;309:237–242.
- [17] Kogelschatz U. Filamentary, patterned, and diffuse barrier discharges. *IEEE Trans. Plasma Sci.* 2002;30:1400–1408.
- [18] Nijdam S, van Veldhuizen E, Bruggeman P, et al. Plasma Chemistry and Catalysis in Gases and Liquids. *Plasma Chem. Catal. Gases Liq.* 2012.
- [19] Kim H-H. Nonthermal Plasma Processing for Air-Pollution Control: A Historical Review, Current Issues, and Future Prospects. *Plasma Process. Polym.* 2004;1:91–110.
- [20] Kim HH, Prieto G, Takashima K, et al. Performance evaluation of discharge plasma process for gaseous pollutant removal. *J. Electrostat.* 2002;55:25–41.
- [21] Johnson RE, Dettre RH. Contact Angle Hysteresis. III. Study of an Idealized Heterogeneous Surface. *J. Phys. Chem.* 1964;68:1744–1750.
- [22] Barthlott W, Neinhuis C. Purity of the sacred lotus, or escape from contamination in biological surfaces. *Planta.* 1997;202:1–8.
- [23] Lafuma A, Quéré D. Superhydrophobic states. *Nat. Mater.* 2003;2:457–460.
- [24] Chattopadhyay S, Huang YF, Jen YJ, et al. Anti-reflecting and photonic nanostructures. *Mater. Sci. Eng. R Reports.* 2010. p. 1–35.
- [25] Farhadi S, Farzaneh M, Kulinich SA. Anti-icing performance of superhydrophobic surfaces. *Appl. Surf. Sci.* 2011;257:6264–6269.
- [26] Raut HK, Ganesh VA, Nair AS, et al. Anti-reflective coatings: A critical, in-depth review. *Energy Environ. Sci.* 2011;4:3779.
- [27] Xue C-H, Jia S-T, Zhang J, et al. Preparation of superhydrophobic surfaces on cotton textiles. *Sci. Technol. Adv. Mater.* 2008;9:035008.
- [28] Zhang X, Shi F, Niu J, et al. Superhydrophobic surfaces: from structural control to functional application. *J. Mater. Chem.* 2008;18:621–633.
- [29] Genzer J, Efimenko K. Recent developments in superhydrophobic surfaces and their

- relevance to marine fouling: a review. *Biofouling*. 2006;22:339–360.
- [30] Jafari R, Menini R, Farzaneh M. Superhydrophobic and icephobic surfaces prepared by RF-sputtered polytetrafluoroethylene coatings. *Appl. Surf. Sci.* 2010;257:1540–1543.
- [31] Mukhopadhyay SM, Joshi P, Datta S, et al. Plasma assisted surface coating of porous solids. *Appl. Surf. Sci.* 2002;201:219–226.
- [32] Zhang J, Van Ooij W, France P, et al. Investigation of deposition rate and structure of pulse DC plasma polymers. *Thin Solid Films*. 2001;390:123–129.
- [33] Young T. An Essay on the Cohesion of Fluids. *Philos. Trans. R. Soc. London*. 1805;95:65–87.
- [34] Wenzel RN. Resistance of solid surfaces to wetting by water. *Ind. Eng. Chem.* 1936;28:988–994.
- [35] Cassie ABD, Baxter S. Wettability of porous surfaces. *Trans. Faraday Soc.* 1944;40:546–551.
- [36] Stoller MD, Park S, Yanwu Z, et al. Graphene-Based ultracapacitors. *Nano Lett.* 2008;8:3498–3502.
- [37] Ervin MH, Miller BS, Hanrahan B, et al. A comparison of single-wall carbon nanotube electrochemical capacitor electrode fabrication methods. *Electrochim. Acta*. 2012;65:37–43.
- [38] Pope MA, Korkut S, Punckt C, et al. Supercapacitor Electrodes Produced through Evaporative Consolidation of Graphene Oxide-Water-Ionic Liquid Gels. *J. Electrochem. Soc.* 2013;160:A1653–A1660.
- [39] Wang Y, Shi Z, Huang Y, et al. Supercapacitor Devices Based on Graphene Materials. *J. Phys. Chem. C*. 2009;113:13103–13107.
- [40] Miller JR, Simon P. Materials science: Electrochemical capacitors for energy management. *Science (80-.)*. 2008;321:651–652.
- [41] Wu NL. Nanocrystalline oxide supercapacitors. *Mater. Chem. Phys.* 2002;75:6–11.
- [42] Zhang LL, Zhou R, Zhao XS. Carbon-based materials as supercapacitor electrodes. *J. Mater. Chem.* 2009;38:2520–2531.
- [43] Kötzt R, Carlen M. Principles and applications of electrochemical capacitors. *Electrochim. Acta*. 2000;45:2483–2498.
- [44] Rajagopalan B, Chung JS. Reduced chemically modified graphene oxide for supercapacitor

- electrode. *Nanoscale Res. Lett.* 2014;9:1.
- [45] Sharma P, Bhatti TS. A review on electrochemical double-layer capacitors. *Energy Convers. Manag.* 2010;51:2901–2912.
- [46] Conway BE. *Electrochemical Capacitors: Scientific Fundamentals and Technological Applications.* Kluwer Acad. 1999.
- [47] Burke A. Ultracapacitors: Why, how, and where is the technology. *J. Power Sources.* 2000;91:37–50.
- [48] Frackowiak E, Béguin F. Carbon materials for the electrochemical storage of energy in capacitors. *Carbon N. Y.* 2001;39:937–950.
- [49] Conway BE. Transition from “Supercapacitor” to “Battery” Behavior in Electrochemical Energy Storage. *J. Electrochem. Soc.* 1991;138:1539–1548.
- [50] Conway BE, Birss V, Wojtowicz J. The role and utilization of pseudocapitance for energy storage by supercapacitors. *J. Power Sources.* 1997;66:1–14.
- [51] Mastragostino M, Arbizzani C, Soavi F. Polymer-based supercapacitors. *J. Power Sources.* 2001;97–98:812–815.
- [52] Kim I-H, Kim K-B. Ruthenium Oxide Thin Film Electrodes for Supercapacitors. *Electrochem. Solid-State Lett.* 2001;4:A62–A64.
- [53] Ryu KS, Kim KM, Park NG, et al. Symmetric redox supercapacitor with conducting polyaniline electrodes. *J. Power Sources.* 2002;103:305–309.

CHAPTER-2

Materials, methods and characterization

2.1. Introduction

The chapter has been discussed the detailed about the chemicals, gases, experimental methods, and the characterization processes used in this thesis. All the experimental works have been done in the laboratory to reach the research goal followed by physicochemical characterization and evaluation of the thin films and electrochemical properties of the obtained materials.

2.2. Materials and apparatus

In order to conduct an experiment, both materials and apparatus are needed. The detailed discussion about materials and apparatus are given below.

2.2.1. Materials

Materials in a reaction are the chemical reactants, solvents and catalysts used in the process. The chemicals were used in this thesis was research grade and were used without further purification. For example, when we require to measure the thickness of a wire using gauge, in this case, the wire uses as a material and screw gauge as an apparatus. The detailed list of materials and chemicals were used in this thesis are given in Table 2.1.1.

Table 2.1.1. List of chemicals used in this thesis.

Materials	Formula	Grade/Purity	Supplier
Hexamethyldisiloxane (HMDSO)	$O[Si(CH_3)_3]_2$,	$\geq 98\%$	Sigma-Aldrich Korea Co., Ltd.
Tetramethylsilane (TMS)	$Si(CH_3)_4$	$\geq 99\%$	Sigma-Aldrich Korea Co., Ltd.
(3-Aminopropyl)- triethoxysilane (APTES)	$H_2N(CH_2)_3Si(OC_2H_5)_3$	$\geq 98\%$	Sigma-Aldrich Korea Co., Ltd.
3-aminopropyl(diethoxy)- methylsilane (APDMES)	$CH_3Si(OC_2H_5)_2(CH_2)_3NH_2$	$\geq 97\%$	Sigma-Aldrich Korea Co., Ltd.
n-Heptane	C_7H_{16}	99.0%	Fisher Scientific

Nickel foam	Ni	-	MTI., Ltd., Korea
Ethanol	CH ₃ CH ₂ OH	99.9%	Fisher Scientific
Acetone	C ₃ H ₆ O	99.8%	Fisher Scientific
Soda lime glass	-	-	-
Argon	Ar	99.99%	-
Nitrogen	N ₂	99.99%	-

2.2.2. Apparatus

The apparatus are the tools which are used for measuring of a physical quantity required depending on the type of materials. All the apparatus used in this thesis are research grade. The detailed list of apparatus were used in this thesis are given in Table 2.1.2.

Table 2.1.2. List of apparatus used in this thesis.

Apparatus	Model/Specification	Manufacturer
FT-IR spectroscopy	FT-IR 7600	Lambda
UV-Vis Spectrophotometer	Mega-2100	SCINCO
Furnace	DFT-50300	DH Science
Pyrex flasks	-	-
Controlled heating mantle	HM1000C	Wissper

2MP 1000X 8 LED USB Digital Microscope Endoscope Zoom Camera	2MP 1000X 8 LED USB Digital Microscope	A4Tech
Home-made scratch tester	-	Home-made

2.3. Preparation of coating

The plasma-induced polymerization of different precursors was performed on soda-lime glass substrates and nickel foams with the dimensions of 75 mm × 27 mm × 1.2 mm. The flow rate of argon was typically 2.5 L/min, and that of nitrogen was also 2.5 L/min. Thus, the total gas flow rate was 5 L/min. Argon and nitrogen were separately fed into the system. The mass flow controllers (MFCs) were used to control the flow rates of the feed gases. The precursors contained in Pyrex flasks were delivered to the plasma reactor by bubbling them with argon. The concentration of precursors was changed from 135 to 8000 ppm (parts per million, volumetric) using its vapor pressure varying according to the temperature. The area of the coating was estimated to be around 1500 mm².

2.4. Materials synthesis

In this thesis, nickel foams were synthesis by the thermal process using furnace in the lab. For this study, n-heptane was used as precursor to deposit hydrocarbon on the nickel foam. The plasma treatment time was varied from 10 to 60 min to find the optimal coating thickness and then pyrolysis was performed under nitrogen environment at 700 °C for 5 hours to convert hydrocarbon to carbon on the nickel foam

2.5. Materials characterization

The nanomaterials were analyzed using several characterizations methods to identify the morphology, surface microstructure, crystal phase, size, composition, surface area, etc. The detailed experimental conditions are given below.

2.5.1. Atomic Force Microscopy (AFM)

The surface nanostructures of the coating were examined by atomic force microscopy (AFM, Nano Xpert II, EM4SYS, USA). One of the most important tools for imaging on the nanometer scale, Atomic Force Microscopy uses a cantilever with a sharp probe that scans the surface of the specimen. Atomic force microscopy will measure a number of different forces depending on the situation and the sample that you want to measure. As well as the forces, other microscopes can include a probe that performs more specialized measurements, such as temperature. Unlike rival technologies, it does not require either a vacuum or the sample to undergo treatment that might damage it.

2.5.2. Field-emission scanning electron microscopy (FE-SEM)

The SEM is routinely used to generate high-resolution images of shapes of objects (SEI) and to show spatial variations in chemical compositions: 1) acquiring elemental maps or spot chemical analyses using EDS, 2) discrimination of phases based on mean atomic number (commonly related to relative density) using BSE, and 3) compositional maps based on differences in trace element "activators" (typically transition metal and Rare Earth elements) using CL. The SEM is also widely used to identify phases based on qualitative chemical analysis and/or crystalline structure. The SEM have been used in this thesis was FE-SEM (Model: FE-SEM, JSM-

6700F, JEOL Ltd) with a 15 kV of acceleration voltage and 10 μ A of filament current. Prior to measurement, the as-prepared samples were fixed onto a double-face conducted tape mounted on a metal stud and coated with platinum with a sputter coater (Quorum Rotary-Pumped sputter coater -Q150R).

2.5.3. X-ray photoelectron spectroscopy (XPS)

The coating surface chemistry was analyzed using X-ray photoelectron spectroscopy (XPS). The chemical composition and the state of elements present in the outermost part of samples were obtained by X-ray photoelectron spectroscopy (XPS) techniques using ESCA- 2000, VG Microtech Ltd and Theta Probe AR-XPS system (Thermo Fisher Scientific, U.K). Here a monochromatic X-ray beam source at 1486.6 eV (Aluminum anode) and 14 kV was used to scan the sample surface. A high flux X-ray source with Aluminum anode was used for X-ray generation, and a quartz crystal monochromatic was used to focus and scan the X-ray beam on the sample.

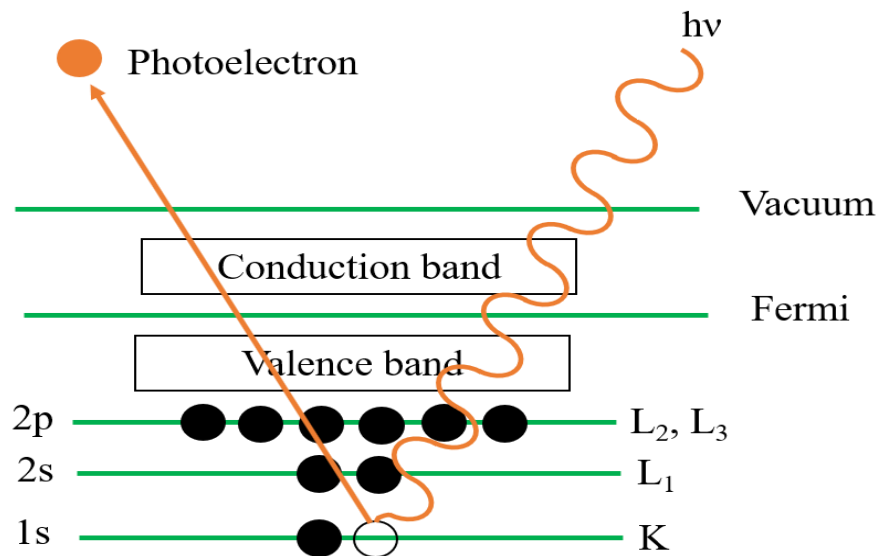


Figure 2.1.1. Principle of X-ray photoelectron spectroscopy.

2.4.4. Raman spectroscopy

The Raman spectrum is a non-damaging tool towards and sensitive technique the structural defects and disorders, crystallization in nanostructures. Further, it is also used to study the bonding nature of various carbon materials such as graphite and carbon nanotube. Raman spectra of the prepared FeCe_2O_4 and SrNiO_3 was studied using a Model: LabRam HR800 micro Raman spectroscopy (manufacturer: Horiba Jobin-Yvon, France). The Raman spectrum was operated at an excitation wavelength of 514 nm at the different laser power using Ar^+ ion laser. The spectral region of $100\text{--}3500\text{ cm}^{-1}$ was used to collect the data was using an acquisition time of 10-s data point.

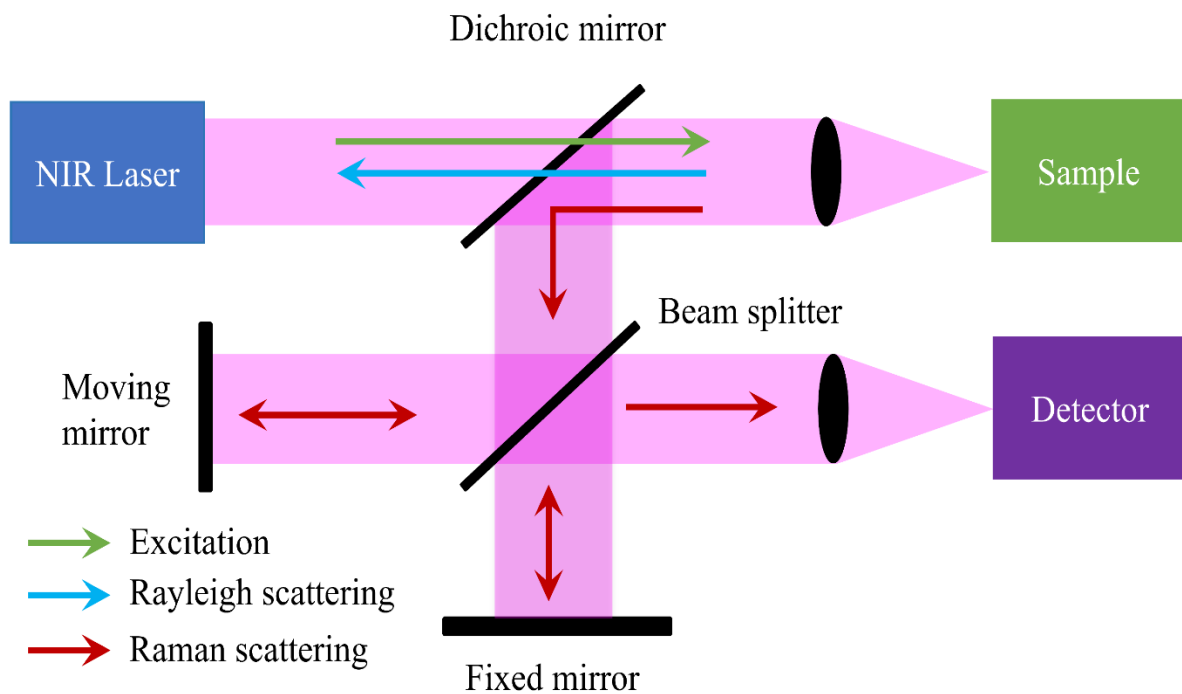


Figure 2.1.2. Simplified block diagram of the FT-Raman spectrometer.

2.4.5. X-ray diffraction (XRD)

X-ray diffractometer (XRD) is an essential analytical technique to determine the phase purity, the phase of the crystal, structure, and crystal size. The synthesized samples were performed by using (D/MAX 2200H, Bede 200, Rigaku Instruments C) X-ray diffractometer (XRD) operated at the power of 40 kV and current of 40 mA with Cu- α radiation in the range 2θ angle of 10-80° with a step of 0.02°.

2.4.6. Fourier transform infrared (FT-IR) spectrometer (XRD)

Fourier transform infrared spectroscopy (FTIR, FTIR-7600, Lambda Scientific, Australia) was used to investigate the composition of the effluent from the plasma jet and the deposited thin films. It is an important technique for the direct monitoring of interaction between adsorbed molecules and the materials. Since the soda-lime glass is not transparent to infrared (IR), polymer films were deposited on potassium bromide (KBr) disks by the same plasma polymerization process. All the spectra were collected by taking average of 10 scans at 1 cm^{-1} resolution in the range of 500–4000 cm^{-1} .

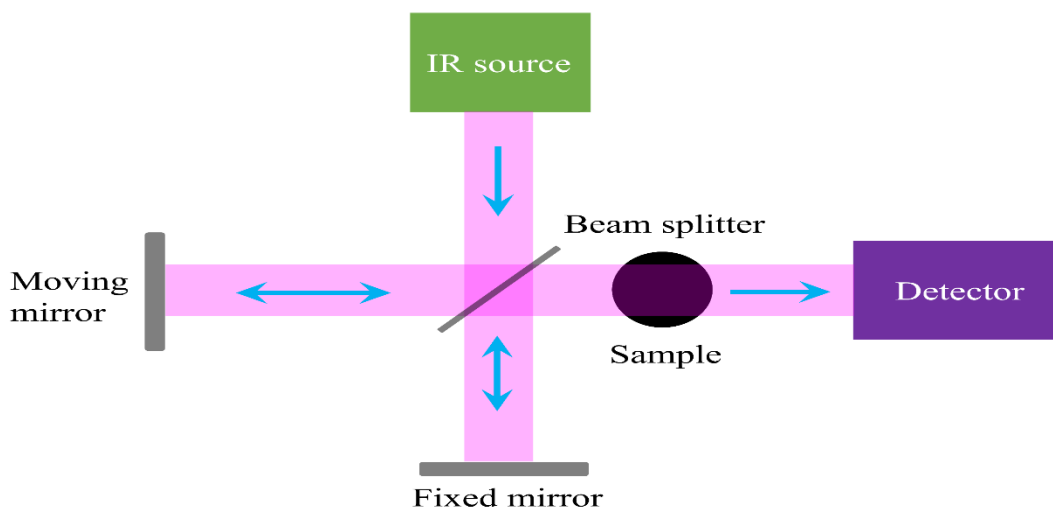


Figure 2.1.3. Schematic diagram of FTIR.

2.4.7. Flow controller units

This division is the first part of the set-up where the gas flow rates can be controlled through the mass flow controllers and blended in a cylinder mixer. A mass flow controller automatically controls the flow rate of a gas according to a set flow rate sent as an electric signal, without being affected by use conditions or changes in gas pressure. Flow rates can be roughly classified into two types: volumetric flow and mass flow. A volumetric flow measurement is affected by ambient temperature and pressure. All the mass flow controllers were used in thesis are manufactured by ATOVAC instruments (model AFC500). Their gas flows are adjusted through a manual control panel which is supplied by ATOVAC instruments (model GMC1200). The ranges of the mass flow were used from 10 to 5000 ml min⁻¹. Each and every controller was calibrated for all gases that were expected to be used with a bubble flow meter and checked regularly.



Figure 2.1.4. (a) Mass flow controller and (b) Pressure & Flow controller.

2.4.8. Nano View 2400

NV-2400 is the fast non-contact 3D profiler for all kinds of surface. X/Y stage is automated but Z axis is manual. NanoSystem designs it mainly for R&D, universities and process management users. NanoSystem creates H/W and S/W with its own patented algorithms and White Light Interferometry. It can measure large field of view (500 mm²) by stitching function. The patented WSI/PSI technology measures a wide variety of surface materials and parameters, including 2D and 3D profiling of surface texture, form, step-height and more (0.1 nm - vertical and 0.2 um-lateral resolution) patented WSI/PSI technology measures a wide variety of surface materials and parameters, including 2D and 3D profiling of surface texture, form, step-height and more (0.1 nm - vertical and 0.2 um-lateral resolution).



Figure 2.1.5. NV-2400 3D nano-profiler system.

CHAPTER-3

Robust hydrophobic coating on glass surface by an atmospheric-pressure plasma jet for plasma-polymerization of hexamethyldisiloxane conjugated with (3-aminopropyl) triethoxysilane

Highlights

- DBD configuration used to make hydrophobic surface.
- HMDSO and APTES used as precursors to study the coating layers.
- Robust coating layer formed on the glass surface with uniform thickness.
- Deposition was confirmed by FE-SEM and AFM.
- No significant loss in the visibility region.

3.1. Introduction

Nonthermal plasma (NTP) treatment at atmospheric pressure has been a warm research topic in recent years for making hydrophobic surface of various materials [1–7]. The hydrophobic surface can be used for various purposes such as self-cleaning windows, anti-icing, out-door textiles, self-cleaning of antennas, ultra-dry surface applications, protection of circuits and grids, medical devices, and other optical apparatuses [8–12]. Basically, the thin films deposited by plasma polymerization are pinhole free, have good adhesion, and have better mechanical and chemical stabilities. To get hydrophobic characteristics the surface requires nano- to micro-scale roughness. Both the surface roughness and the surface chemistry affect the hydrophobicity [2]. Up to now, several methods have been proposed to generate surface roughness, including plasma treatment, sol-gel deposition, anodization, electrodeposition, chemical treatment, hot-water immersion, and lithography [12–17]. A surface having water contact angle (WCA) from 90° to 150° is known as hydrophobic, and the surface more than 150° is known as superhydrophobic due to its excellent self-cleaning ability.

Although low surface energy materials such as fluorocarbons can be used to produce hydrophobic coatings [14,18,19], the plasma polymerization of silicon-based compounds is more environmentally friendly. This study has dealt with the plasma polymerization of hexamethyldisiloxane (HMDSO, $C_6H_{18}OSi_2$) and (3-aminopropyl)triethoxysilane (APTES, $H_2N(CH_2)_3Si(OC_2H_5)_3$) at atmospheric pressure. The main purpose of using the two precursors is to increase not only hydrophobicity but also robustness of the coating. As well known, one of the major drawbacks of the silicon compound coatings is their poor mechanical abrasion which extinguishes the self-cleaning function due to the damage of surface roughness and coating layer. HMDSO is generally used to promote hydrophobicity, but due to its poor adhesion to metal or

inorganic material, the long-term stability of the coating layer is not satisfactory. Hence, APTES is used with HMDSO to overcome this issue but the cost is to sacrifice the WCA as it is known that APTES is hydrophilic in nature. Basically, organosilane reagents are commonly used to produce functionalized thin films on silicon oxide and other substrates for a variety of technological applications. APTES is one of the similar aminosilanes which is used in this study to facilitate production of arrays of metal nanoparticles on silica substrates [20]. For surface coating, APTES is highly suggested to use for its covalent attaching to silica (SiO_2), titania (TiO_2), organic films, and metal oxides [2]. Masuko et al. [21] studied the shear strength and durability of self-assembled monolayer (SAM) and the tribological performance with different numbers of siloxane bonds on smooth silicon substrates. They found that increasing the number of siloxane bonds of SAMs gives more stable surface with low friction and greater durability. One of the key parameters explored in this work was the ratio of HMDSO to APTES.

3.2. Experimental

Schematic diagrams of the plasma polymerization system and homemade scratch tester are shown in Figure 3.1.1. The plasma reactor was made of a glass tube and two stainless steel needles acting as the high voltage (HV) electrode. The HV electrode was powered by an AC power source (Korea Switching Co.) with an operating frequency of 11.5 kHz. The inner and outer diameter of the glass tube was 5.0 and 8.0 mm, respectively. The distance between HV electrode tip and the end of the reactor glass tube was kept constant at 75 mm. The gap between the end of the tube and the substrate was kept constant at 2 mm. The substrate samples held on a Teflon plate reciprocated below the stationary plasma jet at a speed of 90 mm/s. Argon (99.99%) and nitrogen (99.99%) were used as the carrier and shielding gas, and they were separately fed into the system as shown

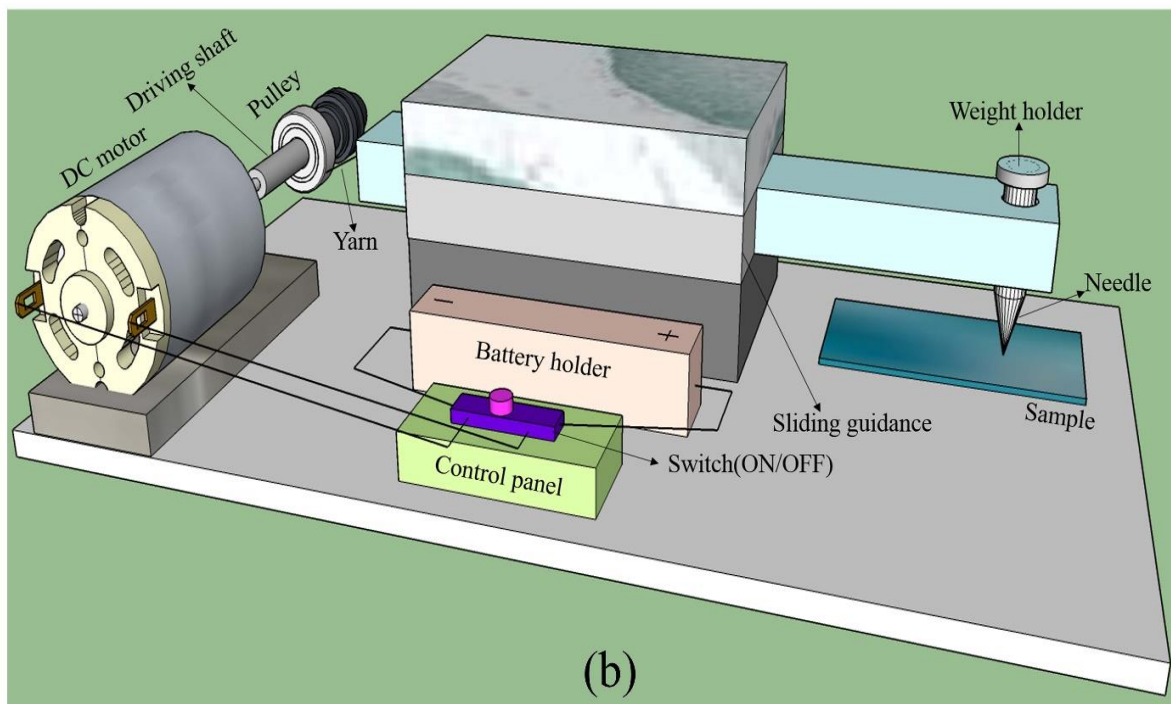
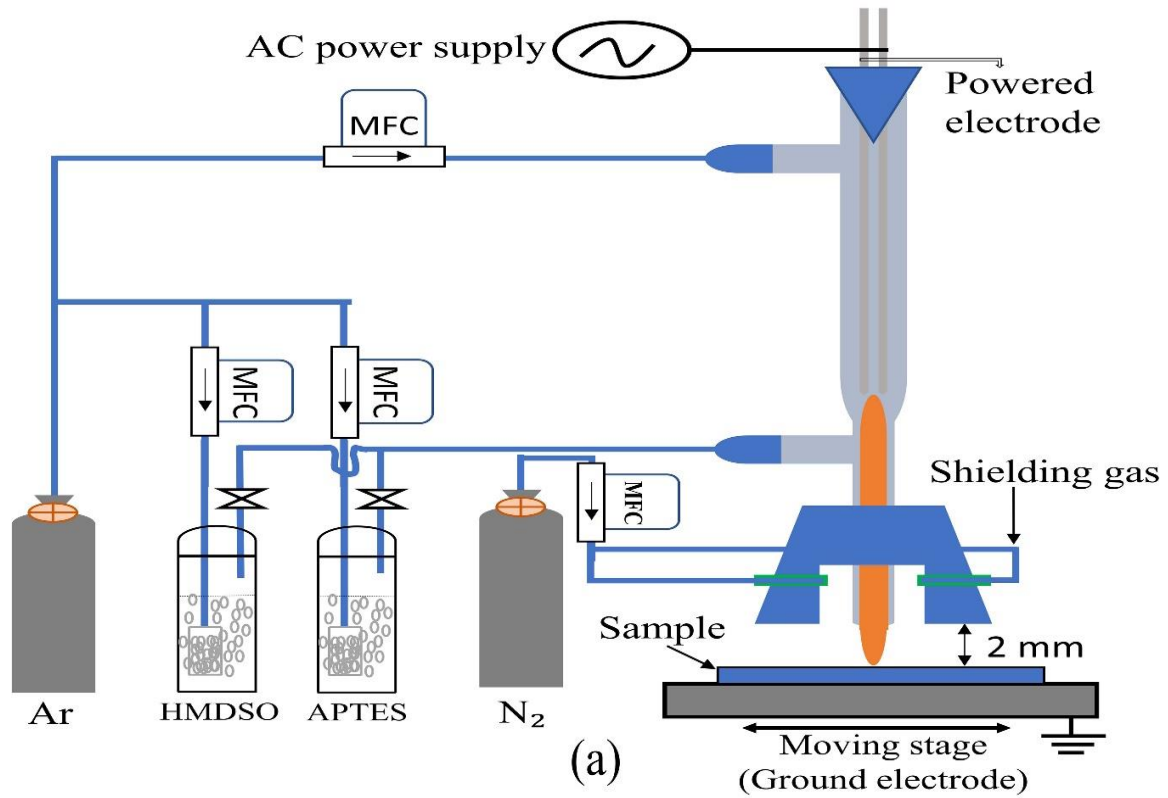


Figure 3.1.1. Schematic diagrams of (a) the experimental setup and (b) home-made scratch tester.

in Figure 3.1.1(a). The purpose of using the shielding gas was to protect the plasma jet from the interference of oxygen and water vapor diffused from ambient air. The two precursors, namely, HMDSO and APTES were purchased from Sigma-Aldrich Korea Co., Ltd. HMDSO was used to promote hydrophobicity while APTES to promote mechanical robustness.

The appropriate condition was determined based on the parametric study with several key parameters such as treatment time, applied voltage, gas flow rate, and the ratio of two precursors. The treatment time was changed from 30 to 120 s, and the effect of applied voltage was examined from 5 to 8 kV. The total concentration of the precursors was set to 280 ppm (parts per million, volumetric). The concentration of HMDSO was 280 ppm in the HMDSO-alone case (H100); in the APTES-alone case (A100), the concentration was also the same.

The HMDSO/APTES (H/A) ratio was varied by 3/1, 1/1, and 1/3. Both precursors were delivered to the jet by bubbling HMDSO and APTES (at 25 and 121°C, respectively) contained in Pyrex flasks using argon gas. The flow rate of the shielding gas was fixed at 2.5 L/min, and the effect of the flow rate of argon on the coating was examined in the range of 0.5–4.5 L/min. Thus, the total flow rate of argon and nitrogen was changed from 3.0 to 7.0 L/min. The substrates for coating were soda-lime glasses with dimensions of 75 mm × 27 mm × 1.2 mm, and thus the resulting coated area was estimated to be around 1500 mm².

The WCA of the coated surfaces was measured for understanding the hydrophobicity of the coated surface polymer. The WCA measurements were carried out on a goniometer (Phonix 300, Surface & Electro Optics Co., Ltd., Korea) using sessile drop technique by dropping about 10 μL of distilled water on the sample's surfaces. The surface morphology was seen by scanning electron microscopy (SEM, JSM-6700F, JEOL, Japan) at an operating voltage of 15 kV. The surface nanostructures of the coating were examined by atomic force microscopy (AFM, Nano

Xpert II, EM4SYS, USA). Fourier transform infrared spectroscopy (FTIR, FTIR-7600, Lambda Scientific, Australia) was used to investigate the composition of the effluent from the plasma jet and the deposited thin films. The coating surface chemistry was analyzed using X-ray photoelectron spectroscopy (XPS). The coating layer robustness was performed by home-made scratch tester and wear tracks were observed by an optical microscope (2MP 1000X 8 LED USB Digital Microscope Endoscope Zoom Camera, A4Tech, Taiwan). For a typical scratch test, a diamond tip moves over the surface to make a scratch with either constant or progressively increasing load [22]. Usually, the normal force, tangential force, friction coefficient, acoustic emission, and penetration depth are measured continuously during scratch testing [22]. Figure 3.1.1(b) shows the home-made scratch tester used in this work to examine the robustness of the coating. The scratch tester is mainly composed of a DC motor which drives a needle (tip diameter: 0.5 mm) to move on the sample's surface for creating scratch with predetermined vertical loads. Yarn is used to connect motor's driving shaft to the needle holder. The needle holder is guided by a sliding guide and it can travel horizontally back and forth. The samples for testing were put under the tip of the needle and fixed by double-sided tape so that the samples did not move during scratching. The tip of the needle was cleaned with ethanol and tissue wiper before and after a scratch test for each sample. The moving speed of the tip was set to 37 mm/s and the length of scratch was around 10 mm. For every sample, constant loads were applied every time to determine the breakdown force for the coating layer.

3.3. Results and discussion

3.3.1. Water contact angle measurements of the glass substrates

The surfaces with different degrees of hydrophobicity were observed after the plasma polymerization process, depending on the operating conditions including the applied voltage, the gas flow rate, the HMDSO/APTES (H/A) ratio, and the treatment time. Figure 3.1.2 shows the dependence of WCA on the treatment time, the applied voltage, the H/A ratio and the gas flow rate. The WCA results reported in Figure 3.1.2 are the average values of five measurements at each condition. In detail, Table 3.1.1 summarizes the values of the experimental parameters, the average WCAs and the standard deviations.

The effect of treatment time was examined from 30 to 120 s at a H/A ratio of 3/1 with the applied voltage and the total gas flow rate kept constant at 7 kV and 6 L/min, respectively. As shown in Figure 3.1.2(a), the WCA was varied from 100° to 141° by changing the treatment time within the investigated range. Basically, WCA depends on surface roughness and thickness. At a short treatment time of 30 s, the surface roughness and coverage were relatively poor, compared with 45–120 s treatment time. Increasing the treatment time can allow more deposition on the surface, which increases thickness, surface coverage and roughness. After a certain limit, however, thickness may increase but surface coverage and roughness remain similar and hence the WCA does not increase. In this experiment, the WCA increased from 100° to 143° with increasing the treatment time from 30 to 60 s, but further increasing the treatment time hardly affected the WCA. Thus, 60 s was chosen for the treatment time.

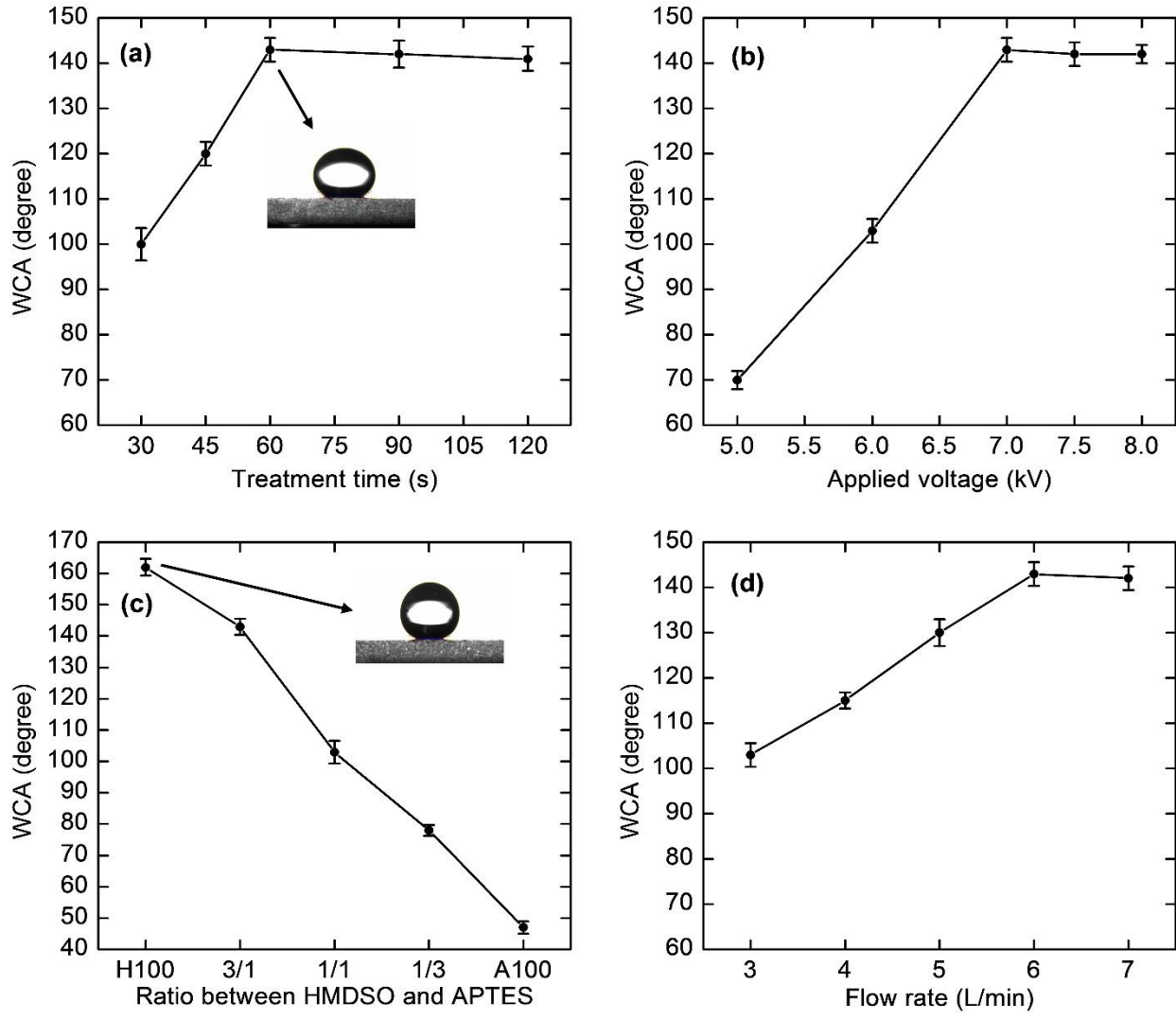


Figure 3.1.2. Dependence of WCA on (a) the treatment time, (b) the applied voltage, (c) the H/A ratio and (d) the gas flow rate.

Table 3.1.1. Operating conditions and WCA measurement results.

Treatment time (s)	Applied voltage (kV)	H/A ratio (-)	Gas flow rate (L/min)	Average WCA (degree)	Standard deviation
30	7.0	3/1	6	100	2.4
45	7.0	3/1	6	120	2.1
60	7.0	3/1	6	143	2.6
90	7.0	3/1	6	142	2.4
120	7.0	3/1	6	141	2.1
60	5.0	3/1	6	70	2.5
60	6.0	3/1	6	103	2.7
60	7.0	3/1	6	143	2.6
60	7.5	3/1	6	142	2.8
60	8.0	3/1	6	142	2.7
60	7.0	H100	6	162	3.1
60	7.0	3/1	6	143	2.6
60	7.0	1/1	6	101	2.8
60	7.0	1/3	6	78	2.5
60	7.0	A100	6	47	2.1
60	7.0	3/1	3	103	2.7
60	7.0	3/1	4	115	2.2
60	7.0	3/1	5	130	2.3
60	7.0	3/1	6	143	2.6
60	7.0	3/1	7	142	2.6

In the second step, the effect of applied voltage was examined from 5 to 8 kV with the treatment time, the H/A ratio, and the total flow rate kept constant at 60 s, 3/1, and 6 L/min, respectively. As in Figure 3.1.2(b), the WCA increased with raising the applied voltage from 5 to 7 kV and then leveled off. Generally, the higher the applied voltage, the more intense the plasma was, leading to the enhancement in the deposition rate and the formation of particulates in the plasma gas phase, called dusty plasma which is prerequisite to obtain rough surfaces. The highest WCA were measured to be 143° at 7 kV. There was no significant change in the WCA at higher applied voltages. From the results obtained, the applied voltage of 7 kV was chosen for the appropriate applied voltage.

The third step was to see the effect of the H/A ratio on the WCA. The treatment time and the applied voltage chosen above were 60 s and 7 kV, respectively. Figure 3.1.2(c) shows the dependence of WCA on the H/A ratio with the treatment time and applied voltage kept constant at 60 s and 7 kV, respectively. The WCA values of the coatings formed from the single precursor of APTES and HMDSO are also added for the purpose of comparison. It is natural that the WCA should decrease with increasing the content of APTES in the mixture of the two precursors due to its hydrophilic character, which has been confirmed by the low WCA of the A100 coating.

Lastly, the gas flow rate was changed to understand its effect on the WCA while the treatment time, the applied voltage, the H/A ratio were kept constant at 60 s, 7 kV, and 3/1, respectively. In Figure 3.1.2(d), it was observed that by increasing the total gas flow rate from 3 to 6 L/min the plasma was getting more intense, leading to an increased WCA from 103° to 143°. But further increases of the feed gas flow rate to 7 L/min did not noticeably change the WCA, and hence 6 L/min was chosen for the optimal gas flow rate.

3.3.2. Coating stability test

Coating stability was examined by performing natural and thermal aging. All the plasma-treated samples were stored in centrifuge tube at room temperature. The aging time was reported to have a significant effect on WCA for the powder substrate coating [23]. Trinh et al. [23] have reported that the WCA could increase by 15–40° within 30 days in the case of powder substrate coating. Unlike the powder substrate coating, the WCA of the plasma-treated substrate (glass) as shown in Figure 3.1.3(a) was hardly affected by the aging (15, 30, and 90 days), indicating that the coating is highly stable and durable. The thermal stability of the coating was examined by annealing tests at 200°C and 250°C for one hour. The WCA did not nearly change in both cases, as shown in Figure 3.1.3(b).

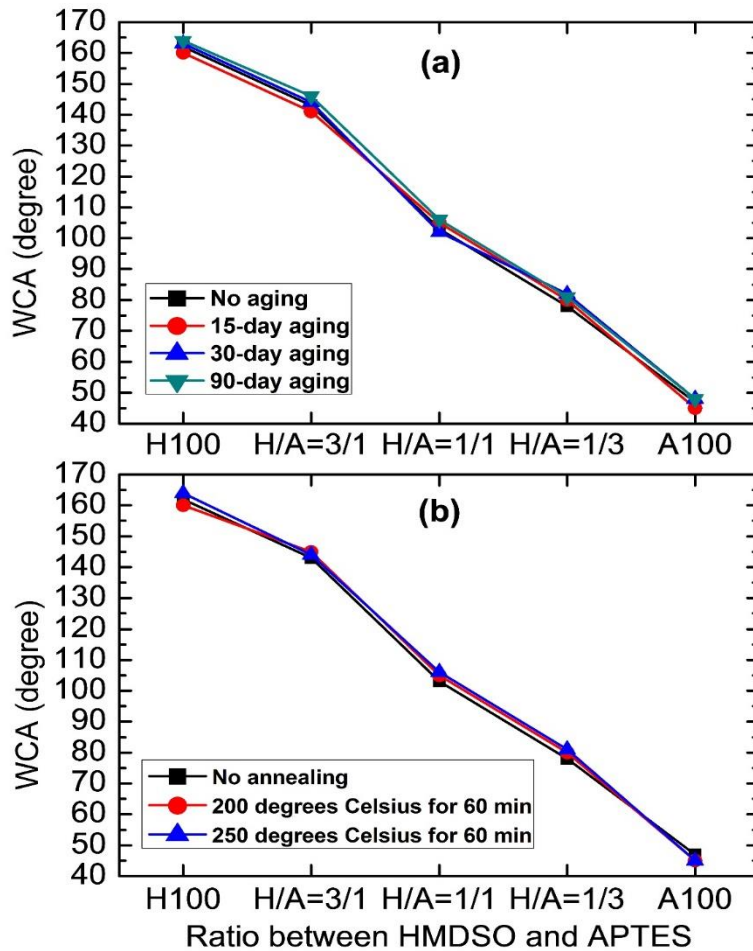


Figure 3.1.3. (a) Aging time effect and (b) annealing temperature.

3.3.3. Surface morphology and coating thickness

The AFM and SEM analyses were carried out to understand the relationship between the two precursors in the plasma polymerization process as well as to see the surface morphology, roughness and thickness of the coating. Root-mean-square (RMS) roughness and coating thickness are listed in Table 3.1.2.

Table 3.1.2. Thickness and RMS roughness of each sample.

Sample	Thickness (nm)	RMS roughness (nm)
H100	420	182±5
H/A=3/1	370	123±6
H/A=1/1	317	86±4
H/A=1/3	275	48±4
A100	215	36±5

Figure 3.1.4 shows the AFM results of the coated samples for H100, A100 and various H/A ratios. From the figure, it can be seen that the number of needle-like peaks grown on the substrate surfaces decreased from Figure 3.1.4(a–e). The higher the number of needle-like peaks, the higher the surface roughness. The H100-alone coating (Figure 3.1.4(a)) had the highest surface roughness and thickness and it is likely due to the hydrophobic nature and reactivity of HMDSO in the plasma. When HMDSO and APTES were added together, the roughness and coating thickness decreased as the H/A ratio decreased. The formation of rough surfaces with nanoscale topographic features results from the generation of particulates through gas-phase condensation reactions. The plasma-induced particulates then deposit and adhere to a substrate [5]. In the plasma polymerization, it is believed that HMDSO is more active than APTES to produce fragments, facilitating the formation of particulates and therefore the high surface roughness.

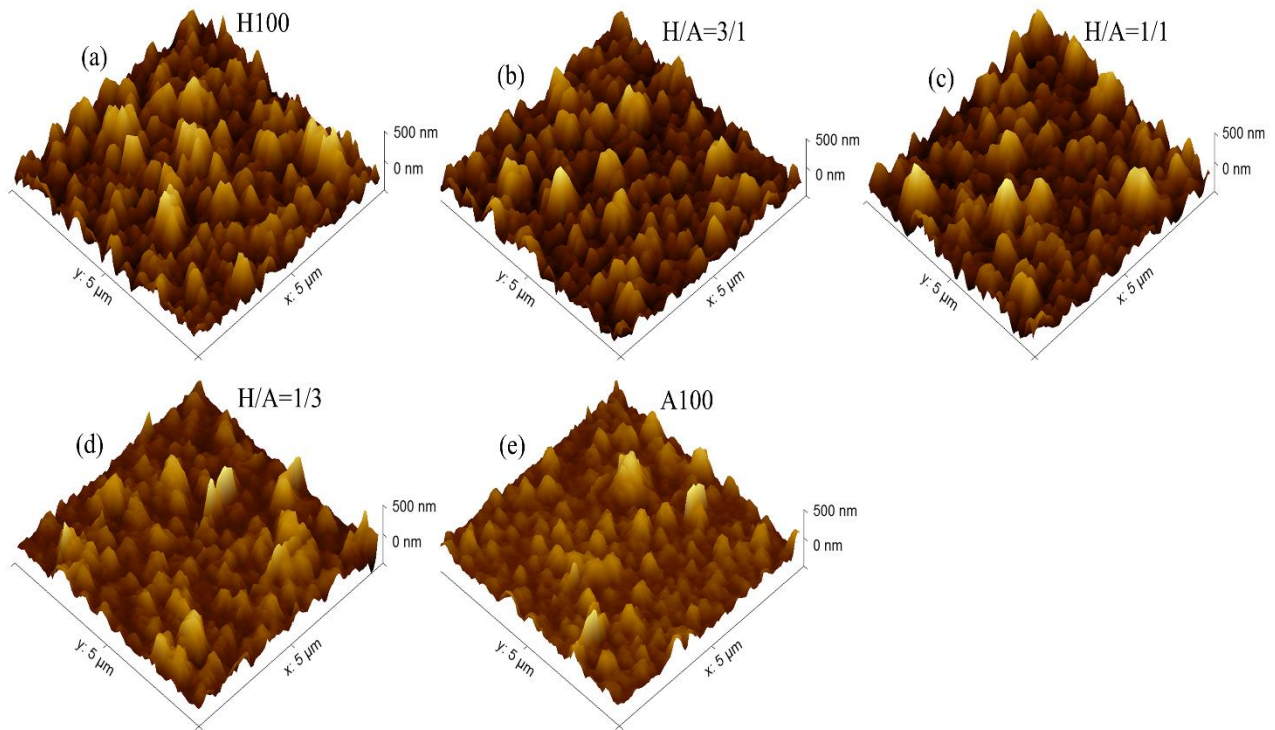


Figure 3.1.4. AFM images of the coated samples. (a) H100; (b) $H/A = 3/1$; (c) $H/A = 1/1$; (d) $H/A = 1/3$; and (e) A100.

Figure 3.1.5 shows SEM images of the corresponding samples. The coatings consist of nanostructures ranging from 70 to 200 nm. It was found that the coatings had shown cauliflower-like morphology in the case of H100 and the H/A ratio of 3/1 (Figure 3.1.5(a,b), respectively), while in the other cases the nanostructures formed were like numerous circular islands with different sizes.

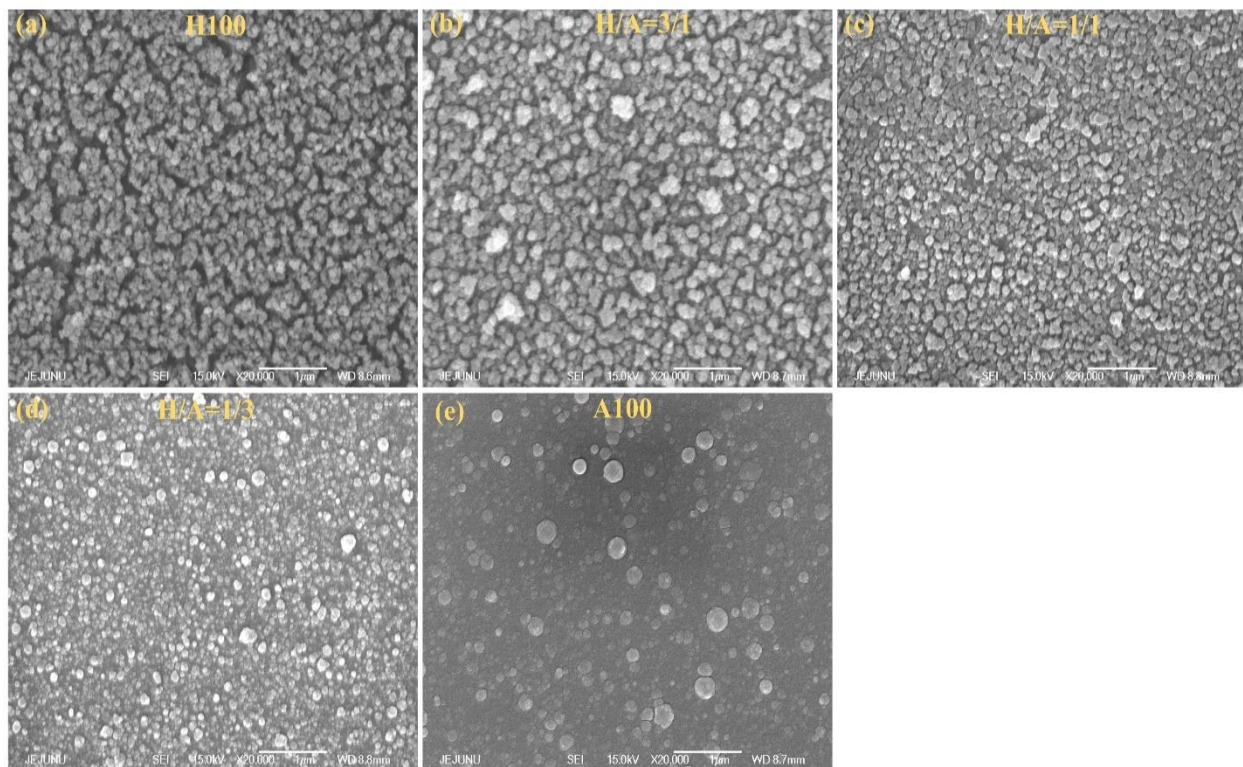


Figure 3.1.5. SEM images of the coated samples. (a) H100; (b) H/A = 3/1; (c) H/A = 1/1; (d) H/A = 1/3; and (e) A100.

3.3.4. Surface modification by APTES

Plasma polymerization with amines is still under investigation and only a few articles discussed about this issue [24–28]. The plasma polymerization by the APTES is described in Figure 3.1.6 [29–31]. For better understanding, the surface modification by the APTES can be divided into three parts: (a) hydrogen bonding due to initial adsorption, (b) surface attachment, and (c) multilayer formation [31]. If we take a careful look at Figure 3.1.6(a,b), it can be seen that still there is no sign of donor amine and acceptor groups. It indicates that some of APTES molecules are not H-bonded to the surface. Hence, the formation of siloxane cross-links depends on the inter-APTES reaction and makes a thin layer (Figure 3.1.6(c)) where donor amine and acceptor H-bond both are present.

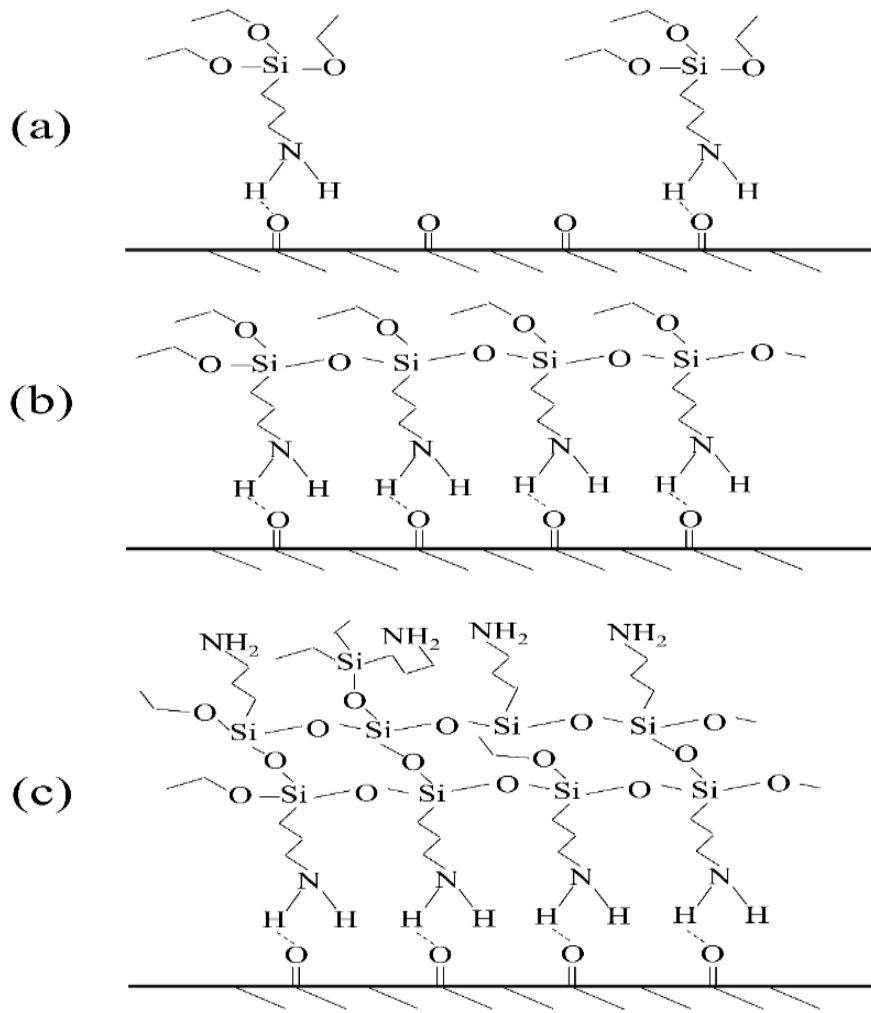


Figure 3.1.6. Surface modification and possible reaction routes of APTES: (a) hydrogen bonding due to initial adsorption, (b) surface attachment, and (c) multilayer formation.

3.3.5. FTIR spectroscopy

The chemical characterizations of the coatings were done by the FTIR spectroscopy, which are shown in Figure 3.1.7. Since the soda-lime glass is not transparent to infrared (IR), polymer films were deposited on potassium bromide (KBr) disks by the same plasma polymerization process. All the spectra were collected by taking average of 10 scans at 1 cm^{-1} resolution in the range of $500\text{--}3500\text{ cm}^{-1}$.

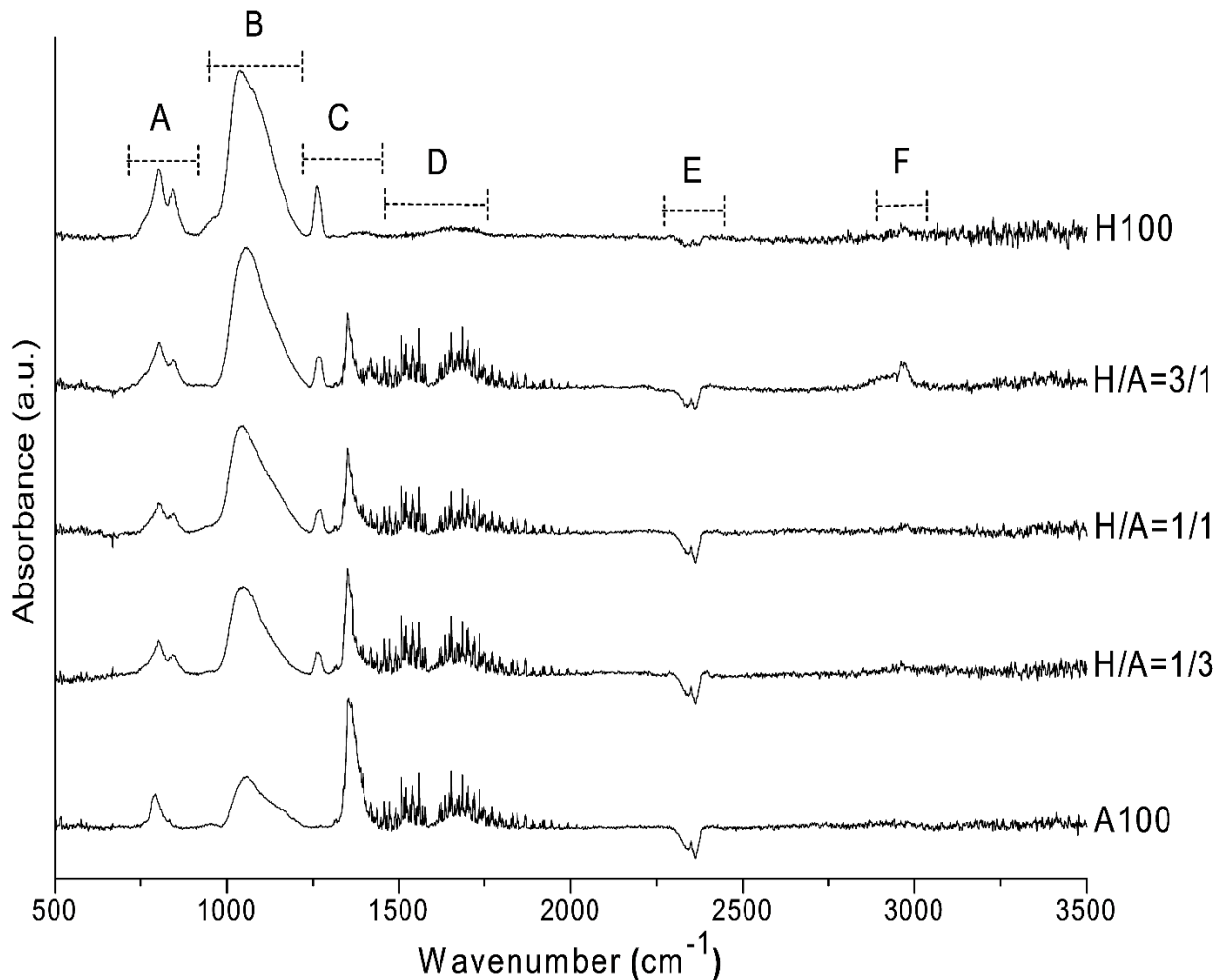


Figure 3.1.7. FTIR spectra of the coated samples from 500 to 3500 cm^{-1} .

The asymmetric stretching band of the backbone Si–O–Si is found at 1047 cm^{-1} [32,7]. Si–O stretching in Si–OH can be seen at $830\text{--}940\text{ cm}^{-1}$ [7,33,34], and Si–C stretching is found at 800 cm^{-1} [7]. The Si–CH₃ symmetric deformation appears at $1260, 1350, \text{ and } 2966\text{ cm}^{-1}$ where the peaks at 1260 and 1350 cm^{-1} are medium in intensity and the peak at 2966 cm^{-1} is weak in intensity [32,35]. The absorption band at 1600 cm^{-1} that corresponds to water is due to the moisture of KBr. Peaks from 2340 to 2360 cm^{-1} are due to the presence of CO₂ in the ambient environment [36].

3.3.6. XPS results

The XPS examination was done to understand the surface chemical composition and the chemical bonds of the polymer thin films. Figure 3.1.8 demonstrates the atomic concentrations measured by the XPS for various specimens. Three samples out of five were selected (H100, A100, and H/A = 3/1) for XPS analyses where all the three samples contain silicon (Si), carbon (C), oxygen (O), and nitrogen. The H100 sample has shown 37.5% of carbon, 33.5% of oxygen, 27.1% of silicon, and 1.9% of nitrogen. On the other hand, APTES (A100) and the H/A ratio of 3/1 coated sample have shown 20.9% and 40.2% of carbon, 50.1% and 37.9% of oxygen, 24.6% and 18.8% of silicon, and 4.4% and 3.1% of nitrogen, respectively. Here, sample H100 has shown less nitrogen when compared to the other two samples, which is due to no nitrogen from the precursor. The deconvolution results of C1s spectra are presented in Figure 3.1.9 and Table 3.1.3. The plasma polymerized thin film shows a high contribution of the Si–CH_x ($x = 3$ or 2) or C–C at 284.6 eV in the all three samples in Figure 3.1.9 [37,38]. The peaks at 286 and 287.5 eV are seen due to the presence of C–O or C–N and C=O in all the coated samples [37]. But, C–Si_x ($x = 3$ or 2) peak at

Table 3.1.3. Deconvolution of C1s spectra along with binding energies and functional groups.

Functional groups	Peak Position (eV)	References
C-Si _x (x=3 or 2)	283.2	[37]
Si-CH _x (x=3 or 2) or C-C	284.6	[37,38]
C-O or C-N	286	[37]
C=O	287.5	[37]
O-C-O	288.7	[37]

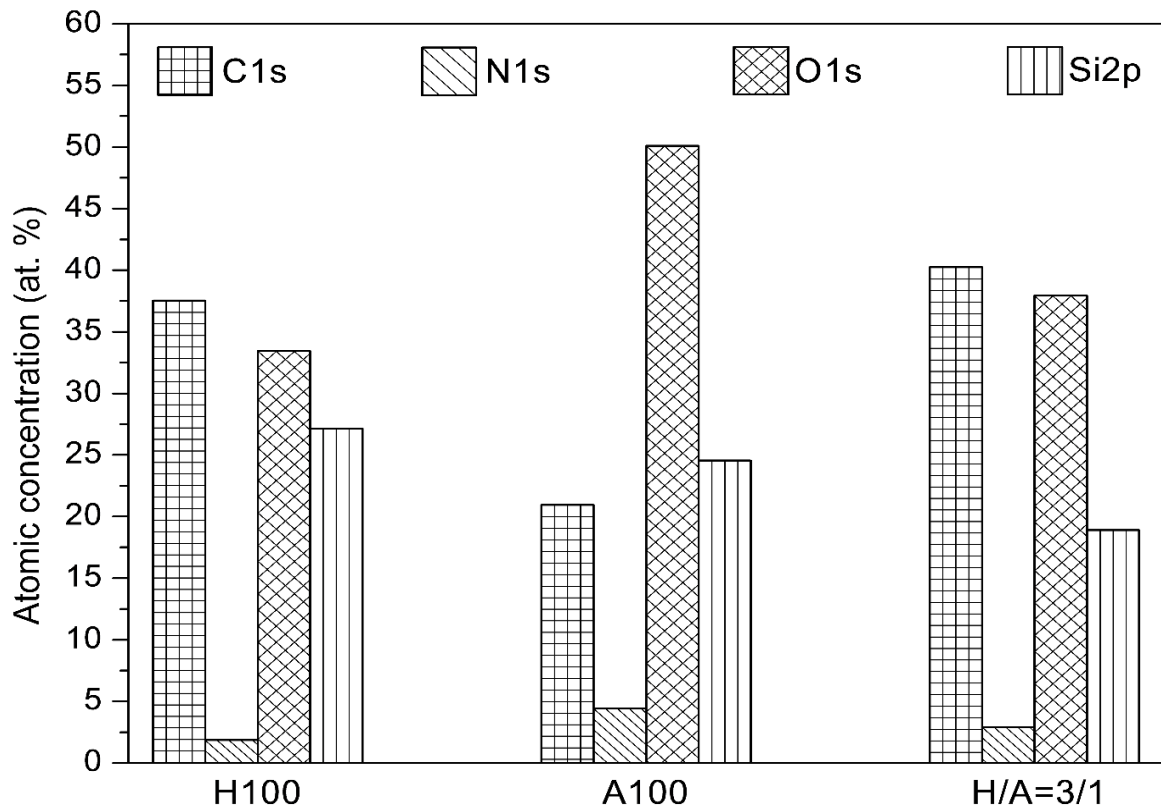


Figure 3.1.8. Atomic composition (%) of selected sample surfaces.

283.2 eV is found only in the sample H100 and H/A ratio of 3/1 in Figure 3.1.9(a,c) [37]. So, it could be said that this chemical bond is generated due to the HMDSO precursor. On the other hand, the chemical bonding of O–C–O at 288.7 eV in Figure 3.1.9(b,c) is due to the APTES precursor [37].

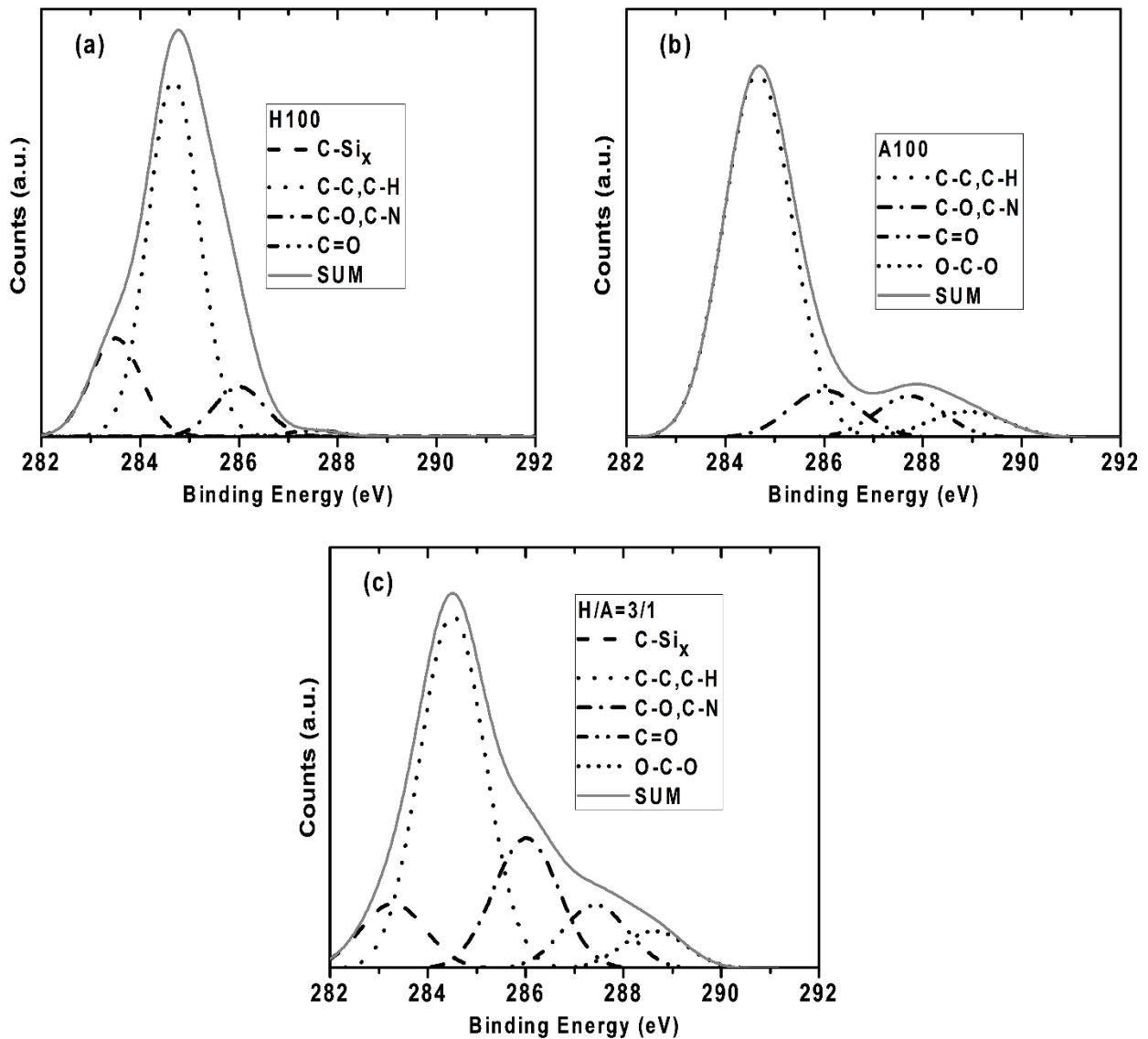


Figure 3.1.9. Deconvolution of C1s spectra (282–290 eV) of the selected coated samples.

3.3.7. UV-visible spectroscopy

Transmittance and hydrophobicity have an inverse relationship because both depend on the thickness and roughness of the coating. As the surface thickness and roughness of the coating increase, the hydrophobicity increases but the visibility decreases [39]. Figure 3.1.10 shows the UV–VIS transmission spectra of the bare glass and the ones coated with HMDSO, APTES, and their mixture at various ratios [39]. Uncoated glass exhibited around 80% transmittance in the visible regions (from 390 to 700 nm), while the plasma-treated glasses at different H/A ratios exhibited slightly lower transmittance.

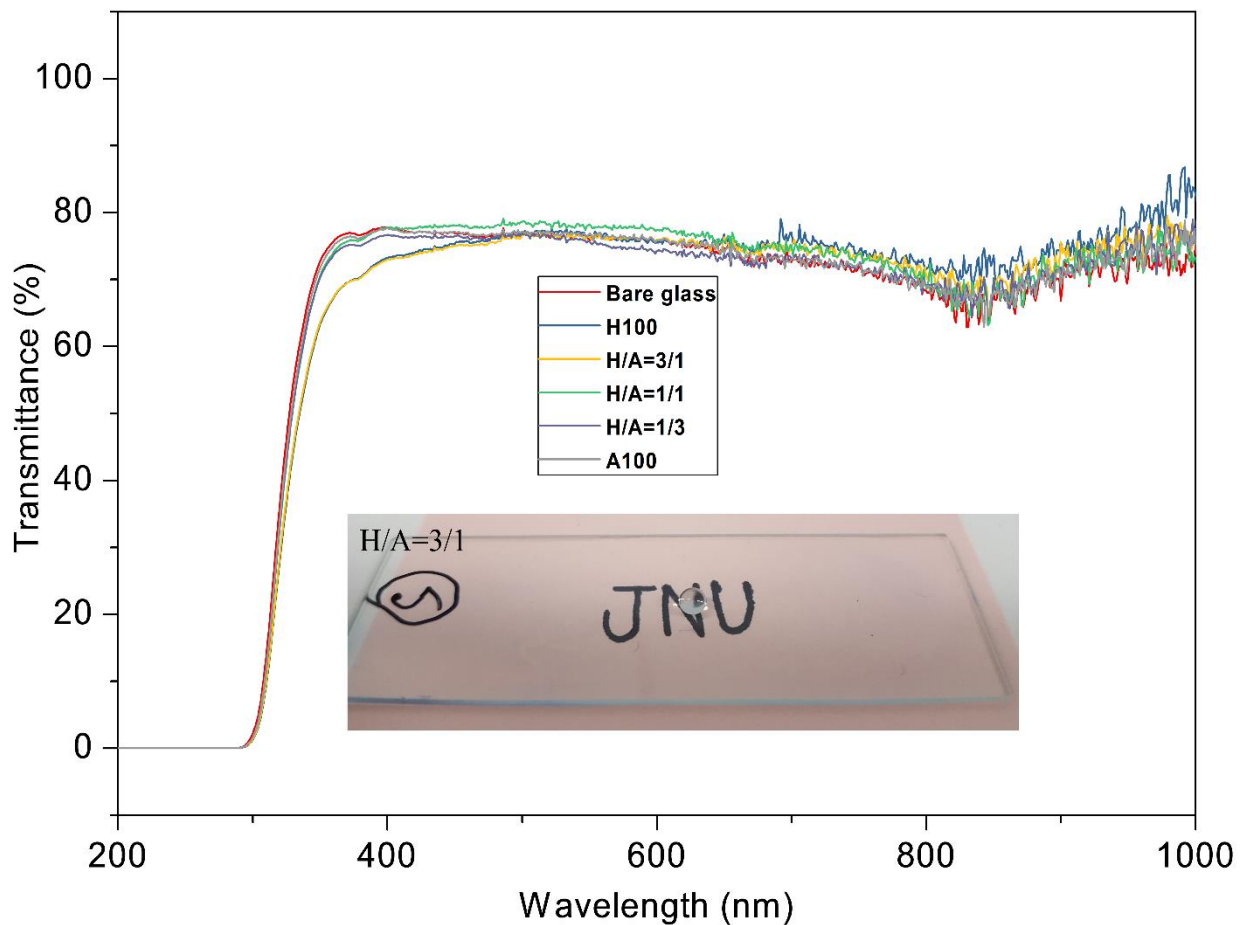


Figure 3.1.10. UV-visible spectra of the coated samples.

3.3.8. Scratch tests

To analyze the mechanical robustness of the coatings, scratch tests were performed after the annealing of the samples at 250°C for 1 h. All the experimental conditions for the scratch test are summarized in Table 3.1.4. The weight of weight holder and needle was 3432 dyne, and thus the minimum applied force was 3432 dyne. The force was gradually increased to find the breakdown force. All the results of the scratch tests are shown in Figure 3.1.11, and the scratch test images taken by the digital microscope are given in Figure 3.1.12. The sample H100 could not sustain minimum force applied by the scratch tester. When the mixture of the two precursors was used, the coating was stronger as the H/A ratio decreased.

Table 3.1.4. Scratch test results for each sample.

Sample	Annealing temperature (°C)	Applied Force (AF) (dyne)	Sliding speed (mm/s)	Needle tip diameter (mm)
H100	250	3432	37	0.5
H/A=3/1	250	9316	37	0.5
H/A=1/1	250	13239	37	0.5
H/A=1/3	250	20104	37	0.5
A100	250	25007	37	0.5

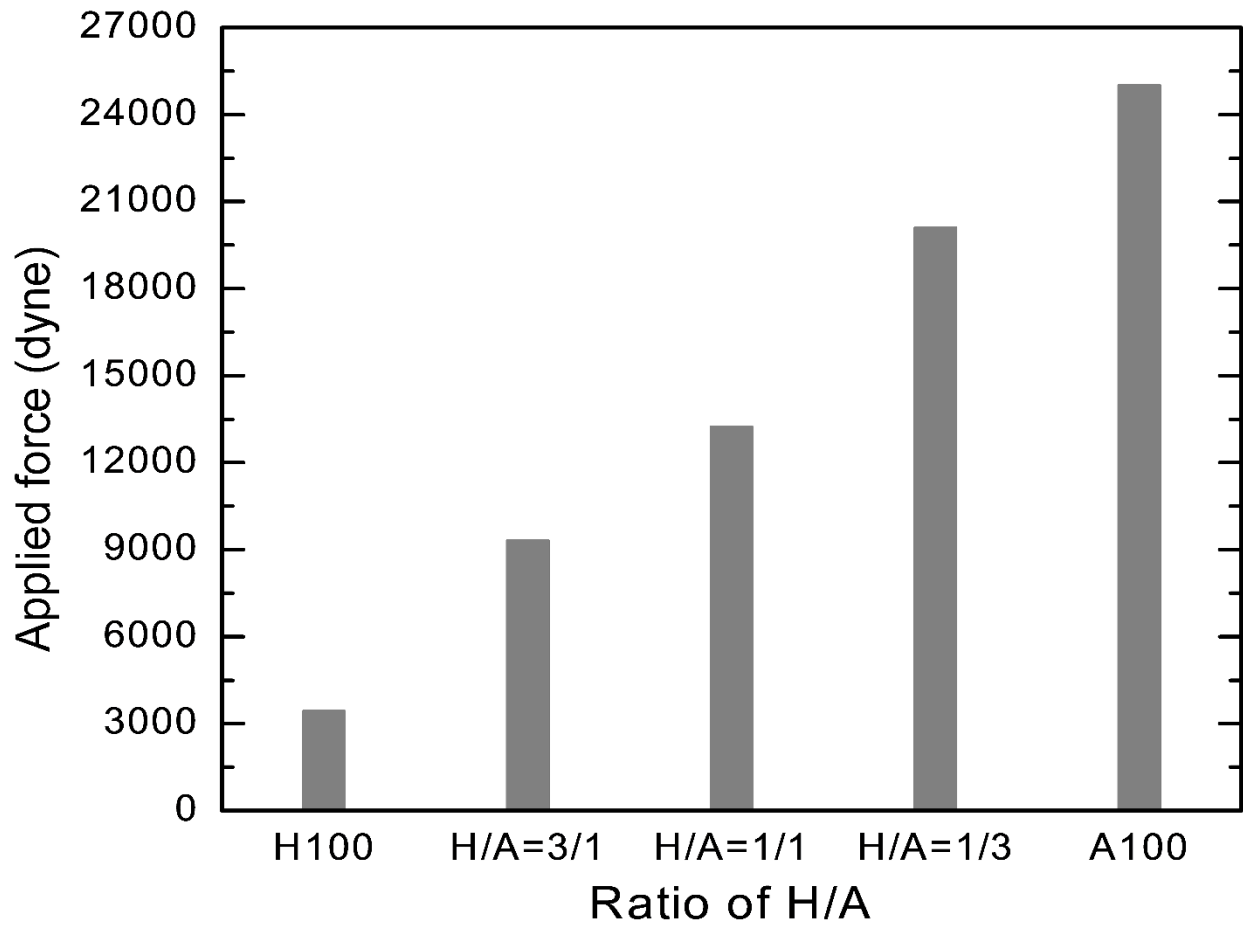


Figure 3.1.11. Breakdown forces of the samples obtained by the scratch tests.

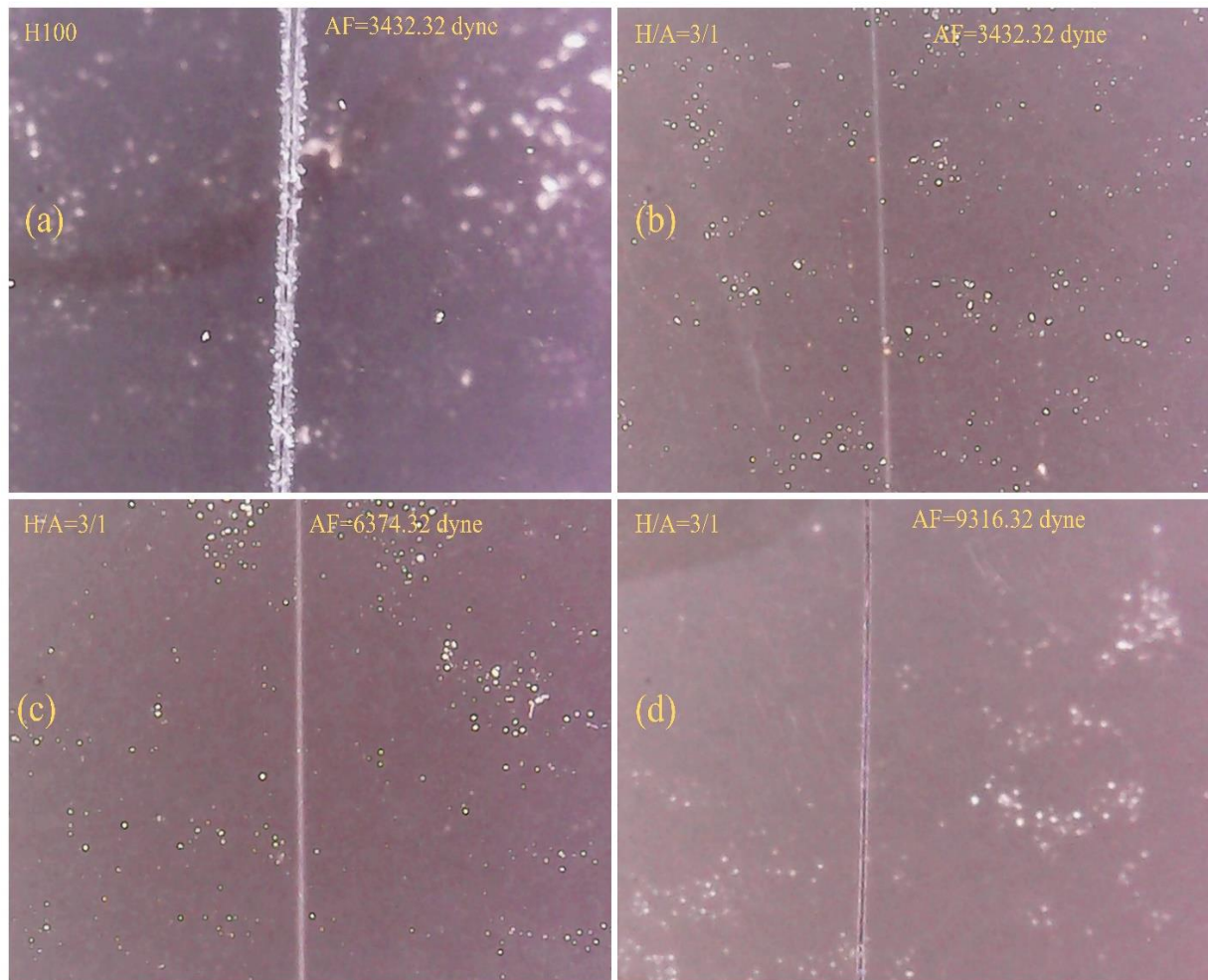


Figure 3.1.12. Microscope images of the selected samples.

3.4. Conclusions

The plasma polymerizations of HMDSO and APTES at different ratios were carried out by the atmospheric pressure plasma jet in order to get a robust and stable hydrophobic surface layer on the glass surface. The HMDSO was used to promote hydrophobicity and the APTES to promote robustness and durability owing to the presence of amines capable of promoting the adhesion of the coating layer. In terms of hydrophobicity and robustness of the coating, the applied voltage of 7 kV, treatment time of 60 s, and the H/A ratio of 3/1 were chosen as optimal condition. The WCA

of 143° and reasonable mechanical strength were obtained under this condition. The deposition of the polymer thin film on the glass surface was evidenced by the SEM and AFM images. The UV–VIS transmission study revealed that there was no significant transmittance loss in the visible region for the sample with H/A ratio of 3/1. Consequently, the nonthermal atmospheric-pressure plasma jet could be a good candidate for producing reliable hydrophobic surface.

3.5. References

- [1] Vogelsang A, Ohl A, Foest R, et al. Hydrophobic coatings deposited with an atmospheric pressure microplasma jet. *J. Phys. D. Appl. Phys.* 2010;43:485201.
- [2] Genzer J, Efimenko K. Recent developments in superhydrophobic surfaces and their relevance to marine fouling: A review. *Biofouling.* 2006;22(5):339–360.
- [3] Ladwig A, Babayan S, Smith M, et al. Atmospheric plasma deposition of glass coatings on aluminum. *Surf. Coatings Technol.* 2007;201:6460–6464.
- [4] Li X-M, Reinhoudt D, Crego-Calama M. What do we need for a superhydrophobic surface? A review on the recent progress in the preparation of superhydrophobic surfaces. *Chem. Soc. Rev.* 2007;36:1350–1368.
- [5] Marchand DJ, Dilworth ZR, Stauffer RJ, et al. Atmospheric rf plasma deposition of superhydrophobic coatings using tetramethylsilane precursor. *Surf. Coatings Technol.* 2013;234:14–20.
- [6] Múgica-Vidal R, Alba-Elías F, Sainz-García E, et al. Atmospheric plasma-polymerization of hydrophobic and wear-resistant coatings on glass substrates. *Surf. Coatings Technol.* 2014;259:374–385.
- [7] Yim JH, Rodriguez-Santiago V, Williams AA, et al. Atmospheric pressure plasma enhanced chemical vapor deposition of hydrophobic coatings using fluorine-based liquid precursors. *Surf. Coatings Technol.* 2013;234:21-32.
- [8] Chattopadhyay S, Huang YF, Jen YJ, et al. Anti-reflecting and photonic nanostructures. *Mater. Sci. Eng. R Reports.* 2010;69(1-3):1-35.
- [9] Farhadi S, Farzaneh M, Kulinich SA. Anti-icing performance of superhydrophobic surfaces. *Appl. Surf. Sci.* 2011;257:6264–6269.

- [10] Raut HK, Ganesh VA, Nair AS, et al. Anti-reflective coatings: A critical, in-depth review. *Energy Environ. Sci.* 2011;4:3779-3804.
- [11] Xue C-H, Jia S-T, Zhang J, et al. Preparation of superhydrophobic surfaces on cotton textiles. *Sci. Technol. Adv. Mater.* 2008;9:035008.
- [12] Zhang X, Shi F, Niu J, et al. Superhydrophobic surfaces: from structural control to functional application. *J. Mater. Chem.* 2008;18:621-633.
- [13] Jafari R, Farzaneh M. Fabrication of superhydrophobic nanostructured surface on aluminum alloy. *Appl. Phys. A Mater. Sci. Process.* 2011;102:195-199.
- [14] Jafari R, Menini R, Farzaneh M. Superhydrophobic and icephobic surfaces prepared by RF-sputtered polytetrafluoroethylene coatings. *Appl. Surf. Sci.* 2010;257:1540-1543.
- [15] Roach P, Shirtcliffe NJ, Newton MI. Progress in superhydrophobic surface development. *Soft Matter.* 2008;4:224-240.
- [16] Safaee A, Sarkar DK, Farzaneh M. Superhydrophobic properties of silver-coated films on copper surface by galvanic exchange reaction. *Appl. Surf. Sci.* 2008;254:2493-2498.
- [17] Saleema N, Farzaneh M. Thermal effect on superhydrophobic performance of stearic acid modified ZnO nanotowers. *Appl. Surf. Sci.* 2008;254:2690-2695.
- [18] Mukhopadhyay SM, Joshi P, Datta S, et al. Plasma assisted surface coating of porous solids. *Appl. Surf. Sci.* 2002;201:219-226.
- [19] Zhang J, Van Ooij W, France P, et al. Investigation of deposition rate and structure of pulse DC plasma polymers. *Thin Solid Films.* 2001;390:123-129.
- [20] Zhang F, Sautter K, Larsen AM, et al. Chemical vapor deposition of three aminosilanes on silicon dioxide: Surface characterization, stability, effects of silane concentration, and cyanine dye adsorption. *Langmuir.* 2010;26:14648-14654.
- [21] Masuko M, Miyamoto H, Suzuki A. Shear strength and durability of self assembled monolayer. 2007 Proc. ASME/STLE Int. Jt. Tribol. Conf. IJTC 2007. 2007 (48108):97-99.
- [22] Kilpi L, Ylivaara OMEOME, Vaajoki A, et al. Microscratch testing method for systematic evaluation of the adhesion of atomic layer deposited thin films on silicon. *J. Vac. Sci. Technol. A Vacuum, Surfaces, Film.* 2016;34:01A124.
- [23] Trinh QH, Lee SB, Mok YS. Hydrophobic Coating of Silicate Phosphor Powder Using Atmospheric Pressure Dielectric Barrier Discharge Plasma. *Am. Inst. Chem. Eng.* 2014;60:829-838.

- [24] Borges JN, Belmonte T, Guillot J, et al. Functionalization of copper surfaces by plasma treatments to improve adhesion of epoxy resins. *Plasma Process. Polym.* 2009;6:S490-S495
- [25] Gubala V, Gandhiraman RP, Volcke C, et al. Functionalization of cycloolefin polymer surfaces by plasma-enhanced chemical vapour deposition: comprehensive characterization and analysis of the contact surface and the bulk of aminosiloxane coatings. *Analyst.* 2010;135(6):1375-81.
- [26] Juda W. Preparation of Ion Exchange Membranes. *J. Appl. Polym. Sci.* 1953;5193:875–884.
- [27] Volcke C, Gandhiraman RP, Gubala V, et al. Plasma functionalization of AFM tips for measurement of chemical interactions. *J. Colloid Interface Sci.* 2010;348:322–328.
- [28] Volcke C, Gandhiraman RP, Gubala V, et al. Reactive amine surfaces for biosensor applications, prepared by plasma-enhanced chemical vapour modification of polyolefin materials. *Biosens. Bioelectron.* 2010;25:1875–1880.
- [29] Howarter JA, Youngblood JP. Surface modification of polymers with 3-aminopropyltriethoxysilane as a general pretreatment for controlled wettability. *Macromolecules.* 2007;40:1128–1132.
- [30] Liu Y, Li Y, Li XM, et al. Kinetics of (3-aminopropyl)triethoxysilane (APTES) silanization of superparamagnetic iron oxide nanoparticles. *Langmuir.* 2013;29:15275–15282.
- [31] Loch CL, Ahn D, Chen C, et al. Sum frequency generation studies at poly(ethylene terephthalate)/silane interfaces: hydrogen bond formation and molecular conformation determination. *Langmuir.* 2004;20:5467–5473.
- [32] Fanelli F, Lovascio S, D'Agostino R, et al. Ar/HMDSO/O₂ fed atmospheric pressure DBDs: Thin film deposition and GC-MS investigation of by-products. *Plasma Process. Polym.* 2010;7:535–543.
- [33] Alba-Elías F, Ordieres-Meré J, González-Marcos A. Deposition of thin-films on EPDM substrate with a plasma-polymerized coating. *Surf. Coatings Technol.* 2011;206:234–242.
- [34] Schäfer J, Foest R, Quade A, et al. Carbon-free SiO_x films deposited from octamethylcyclotetrasiloxane (OMCTS) by an atmospheric pressure plasma jet (APPJ). *Eur. Phys. J. D.* 2009;54:211–217.
- [35] Rombaldoni F, Mossotti R, Montarsolo A, et al. Thin film deposition by PECVD using HMDSO-O₂-Ar gas mixture on knitted wool fabrics in order to improve pilling resistance.

- Fibers Polym. 2008;9:566–573.
- [36] Gueye M, Gries T, Noël C, et al. Interaction of (3-Aminopropyl)triethoxysilane with Pulsed Ar–O₂ Afterglow: Application to Nanoparticles Synthesis. *Plasma Chem. Plasma Process.* 2016;36:1031–1050.
- [37] Finot E, Roualdes S, Kirchner M, et al. Surface investigation of plasma HMDSO membranes post-treated by CF₄/Ar plasma. *Appl. Surf. Sci.* 2002;187:326–338.
- [38] Zanini S, Massini P, Mietta M, et al. Plasma treatments of PET meshes for fuel-water separation applications. *J. Colloid Interface Sci.* 2008;322:566–571.
- [39] Li Y, Zhang J, Zhu S, et al. Biomimetic surfaces for high-performance optics. *Adv. Mater.* 2009;21:4731–4734.

CHAPTER-4

Improvement of mechanical strength of hydrophobic coating on glass surfaces by an atmospheric pressure plasma jet

Highlights

- Robust coating on the glass by APPJ conjugated with two precursors
- Coating strength depended on the flow rate, voltage, time and TMS/APTES ratio.
- The coating exhibited good durability, mechanical strength and thermal stability.
- Coatings show uniform thickness along with excellent visibility

4.1. Introduction

Making hydrophobic surface of various materials by nonthermal plasma (NTP) treatment at atmospheric pressure has been a warm research topic in recent years [1-7]. Researchers found the idea to make hydrophobic surface from nature [8-10] to use it for various purposes such as self-cleaning windows, ultra-dry surface applications, self-cleaning of antennas, anti-icing, outdoor textiles, protection of circuits and grids, medical devices and other optical apparatuses [11-15]. In order to obtain hydrophobic characteristics the surface requires nano-scale and micro-scale roughness which can be done by applying low surface energy coating. Basically, the surface roughness and the surface chemistry both affect the hydrophobicity [16]. The hydrophobic coating can be done by plasma treatment, by deep coating or by spraying low surface energy materials on the surface. The surface having water contact angle (WCA) $< 90^\circ$ is known as hydrophilic surface but having $WCA \geq 90^\circ$ is known as hydrophobic surface. On the other hand, surface having $WCA > 150^\circ$ and sliding angle (SA) $\leq 10^\circ$ is called super-hydrophobic surface due to its excellent self-cleaning ability. Generally, WCA and SA indicate the performance of the surface how much it will be effective in self-cleaning function.

The major drawback of the coatings is its poor mechanical abrasion which extinguishes the self-cleaning function due to the damage of roughness and coating layer. As a result, for this experiment two different precursors have been selected to investigate the mechanical strength of the coating. Tetramethylsilane (TMS, $Si(CH_3)_4$) used to promote hydrophobicity in this work is an organosilicon compound precursor having the formula $Si(CH_3)_4$. Though TMS is a good promoter of hydrophobicity, due to its poor adhesion to metal or inorganic material, the coating does not survive for long time. To overcome this problem an additive precursor called (3-Aminopropyl)triethoxysilane (APTES, $H_2N(CH_2)_3Si(OC_2H_5)_3$) is also used together with TMS to

make robust coating on the glass surface. APTES is an aminosilane basically used in the process of silanization as well as the functionalization of surfaces with alkoxy silane molecules. In recent times, APTES is highly recommended to use for surface coating due to its covalent attaching of organic films to metal oxides, silica (SiO_2) [16] and titania (TiO_2). Masuko et al. [17] studied the shear strength and durability of self-assembled monolayer (SAM) and the tribology performance with different numbers of siloxane bonds on smooth silicon substrates. They showed that increasing the number of siloxane bonds with SAMs actually allows the stable low friction and greater durability. Therefore, APTES having these advantages is selected as a promoter for robust coating to improve the wear resistance of the surface although it is hydrophilic in character.

Nowadays, NTPs are very popular to create a thin film polymer layer onto different surfaces such as silicon, glass, wood, and fabric. The pioneer advantage of the NTP is that polymerization or deposition for the coating can be easily controlled by controlling electric power and gas flow rate. Topala et al. [18] used DBD plasma to deposit thin film onto glass and silicon substrates to get stable hydrophobic surface. With these background knowledges, non-thermal plasma jet operating at atmospheric pressure has been selected for this work. One of the key parameters explored was the ratio of TMS to APTES.

4.2. Experimental

Figure 4.1.1 shows the schematic figure of the experimental setup and custom-built scratch tester and Figure 4.1.2 shows the discharge image of the plasma jet. The plasma jet was composed of a glass tube having a coaxially inserted stainless-steel rod with a sharp tip acting as the high voltage (HV) electrode. The orifice of the glass tube from which the plasma jet was discharged had the inner and outer diameters of 5.0 and 8.0 mm, respectively. The HV electrode was

connected to an AC power source purchased from Korea Switching Co., which could deliver maximum 7.5 kV at an operating frequency of 11.5 kHz. The distance between the tip of the HV electrode and the end of the tube and the gap from the end of the tube to the substrate were kept constant at 75 and 2 mm, respectively. Argon gas (99.99%) was used as a main carrier gas at a rate

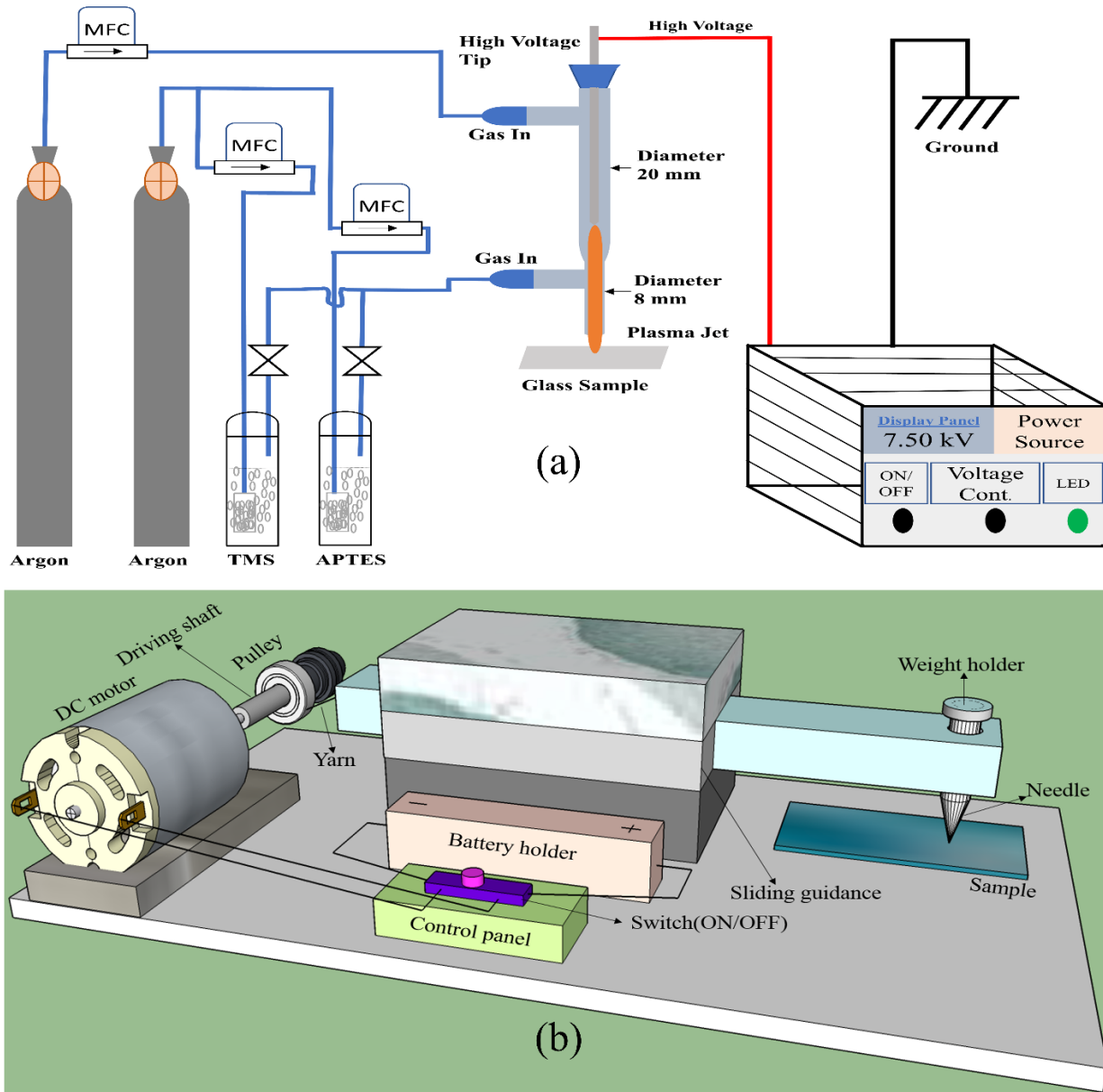


Figure 4.1.1. The schematic figure of the experimental setup (a) and custom-built scratch tester (b).

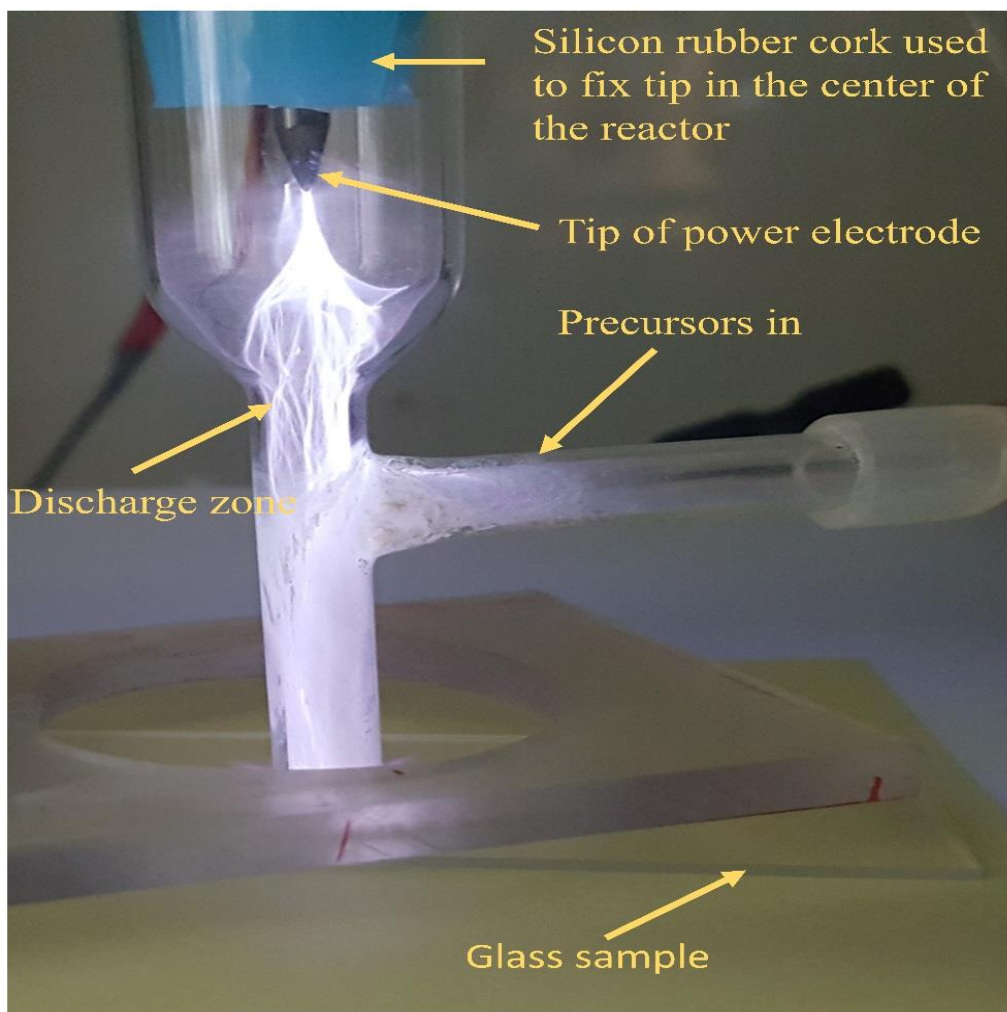


Figure 4.1.2. Discharge photograph image of the plasma jet.

of $1600 \text{ cm}^3 \text{ min}^{-1}$ (sccm). TMS (Sigma-Aldrich Korea Co., Ltd) was used to promote hydrophobicity, and APTES (Sigma-Aldrich Korea Co., Ltd) was used to promote the robustness of the coating. The precursors were delivered to the jet by bubbling liquid TMS and APTES (at 20 and 121 °C, respectively) contained in pyrex flasks using Ar gas. All Ar flows were precisely controlled by mass flow controllers (MFCs). The TMS/APTES ratio was varied from 3.0 to 6.0 to investigate its effect on the thin film obtained by the plasma polymerization. The TMS concentration was changed by the feed gas from 4304 ppm (parts per million, volumetric) to

8450 ppm, while APTES concentration was kept constant at 1408 ppm. The main carrier gas and precursor mixture were separately fed into the jet. The substrate for the coating was soda-lime glass with a dimension of 75 mm × 27 mm × 1.2 mm. For simplicity, the substrates were set to stand still during coating. The resulting coated area was estimated to be about 20 mm². It is important to know the WCA of the coated surface for understanding the character of the coated surface polymer. The WCA measurements were carried out on a goniometer (Phonix 300, Surface & Electro Optics Co., Ltd., Korea) using sessile drop technique by dropping about 10 μL of distilled water. To see the surface nanostructures of the coating, atomic force microscopy (AFM, Nano Xpert II, EM4SYS, USA) was performed. The surface morphology was observed by scanning electron microscopy (SEM, JSM-6700F, JEOL, Japan) at an operating voltage of 15 kV. The coating surface chemistry was analyzed using an X-ray photoelectron spectroscopy (XPS). A Fourier transform infrared spectroscopy (FTIR, FTIR-7600, Lambda Scientific, Australia) was used to investigate the composition of the effluent from the plasma jet and the deposited thin films. Measurement of mechanical strength of the coating was carried out using a custom-built scratch tester and the wear tracks were observed by an optical microscope (2MP 1000 × 8 LED USB Digital Microscope Zoom Camera, A4Tech, Taiwan). Many researchers used scratch test to assess the coating adhesion and robustness [19-26]. A new scratch test methodology was recently developed to use in various modes of scratch test to quantify scratch resistance of polymeric coatings [27]. Richard et al. [28] used combination of scratch test and acoustic microscopy imaging for the study of coating adhesion. Scratch test is a simple and rapid method for characterizing the coatings. Obtained results by scratch test are influenced by various factor such as coating thickness, interfacial bond strength, mechanical properties of substrate, test condition such as load, scratch speed, and indenter tip radius [29]. Scratch testing is usually performed by moving sharp

tip on the coated surface with either constant or progressively increasing load to create a scratch [30]. The scratch tester used in this work is shown in Figure 4.1.1(b). Its main parts include a dc motor, a needle holder, a needle, a sliding guidance, and a control panel. An iron needle having a tip with a diameter of 0.5 mm was used. Yarn was used to connect the driving shaft of the motor to the needle holder. The needle holder was guided by the sliding guidance so that it can move horizontally back and forth. The moving speed of the needle was set to 37 mm/s. A sample for testing was put under the needle and fixed by using double-sided tape. For each measurement, the tip of the needle was cleaned with acetone and tissue wiper.

4.3. Results and discussion

4.3.1. Hydrophobic treatment of glass and water contact angle measurement

The hydrophobic treatment by the plasma polymerization process depended on a number of parameters such as applied voltage, treatment time, the TMS/APTES ratio and the gas flow rate. At first, the effect of the treatment time was examined from 30 s to 420 s at a TMS/APTES ratio of 4.8 and an applied voltage of 7.5 kV., and then the effect of the applied voltage, TMS/APTES ratio and the gas flow rate on the coating was examined one by one with the other parameters kept constant. Figure 4.1.3 shows the dependence of WCA on the treatment time, the applied voltage, the TMS/APTES ratio and the feed gas flow rate. As seen in Figure 4.1.3(a), the WCA significantly increased from 87° to 139° with increasing the treatment time up to 300 s and seemed to level off thereafter. The improvement of the coating in terms of WCA is related to the surface coverage which increased with increasing the treatment time.

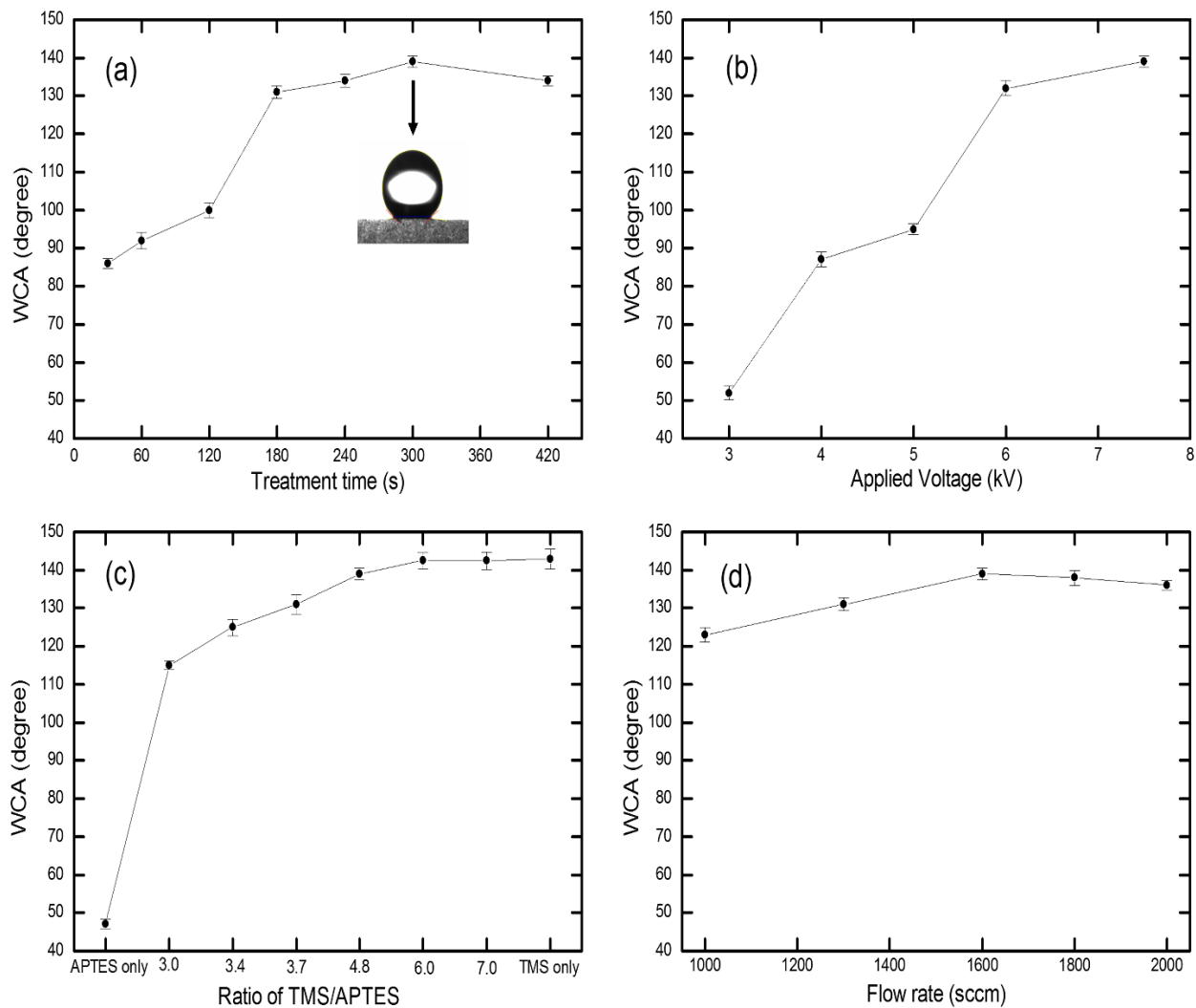


Figure 4.1.3. Dependence of WCA on (a) treatment time, (b) applied voltage, (c) the TMS/APTES ratio and (d) the flow rate of the carrier gas.

Second step was to find out appropriate applied voltage and hence the TMS/APTES ratio and treatment time were kept constant at 4.8 and 300 s, respectively. As shown in Figure 4.1.3(b), a similar increasing trend in the WCA was observed. The higher the applied voltage, the more intense the plasma was, leading to the enhancement in the deposition rate and the formation of particulates in the plasma gas phase, called dusty plasma. The high surface roughness and therefore the high WCA of the coating is strongly related to the deposition of the formed particulates on the

substrate. At the applied voltage of 7.5 kV, the WCA was observed to be ca. 139°. The surface roughness of the obtained coatings will be discussed below.

After having an idea of treatment time and applied voltage the TMS/APTES ratio was varied while the treatment time and applied voltage were kept constant at 300 s and 7.5 kV, respectively. Figure 4.1.3(c) shows the dependence of WCA on the TMS/APTES ratio. The WCA values of the coatings formed from the single precursor of APTES and TMS are also added for the purpose of comparison. It is natural that the WCA should increase with increasing the TMS/APTES ratio due to the hydrophobic character of TMS. At the TMS/APTES ratio of 6, the WCA shows the similar values achieved by the TMS-alone coating. Further, increase the ratio only increase the thickness but WCA angle remain same like as the TMS/APTES ratio of 6. Meanwhile, the low WCA of the APTES-alone coating clearly showed the hydrophilic nature of APTES.

Finally, we changed the flow rate of the gas to see the effect of the WCA while treatment time, applied voltage, the TMS/APTES ratio were kept constant at 300 s, 7.5 kV, and 4.8 respectively. Figure 4.1.3(d) shows the result of the flow rate change from 1000 sccm (Standard Cubic Centimeters per Minute) to 1600 sccm. It was observed that the plasma was getting more intense, leading to an increased WCA from 123° to 139°. But further increases of the feed gas flow rate to 2000 sccm slightly decreased the WCA to 136°, and hence 1600 sccm was chosen for the optimal gas flow rate.

Figure 4.1.4 displays the photographic images of the water droplet on various substrates in the coated state. Here, top view was added to see the surface of the coating and side view to see the WCA.

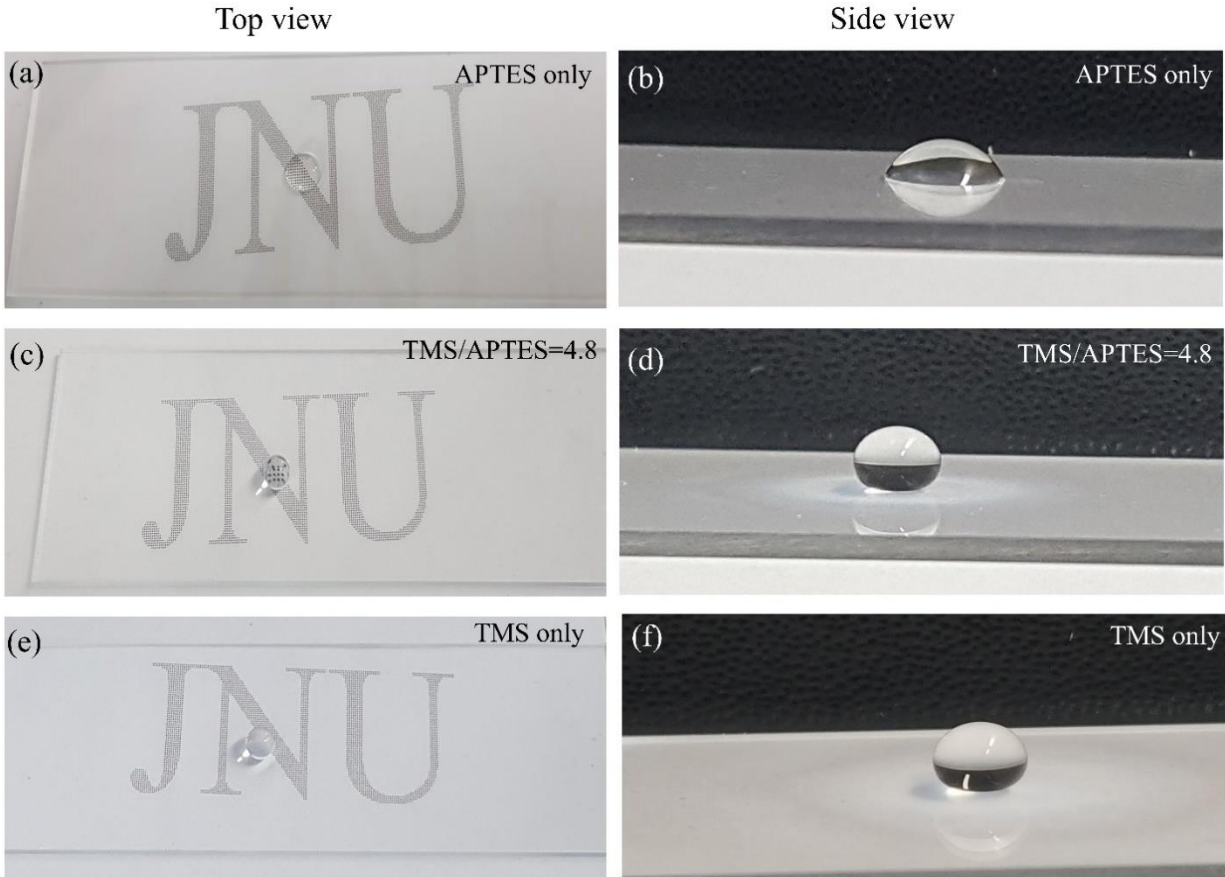


Figure 4.1.4. Photograph image of the coated surface in the coated state.

4.3.2. Coating stability

For this work, the plasma-treated samples were stored in centrifuge tube at room temperature to check the coating stability under the effect of natural aging and thermal heating. Aging time has a great effect on WCA for the powder substrate coating [31]. For powder substrate coating, WCA can increase by 15° to 40° within 30 days [31]. Figure 4.1.5(a) shows the effect of aging (15 days and 30 days) on WCA, where it can be easily understood that there is negligible aging effect on WCA. In other words, the coating is stable and durable. The thermal stability of

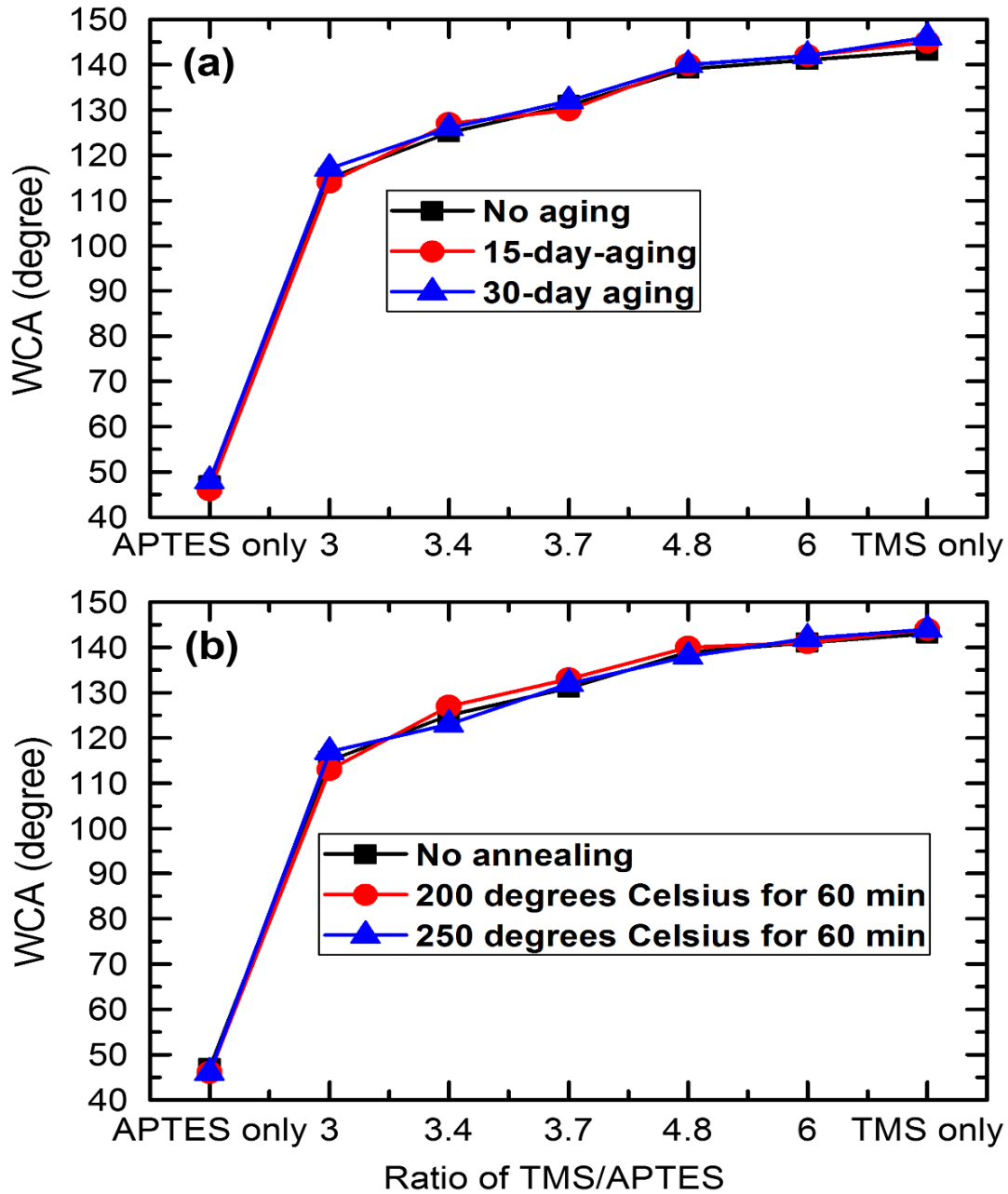


Figure 4.1.5. (a) Effect of aging time and (b) annealing temperature on the coating.

the coating was examined by annealing tests at 200 °C and 250 °C for one hour. In both cases, there was no change in WCA, as shown in Figure. 4.1.5(b).

4.3.3. Coating thickness and surface morphology

The AFM and SEM analyses were performed to examine the effect of TMS/APTES ratio on the surface morphology and surface roughness of the coatings. Figure 4.1.6 shows the AFM results of the coated samples with various TMS/APTES ratios. The corresponding root-mean-squared (RMS) roughness and coating thickness values are listed in Table 4.1.1. As seen, the morphologies of all coatings were similar regardless of the precursor ratio, displaying rough and needle-like surfaces. However, the RMS roughness seemed to increase with increasing the TMS/APTES ratio, which is consistent with the increased WCA. Among the coated samples, the APTES-alone case showed the lowest surface roughness. Meanwhile, the opposite was true for the TMS-alone case. The formation of rough surfaces with nanoscale topographic features results from the generation of particulates through gas-phase condensation reactions. The plasma-induced particulates are then deposited and adhere to a substrate [5]. In plasma, TMS seemed to be more active than APTES to produce more fragments, facilitating the formation of particulates and therefore the high surface roughness.

Table 4.1.1. Thickness and RMS roughness of each sample.

Sample	Thickness (nm)	RMS roughness (nm)
APTES	103	37 ± 5
TMS/APTES = 3	218	64 ± 4
TMS/APTES = 3.4	270	71 ± 7
TMS/APTES = 3.7	300	85 ± 7
TMS/APTES = 4.8	431	108 ± 5
TMS/APTES = 6	480	117 ± 5
TMS	460	120 ± 5

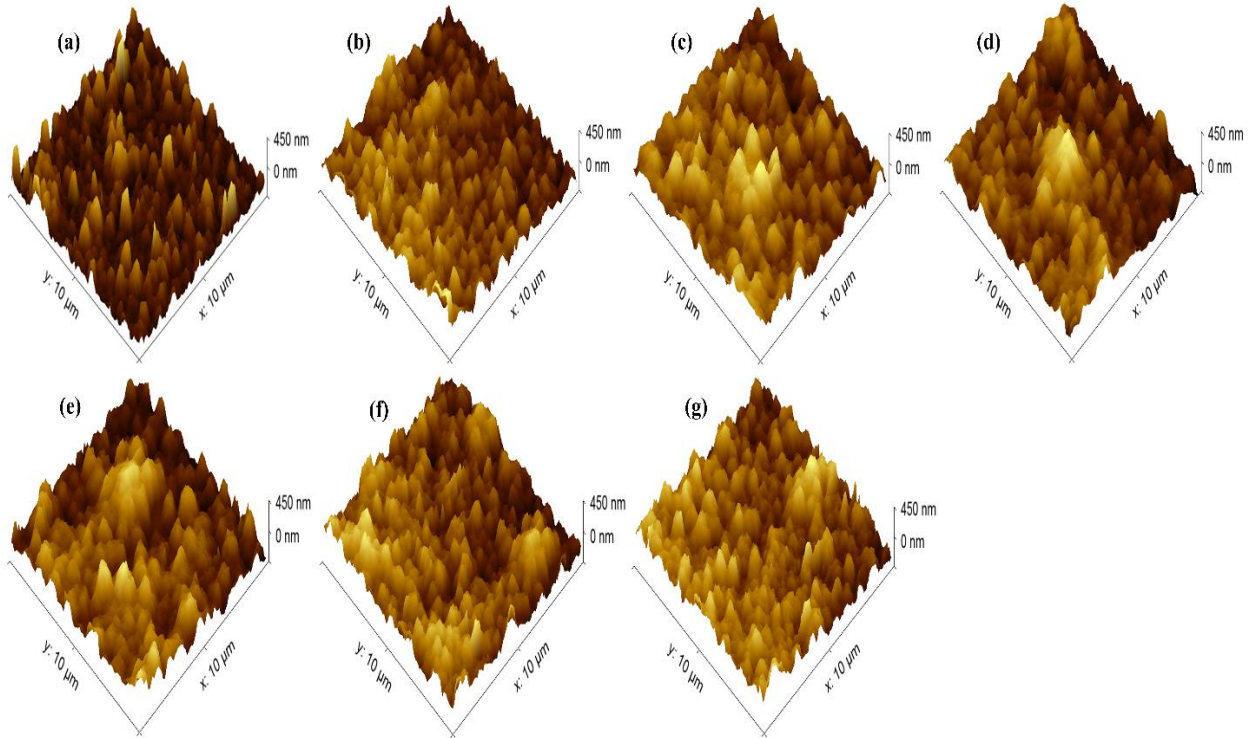


Figure 4.1.6. AFM images of the coated samples. [TM = TMS and AP = APTES, (a) APTES only, (b) TM/AP = 3, (c) TM/AP = 3.4, (d) TM/AP = 3.7, (e) TM/AP = 4.8, (f) TM/AP = 6, and (g) TMS only].

The SEM images of the corresponding samples are shown in Figure 4.1.7. The coatings consist of nanostructures ranging from 70 to 250 nm. It is clear that at high TMS/APTES ratios, the particulates were intensively formed and deposited on the substrates. It is found that the coatings have shown cauliflower morphology in the case of TMS-alone and the TMS/APTES ratio of 6 (Figure 4.1.7 (g) and (f), respectively) but in other cases the nanostructures like circular island with different sizes were formed. In comparison, at low TMS/APTES ratios, the particulates adhered to smooth layers that were mainly formed from APTES.

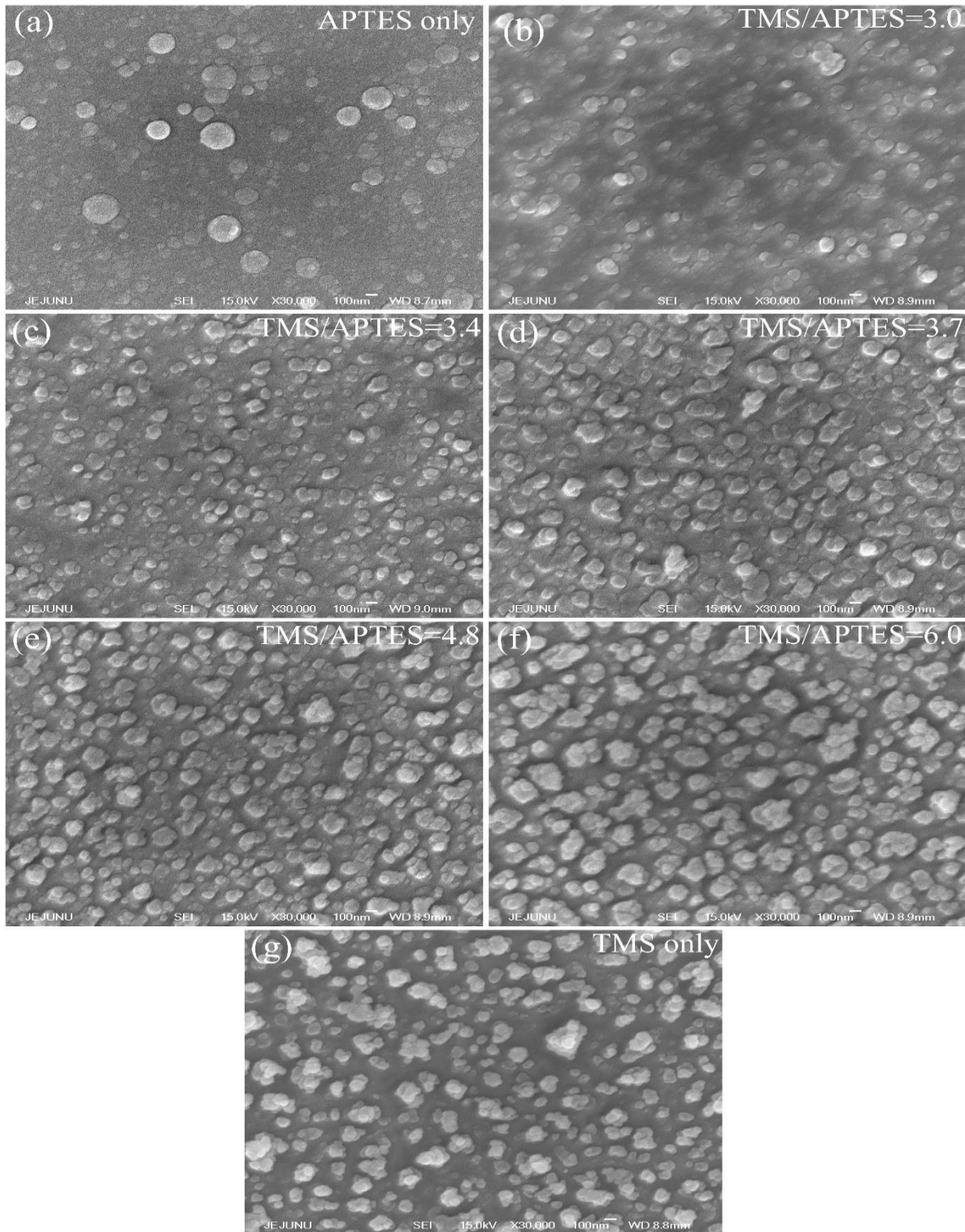


Figure 4.1.7. SEM images of the coated samples. [TM = TMS and AP = APTES, (a) APTES only, (b) TM/AP = 3, (c) TM/AP = 3.4, (d) TM/AP = 3.7, (e) TM/AP = 4.8, (f) TM/AP = 6, and (g) TMS only].

4.3.4. Gas-phase FTIR analysis

4.3.4.1. Gas-phase analysis of the effluent of the Ar/TMS plasma

Figure 4.1.8 shows the FTIR spectra of the Ar/TMS and Ar/APTES mixture without (black) and with (red) plasma ignition. If we look at the figure (Figure 4.1.8 (a) & (b)), the main significant difference is the reduction of IR peak intensities in the case of plasma turned on due to the TMS and APTES decomposition. When the plasma is turned on, the absorption intensities for both TMS and APTES decreased which indicates that these precursors compounds were decomposed by plasma. Figure 4.1.8 (a) presents the infrared spectra for the gas-phase effluent of the Ar/TMS mixture. Strong peaks were observed from 1000 cm^{-1} to 1500 cm^{-1} and from 2800 cm^{-1} to 3300 cm^{-1} , while some other weak peaks appeared at wavenumbers from 1800 cm^{-1} to 2400 cm^{-1} (see the insets). Here, the peaks at 1256 cm^{-1} , 1289 cm^{-1} , 1430 cm^{-1} , 2823 cm^{-1} , and 2965 cm^{-1} are due to TMS [32-34]. The strong deformation of CH_3 symmetric groups are found at 1247 cm^{-1} and 1265 cm^{-1} [34]. A weak SiO peak at 1065 cm^{-1} is found only in Ar/TMS with plasma. CH_3 rock, SiH_2 bend, and Si-H symmetric stretching are observed at $3050\text{--}3100\text{ cm}^{-1}$ only in Ar/TMS without plasma [33-35]. The infrared spectra also detected the very weak peak of CO_2 at 2350 cm^{-1} , Si-H stretching at 2129 cm^{-1} , and deformation of CH_3 symmetric groups at 1863 cm^{-1} and 1947 cm^{-1} [33-35].

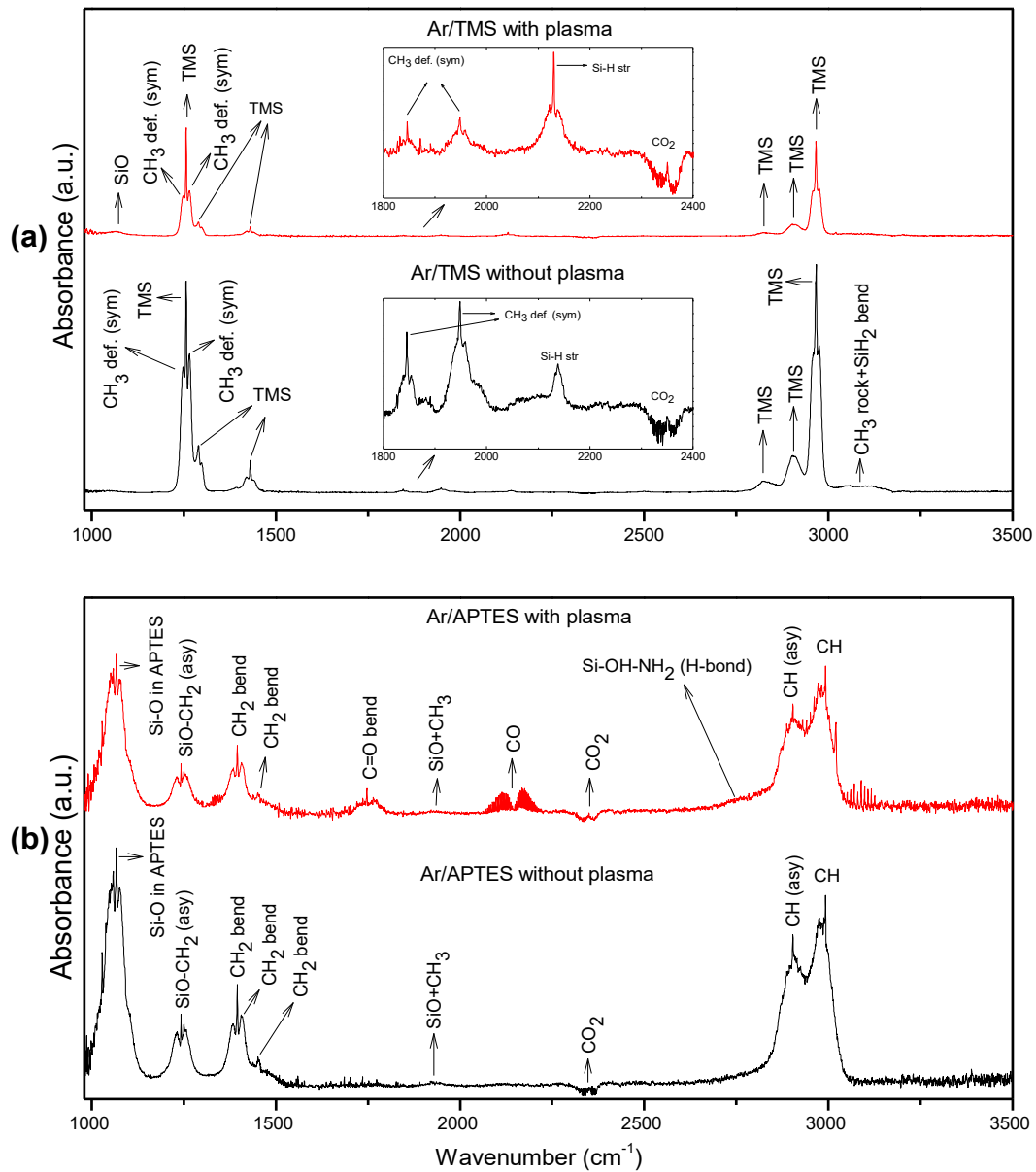


Figure 4.1.8. (a) Gas-phase FTIR spectra of the Ar/TMS without (black) and with (red) plasma and (b) gas-phase FTIR spectra of the Ar/APTES without (black) and with (red) plasma from 1000 to 3500 cm^{-1} .

4.3.4.2. Gas-phase analysis of the effluent of Ar/APTES plasma

The gas-phase FTIR spectra of the Ar/APTES mixture without (black) and with (red) plasma ignition are shown in Figure 4.1.8 (b). A high-intensity peak at 1065 cm^{-1} is assigned to the vibration of Si-O in APTES [35–37]. A strong asymmetric peak at 1242 cm^{-1} is due to the vibration of SiO-CH₂ [35]. Weak peaks at 1451 cm^{-1} and 1475 cm^{-1} are attributed to H-C-H bends, while the strong peak at 1395 cm^{-1} is for the CH₂ bending. The H-C-H bending at 1475 cm^{-1} is only found in Ar/APTES mixture without plasma [36,38,39]. The Strong asymmetric peak at 2903 cm^{-1} and very strong symmetric peak at 2985 cm^{-1} are found for the vibration of CH₂ [35]. Very weak O-H stretch mode of Si-OH-NH₂ group is detected at the frequency of 2762 cm^{-1} , which is only observed in the Ar/APTES mixture with plasma [40]. The infrared spectra also detected C=O bend at 1746 cm^{-1} and CO at 2140 cm^{-1} only in Ar/APTES with plasma case. A weak peak appearing at 1923 cm^{-1} may be ascribed to SiO+CH₃ bend in both with and without plasma [35,37].

To see the effect of gas phase on the hydrophobicity, one more experiment was done using TMS/APTES mixture without plasma discharge, and then the WCA of the glass was measured. It has shown there was no change in hydrophobicity under such a condition.

4.3.4.3. Possible reaction routes and mechanism of APTES for the surface modification

Siloxane-based plasma polymerization with primary amines using a single amino-alkoxysilane precursor is still under investigation and only a few articles discussed about this issue [41–45]. The Plasma-assisted APTES polymerization is described in Figure 4.1.9 [46–48]. The

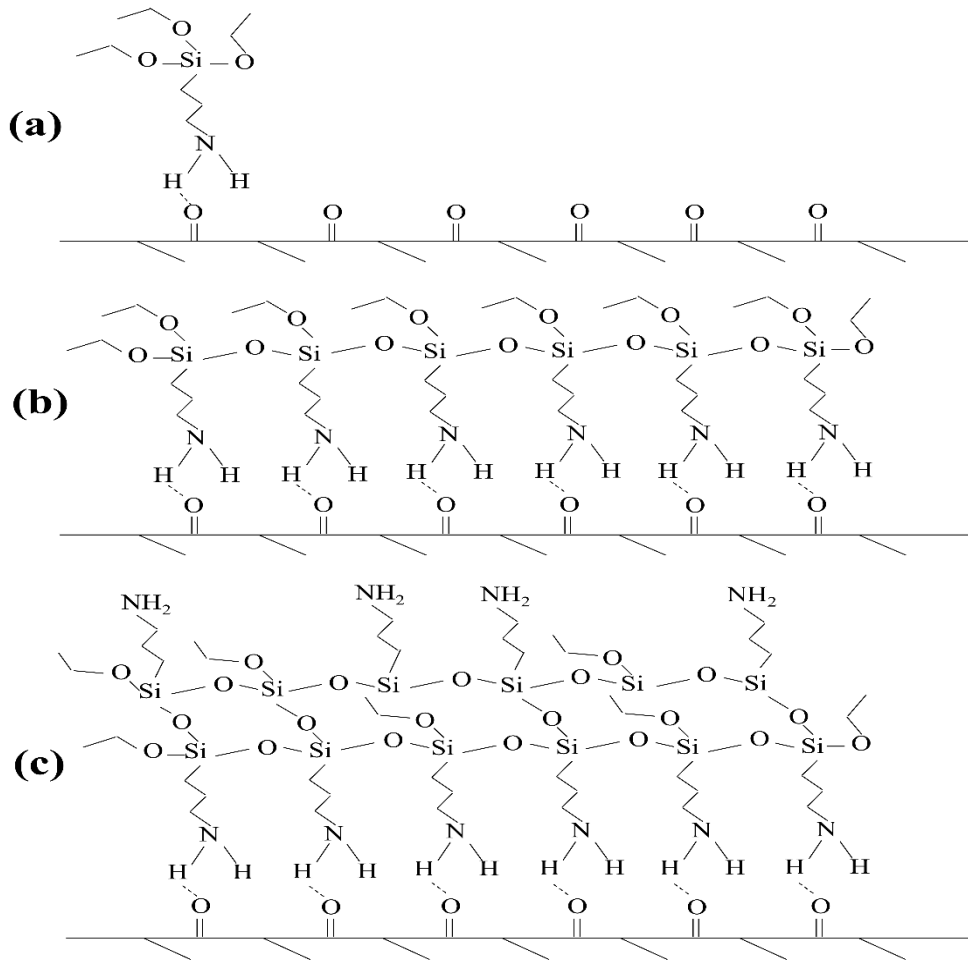


Figure 4.1.9. Possible reaction routes and mechanism of APTES for the surface modification: (a) hydrogen bonding due to initial adsorption, (b) surface attachment, and (c) multilayer formation.

process can be divided into three parts: (a) hydrogen bonding due to initial adsorption, (b) surface attachment, and (c) multilayer formation. The polymer surface by the hydrogen bonding is the 1st step (Figure 4.19(a)) of physical process of APTES [48] where siloxane bond formation by the ethoxy groups with neighbors H-bonded to the surface with free APTES molecules can be seen in Figure 4.1.9(b). From Figure 4.1.9(a) and 4.1.9(b) still there is no sign of donor amine and acceptor groups. This means that some of APTES molecules are not H-bonded to the surface. Basically, the

inter-APTES reactions lead to the formation of siloxane cross-link and it makes a thin layer (Figure 4.1.9(c)) where donor amine and acceptor H-bond both are present.

4.3.5. FTIR analysis of the coating layer

So as to take the FTIR spectra of the coating layer, the coatings were prepared on infrared-transparent KBr discs instead of the glass substrates. Note that strong IR adsorption of glass hinders the infrared analysis of the coating layer. The obtained results are shown in Figure 4.1.10. The

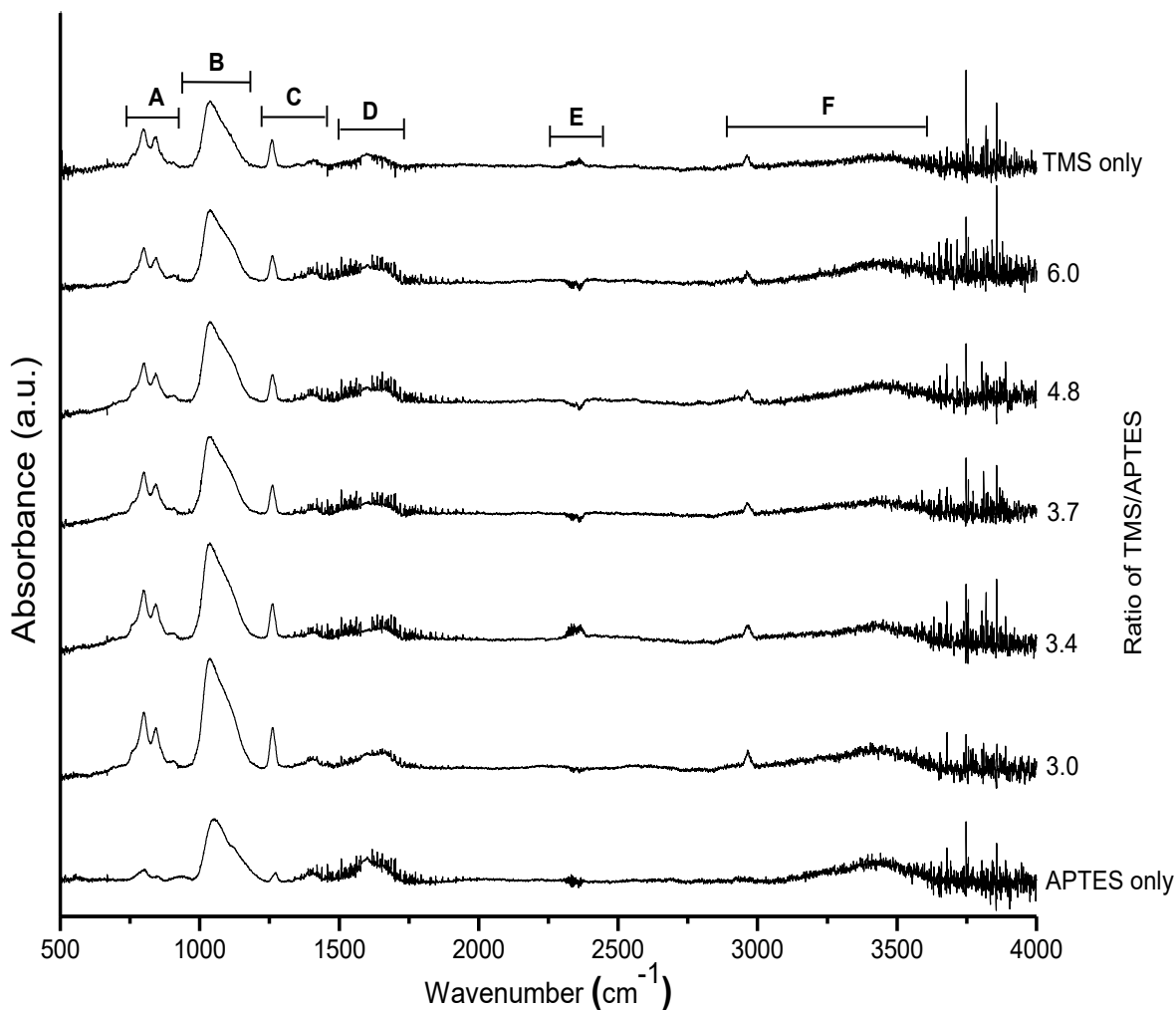


Figure 4.1.10. FTIR spectra of coated samples from 500 to 4000 cm^{-1} .

most intense peaks are seen in the region B in the range of 1010-1240 cm^{-1} . These peaks are due to the Si-O stretching in Si-O-Si [49,50]. In the region A, the Si-C stretching is seen at 800 cm^{-1} [49] and the peaks of Si-O stretching in Si-OH are seen at 830-940 cm^{-1} [49–51]. In the regions C and F, the peaks at 1260 cm^{-1} and 2970 cm^{-1} are related to Si-CH₃ symmetric deformation and Si-CH₂ deformation or Si-CH₃ asymmetric stretching appears at 1410 cm^{-1} [52,53]. The wide Si-OH stretching vibration is seen in the region F [49,54].

4.3.6. XPS analysis

The XPS analysis was carried out to identify the surface chemical composition of the coatings. From the XPS study, it was found that the uncoated soda-lime glass contains silicon (Si), carbon (C), calcium (Ca), nitrogen (N), oxygen (O) and sodium (Na). On the other hand, silicon

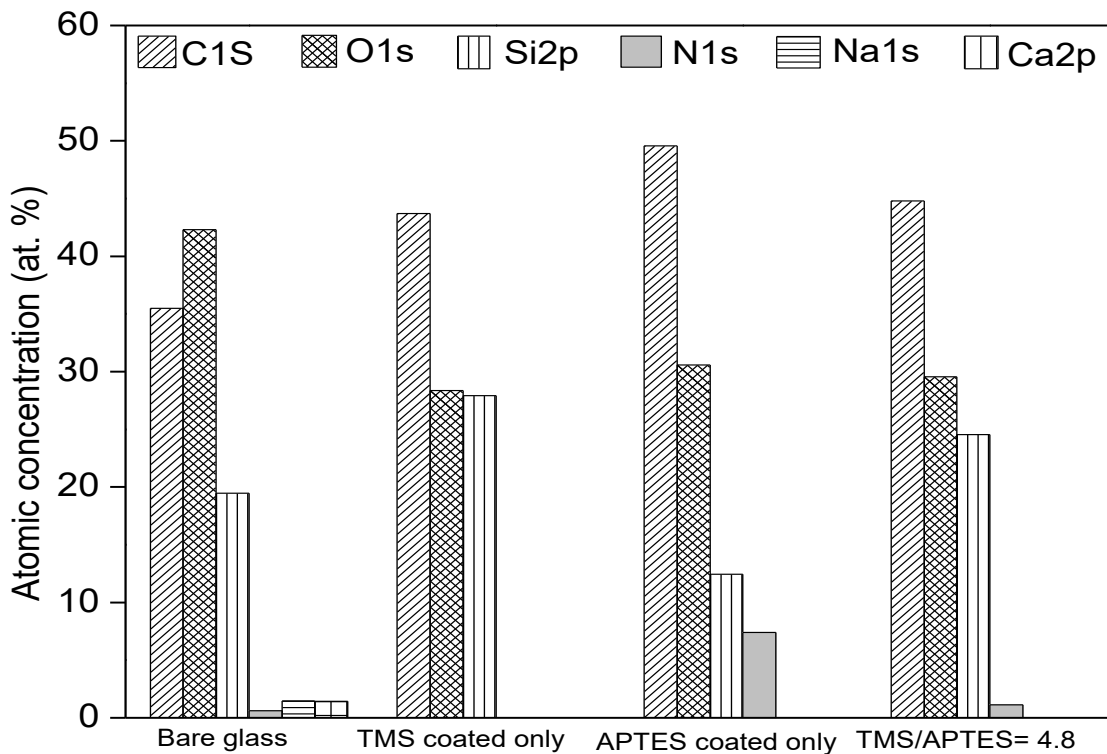


Figure 4.1.11. Elemental composition (%) of sample surfaces.

(Si), carbon (C), nitrogen (N) and oxygen (O) were found in the coated glasses. Figure 4.1.11 shows the concentrations of the elements observed for the bare glass and the ones coated with only TMS, only APTES and TMS/APTES mixture of a ratio of 4.8. The plasma-treated glass with TMS alone did not contain any nitrogen in the coating layer. 35% carbon in the bare glass is probably due to the presence of adventitious carbon on the sample's surface [3]. The presence of carbon of the coated glasses was provided by both adventitious and precursors.

The deconvolution of C1s spectra is shown in Figure 4.1.12 and the peak positions of C1s with the corresponding functional groups are seen in Table 4.1.2. H-C or C-C peak was found at ~284.7 eV from all the samples [3,55]. The peak at around 286 eV also appeared from all the samples due to the C-O bond. The C-N group appeared from the APTES and TMS/APTES coated samples (Figures 4.1.12(c) and 4.1.12(d)) [3,55]. The peak at ~287.5 eV was due to C=O in the

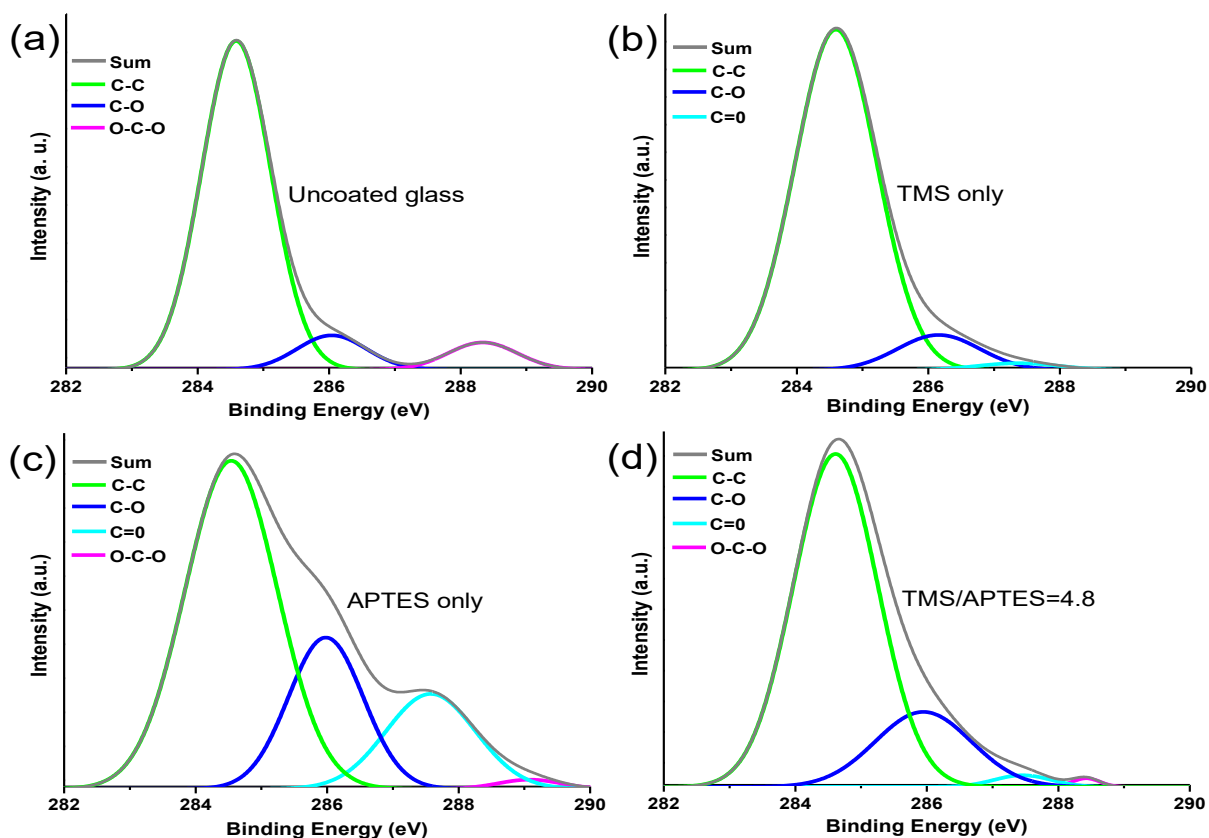


Figure 4.1.12. Deconvolution of C1s spectra (282–290 eV) of the coated samples.

coated samples (Figures 4.1.12(b), 4.1.12(c), and 4.1.12(d)) and peak at ~288.7 eV was found due to O-C-O in the uncoated sample and the ones coated with only APTES and TMS/APTES mixture [3,55].

Table 4.1.2. Deconvolution of C1s spectra along with binding energies and functional groups.

Functional groups	Peak Position (eV)	References
C-C, C-H	~284.7	[3,55]
C-O, C-N	~286	[3,55]
C=O	~287.5	[3,55]
O-C-O	~288.7	[3,55]

4.3.7. UV-Vis transmission spectra result

Figure 4.1.13 shows the UV-Vis transmission spectra of the bare glass and the ones coated with APTES, TMS, and their mixture at various ratios. Transmittance and hydrophobicity both

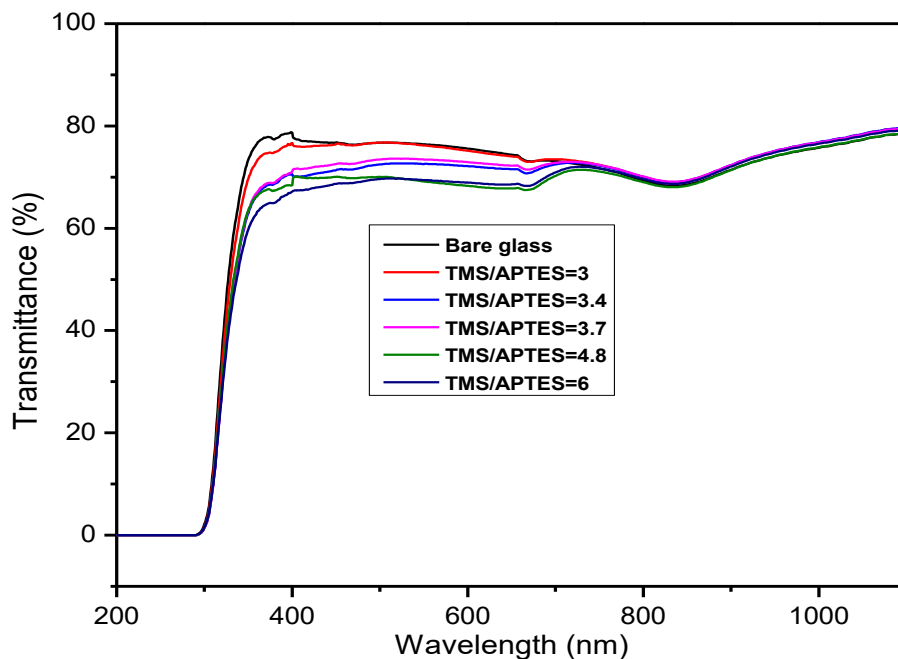


Figure 4.1.13. UV-vis transmission of the coated samples.

depend on the thickness and roughness of the coating. In order to increase the hydrophobic property, thickness and roughness need to be increased, however, the visibility has to be sacrificed [56]. The transparency of the coated glasses in the visible region (from 390 to 700 nm) decreased with increasing the TMS/APTES ratio. Bare glass exhibited around 80% transmittance in the visible regions, while the plasma-treated glasses at different TMS/APTES ratios showed transmittance from 80 to 65%.

4.3.8. Scratch test

For finding the same coating thickness, the deposition rate of each sample was calculated. Four samples with different treatment time for TMS/APTES=4.8 sample was generated. After that, the thickness of each sample was measured and plotted in Microsoft Excel and found the slope which was the deposition rate. By doing this, the deposition rate was calculated for each sample.

Table 4.1.3. Scratch test results (breakdown force).

Sample	Annealing temperature (°C)	Coating thickness (nm)	Treatment time (min)	Deposition rate* (nm/min)	Applied force (dyne)
APTES only	250	400	16.5	25.9	16671
TMS/APTES=3	250	400	8.3	56.2	14709
TMS/APTES=3.4	250	400	7.1	64.5	10767
TMS/APTES=3.7	250	400	6.1	85.5	9316
TMS/APTES=4.8	250	400	4.2	67.8	7354
TMS/APTES=6	250	400	4.1	86.2	3432
TMS only	250	400	6.4	64.5	3432

*This is the slope value of linear fitting.

After analyzing all the sample thickness, 400 nm thickness was considered for the scratch test. So each sample should have 400 nm thickness for scratch test. Scratch tests were conducted after annealing the samples at 250° C for 1 h. The minimum force applied to the needle tip was 3430 dyne, which was applied to all the samples. For the samples that could sustain the 3430 dyne force, the force was gradually increased to find the breakdown force. The experimental conditions are summarized in Table 4.1.3. Figure 4.1.14 shows the results of the scratch tests, and Figure 4.1.15 shows the images of the scratch tests. As can be seen, the presence of APTES as a precursor greatly enhanced the scratch resistance of the coating layer, compared to the coating with only TMS. For example, the TMS coating was totally destroyed by the needle at the applied force of 3432 dyne. In comparison, at the same force, the TMS/APTES coating was only slightly scratched by the needle.

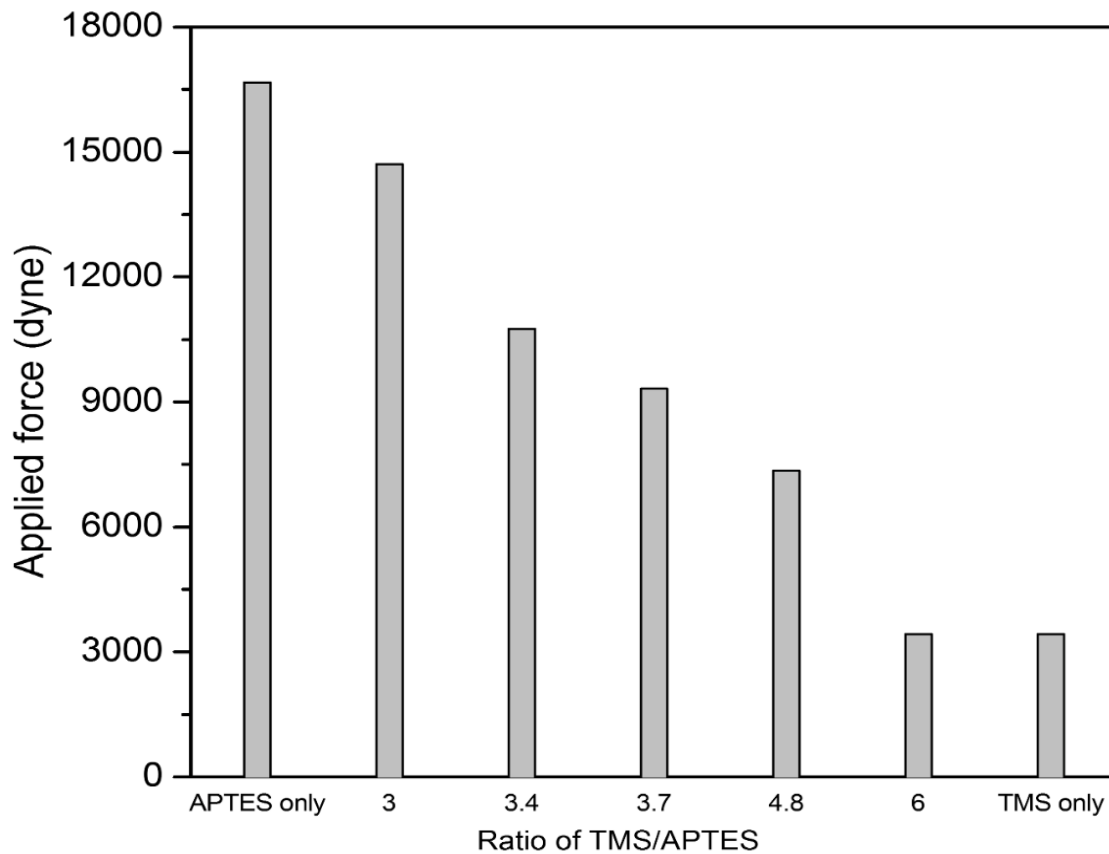


Figure 4.1.14. Scratch test results sustained by the samples.

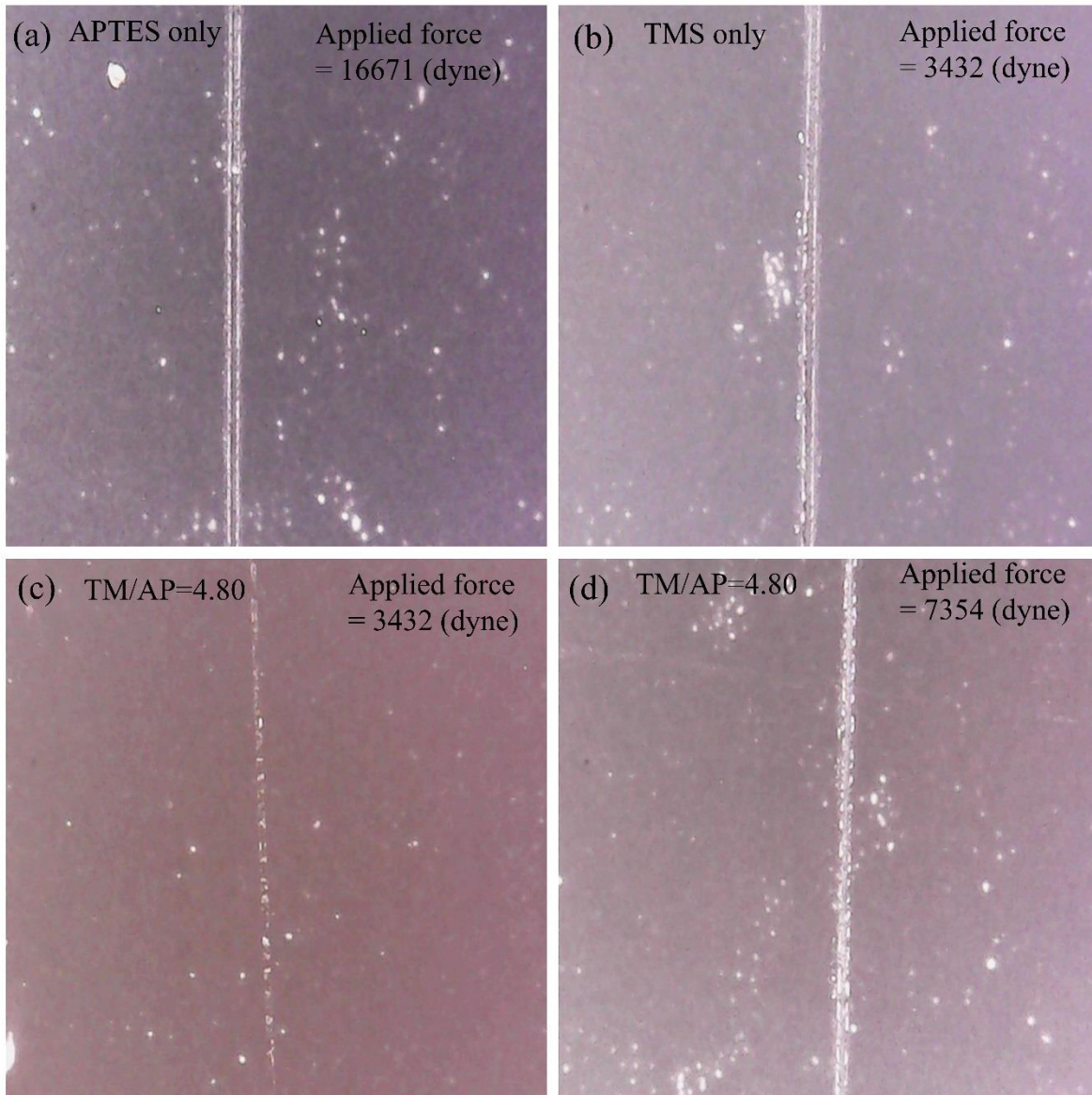


Figure 4.1.15. Scratch test photographs taken by the microscope.

4.4. Conclusions

The purpose of this work was to prepare a robust coating with good hydrophobic character as well as wear resistance by using non-thermal plasma jet with the mixture of two precursors. TMS was to promote hydrophobic character and APTES to increase the mechanical strength and durability owing to the presence of amines capable of promoting adhesion. The appropriate operating condition in terms of both hydrophobicity and mechanical strength was found to be the TMS/APTES ratio of 4.8, the applied voltage of 7.5 kV, and the treatment time of 300 s. At this condition, the WCA achieved was 139° . The aging and annealing tests have shown that the coating layer prepared on the glass is stable and durable. The AFM and SEM images indicated that the hydrophobic property of the coating is closely related to the thickness and roughness. According to the UV-Vis transmission spectra of the glass coated with the TMS and APTES mixture, there was no significant loss in the visibility. The non-thermal plasma jet operating at atmospheric pressure can be a promising candidate for the preparation of hydrophobic coating.

4.5. References

- [1] J. Genzer, K. Efimenko, Recent developments in superhydrophobic surfaces and their relevance to marine fouling: a review, *Biofouling*. 22 (2006) 339–360.
- [2] X.-M. Li, D. Reinhoudt, M. Crego-Calama, What do we need for a superhydrophobic surface? A review on the recent progress in the preparation of superhydrophobic surfaces, *Chem. Soc. Rev.* 36 (2007) 1350.
- [3] R. Múgica-Vidal, F. Alba-Elías, E. Sainz-García, J. Ordieres-Meré, Atmospheric plasma-polymerization of hydrophobic and wear-resistant coatings on glass substrates, *Surf. Coatings Technol.* 259 (2014) 374–385.
- [4] J.H. Yim, V. Rodriguez-Santiago, A.A. Williams, T. Gougousi, D.D. Pappas, J.K. Hirvonen, Atmospheric pressure plasma enhanced chemical vapor deposition of hydrophobic coatings using fluorine-based liquid precursors, *Surf. Coatings Technol.* 234 (2013).
- [5] D.J. Marchand, Z.R. Dilworth, R.J. Stauffer, E. Hsiao, J.H. Kim, J.G. Kang, S.H. Kim, Atmospheric rf plasma deposition of superhydrophobic coatings using tetramethylsilane precursor, *Surf. Coatings Technol.* 234 (2013) 14–20.
- [6] A. Ladwig, S. Babayan, M. Smith, M. Hester, W. Highland, R. Koch, R. Hicks, Atmospheric plasma deposition of glass coatings on aluminum, *Surf. Coatings Technol.* 201 (2007) 6460–6464.
- [7] A. Vogelsang, A. Ohl, R. Foest, K. Schröder, K.-D. Weltmann, Hydrophobic coatings deposited with an atmospheric pressure microplasma jet, *J. Phys. D: Appl. Phys.* 43 (2010) 485201.
- [8] R.E. Johnson, R.H. Dettre, Contact Angle Hysteresis. III. Study of an Idealized Heterogeneous Surface, *J. Phys. Chem.* 68 (1964) 1744–1750.
- [9] W. Barthlott, C. Neinhuis, Purity of the sacred lotus, or escape from contamination in biological surfaces, *Planta*. 202 (1997) 1–8.
- [10] A. Lafuma, D. Quéré, Superhydrophobic states, *Nat. Mater.* 2 (2003) 457–460.
- [11] H.K. Raut, V.A. Ganesh, A.S. Nair, S. Ramakrishna, Anti-reflective coatings: A critical, in-depth review, *Energy Environ. Sci.* 4 (2011) 3779.
- [12] S. Farhadi, M. Farzaneh, S.A. Kulinich, Anti-icing performance of superhydrophobic surfaces, *Appl. Surf. Sci.* 257 (2011) 6264–6269.

- [13] S. Chattopadhyay, Y.F. Huang, Y.J. Jen, A. Ganguly, K.H. Chen, L.C. Chen, Anti-reflecting and photonic nanostructures, *Mater. Sci. Eng. R Reports*. 69 (2010) 1–35.
- [14] C.-H. Xue, S.-T. Jia, J. Zhang, L.-Q. Tian, H.-Z. Chen, M. Wang, Preparation of superhydrophobic surfaces on cotton textiles, *Sci. Technol. Adv. Mater.* 9 (2008) 035008.
- [15] X. Zhang, F. Shi, J. Niu, Y. Jiang, Z. Wang, Superhydrophobic surfaces: from structural control to functional application, *J. Mater. Chem.* 18 (2008) 621–633.
- [16] J. Genzer, K. Efimenko, Recent developments in superhydrophobic surfaces and their relevance to marine fouling: A review, *Biofouling*. 22 (2006) 339–360.
- [17] M. Masuko, H. Miyamoto, A. Suzuki, Shear strength and durability of self assembled monolayer, 2007 Proc. ASME/STLE Int. Jt. Tribol. Conf. IJTC 2007. PART A (2008) 3–5.
- [18] I. Topala, M. Asandulesa, D. Spridon, N. Dumitrascu, Hydrophobic coatings obtained in atmospheric pressure plasma, *IEEE Trans. Plasma Sci.* 37 (2009) 946–950.
- [19] M.T. Laugier, An energy approach to the adhesion of coatings using the scratch test, *Thin Solid Films*. (1984).
- [20] J. Valli, U. Mäkelä, A. Matthews, V. Murawa, TiN coating adhesion studies using the scratch test method, *J. Vac. Sci. Technol. A Vacuum, Surfaces, Film*. (1985).
- [21] V.D. Jardret, W.C. Oliver, On the robustness of scratch testing for thin films: The issue of tip geometry for critical load measurement, in: *Thin Film. Mech. Prop.* Viii, 2000.
- [22] A.J. Perry, The adhesion of chemically vapour-deposited hard coatings to steel-the scratch test, *Thin Solid Films*. (1981).
- [23] R.L. Browning, G.T. Lim, A. Moyse, H.J. Sue, H. Chen, J.D. Earls, Quantitative evaluation of scratch resistance of polymeric coatings based on a standardized progressive load scratch test, *Surf. Coatings Technol.* (2006).
- [24] S.J. Bull, E. G.-Berasetegui, Chapter 7 An overview of the potential of quantitative coating adhesion measurement by scratch testing, *Tribol. Interface Eng. Ser.* (2006).
- [25] P.A. Steinmann, Y. Tardy, H.E. Hintermann, Adhesion testing by the scratch test method: The influence of intrinsic and extrinsic parameters on the critical load, *Thin Solid Films*. (1987).
- [26] J. Valli, U. Mäkelä, Applications of the scratch test method for coating adhesion assessment, *Wear*. (1987).
- [27] ASTM (American Society for Testing and Materials), D7027 - Standard Test Method for

- Evaluation of Scratch Resistance of Polymeric Coatings and Plastics Using an Instrumented Scratch Machine, ASTM Int. (2013).
- [28] P. Richard, J. Thomas, D. Landolt, G. Gremaud, Combination of scratch-test and acoustic microscopy imaging for the study of coating adhesion, *Surf. Coatings Technol.* (1997).
- [29] R.S.R. Kalidindi, R. Subasri, Sol-gel nanocomposite hard coatings, in: *Anti-Abrasive Nanocoatings Curr. Futur. Appl.*, 2014.
- [30] L. Kilpi, O.M.E. Ylivaara, A. Vaajoki, J. Malm, S. Sintonen, M. Tuominen, R.L. Puurunen, H. Ronkainen, Microscratch testing method for systematic evaluation of the adhesion of atomic layer deposited thin films on silicon, *J. Vac. Sci. Technol. A Vacuum, Surfaces, Film.* 34 (2016) 01A124.
- [31] Q.H. Trinh, S.B. Lee, Y.S. Mok, Hydrophobic Coating of Silicate Phosphor Powder Using Atmospheric Pressure Dielectric Barrier Discharge Plasma, *Am. Inst. Chem. Eng.* 60 (2014) 829–838.
- [32] S. Sportouch, C. Lacoste, R. Gaufrés, Spectres Raman du néopentane et du tétraméthylsilane à l'état gazeux, *J. Mol. Struct.* 9 (1971) 119–127.
- [33] N. Herlin, M. Lefebvre, M. Pealat, J. Perrin, Investigation of the Chemical Vapor Deposition of Silicon Carbide from Tetramethylsilane by in Situ Temperature and Gas Composition Measurements, *J. Phys. Chem.* 96 (1992) 7063–7072.
- [34] D. Ball, T. Carter, D. McKean, L. Woodward, Raman and infra-red spectra of methyl silane and some deuterated derivatives, *Spectrochim. Acta.* 20 (1964) 1721.
- [35] M. Gueye, T. Gries, C. Noël, S. Migot-Choux, S. Bulou, E. Lecoq, P. Choquet, K. Kutasi, T. Belmonte, Interaction of (3-Aminopropyl)triethoxysilane with Pulsed Ar–O₂ Afterglow: Application to Nanoparticles Synthesis, *Plasma Chem. Plasma Process.* 36 (2016) 1031–1050.
- [36] V.R. Rai, S. Agarwal, Mechanism of self-catalytic atomic layer deposition of silicon dioxide using 3-aminopropyl triethoxysilane, water, and ozone, *Chem. Mater.* 23 (2011) 2312–2316.
- [37] P.J. Launer, Infrared Absorption Bands Characteristic of the Si-CH₂CH₂CN and Si-CH₂CH₂CH₂CN Groups, *Silicon Compd. Regist. Rev.* (1987) 100–103.
- [38] I.A. Rahman, M. Jafarzadeh, C.S. Sipaut, Synthesis of organo-functionalized nanosilica via a co-condensation modification using γ -aminopropyltriethoxysilane (APTES), *Ceram. Int.*

- 35 (2009) 1883–1888.
- [39] H. Okabayashi, I. Shimizu, E. Nishio, C.J. OConnor, Diffuse reflectance infrared Fourier transform spectral study of the interaction of 3-aminopropyltriethoxysilane on silica gel. Behavior of amino groups on the surface, *Colloid Polym. Sci.* 275 (1997) 744–753.
- [40] L.D. White, C.P. Tripp, Reaction of (3-Aminopropyl)dimethylethoxysilane with Amine Catalysts on Silica Surfaces, *J. Colloid Interface Sci.* 232 (2000) 400–407.
- [41] J.N. Borges, T. Belmonte, J. Guillot, D. Duday, M. Moreno-Couranjou, P. Choquet, H.N. Migeon, Functionalization of copper surfaces by plasma treatments to improve adhesion of epoxy resins, in: *Plasma Process. Polym.*, 2009.
- [42] V. Gubala, R.P. Gandhiraman, C. Volcke, C. Doyle, C. Coyle, B. James, S. Daniels, D.E. Williams, Functionalization of cycloolefin polymer surfaces by plasma-enhanced chemical vapour deposition: comprehensive characterization and analysis of the contact surface and the bulk of aminosiloxane coatings, *Analyst.* 135 (2010) 1375–1381.
- [43] C. Volcke, R.P. Gandhiraman, V. Gubala, C. Doyle, G. Fonder, P.A. Thiry, A.A. Cafolla, B. James, D.E. Williams, Plasma functionalization of AFM tips for measurement of chemical interactions, *J. Colloid Interface Sci.* 348 (2010) 322–328.
- [44] C. Volcke, R.P. Gandhiraman, V. Gubala, J. Raj, T. Cummins, G. Fonder, R.I. Nooney, Z. Mekhalif, G. Herzog, S. Daniels, D.W.M. Arrigan, A.A. Cafolla, D.E. Williams, Reactive amine surfaces for biosensor applications, prepared by plasma-enhanced chemical vapour modification of polyolefin materials, *Biosens. Bioelectron.* 25 (2010) 1875–1880.
- [45] W. Juda, Preparation of Ion Exchange Membranes, *J. Appl. Polym. Sci.* 5193 (1953) 875–884.
- [46] Y. Liu, Y. Li, X.M. Li, T. He, Kinetics of (3-aminopropyl)triethoxysilane (aptes) silanization of superparamagnetic iron oxide nanoparticles, *Langmuir.* 29 (2013) 15275–15282.
- [47] J.A. Howarter, J.P. Youngblood, Surface modification of polymers with 3-aminopropyltriethoxysilane as a general pretreatment for controlled wettability, *Macromolecules.* 40 (2007) 1128–1132.
- [48] C.L. Loch, D. Ahn, Chen, J. Wang, Z. Chen, Sum Frequency Generation Studies at Poly(ethylene terephthalate)/Silane Interfaces: Hydrogen Bond Formation and Molecular Conformation Determination, *Langmuir.* 20 (2004) 5467–5473.

- [49] J.H. Yim, V. Rodriguez-Santiago, A.A. Williams, T. Gougousi, D.D. Pappas, J.K. Hirvonen, Atmospheric pressure plasma enhanced chemical vapor deposition of hydrophobic coatings using fluorine-based liquid precursors, *Surf. Coatings Technol.* 234 (2013) 21–32.
- [50] F. Alba-Elías, J. Ordieres-Meré, A. González-Marcos, Deposition of thin-films on EPDM substrate with a plasma-polymerized coating, *Surf. Coatings Technol.* 206 (2011) 234–242.
- [51] J. Schäfer, R. Foest, A. Quade, A. Ohl, J. Meichsner, K.D. Weltmann, Carbon-free SiO_x films deposited from octamethylcyclotetrasiloxane (OMCTS) by an atmospheric pressure plasma jet (APPJ), *Eur. Phys. J. D.* 54 (2009) 211–217.
- [52] T.J. Lin, J.A. Antonelli, D.J. Yang, H.K. Yasuda, F.T. Wang, Plasma treatment of automotive steel for corrosion protection - a dry energetic process for coatings, *Prog. Org. Coatings.* 31 (1997) 351–361.
- [53] K.T.L. Trinh, H. Zhang, D.J. Kang, S.H. Kahng, B.D. Tall, N.Y. Lee, Fabrication of polymerase chain reaction plastic Lab-on-a-Chip device for rapid molecular diagnoses, *Int. Neurourol. J.* 20 (2016) S38–S48.
- [54] V.M. Gun'ko, O. Seledets, J. Skubiszewska-Zięba, V.I. Zarko, R. Lebeda, W. Janusz, S. Chibowski, Phosphorus-containing carbon deposits on silica gel Si-100, *Microporous Mesoporous Mater.* 87 (2005) 133–145.
- [55] C.-W. Kan, C.-H. Kwong, S.-P. Ng, Atmospheric Pressure Plasma Surface Treatment of Rayon Flock Synthetic Leather with Tetramethylsilane, *Appl. Sci.* 6 (2016) 59.
- [56] Y. Li, J. Zhang, S. Zhu, H. Dong, F. Jia, Z. Wang, Z. Sun, L. Zhang, Y. Li, H. Li, W. Xu, B. Yang, Biomimetic surfaces for high-performance optics, *Adv. Mater.* 21 (2009) 4731–4734.

CHAPTER-5

Formation of plasma-polymerized superhydrophobic coating using an atmospheric-pressure plasma jet

Highlights

- DBD plasma used to make superhydrophobic surface.
- TMS and APDMES used as precursors to study the coating layers.
- Robust coating layer formed on the glass surface.
- Deposition was confirmed by FE-SEM and 3D nano profiler.
- No significant loss in the visibility region.

5.1. Introduction

Non-thermal plasma (NTP) polymerization processes are of considerable interest because they can effectively produce protective or hydrophobic coating layers on the surfaces of various materials such as glasses, fabrics, powders and polymers [1–9] with low cost. The surface wettability is determined by the measurement of water contact angle (WCA). The surfaces having more than 150° of WCA are known as superhydrophobic surfaces that are highly repellent to water. These surfaces have many applications such as self-cleaning windshields [10–14], anti-contamination [15,16], anti-sticking of snow for windows and antennas [17,18], anti-biofouling paints for boats [19–22], anti-icing [23,24], anti-corrosion [25–28], etc. The wettability of a solid surface is a property that depends on both surface roughness and surface chemistry [29–31], and directly related to the surface free energy. Basically, materials with low surface energies are used to prepare superhydrophobic surfaces.

Many research groups have tried to make durable superhydrophobic surfaces over metals, organic or inorganic substrates [32–39]. Long-lasting hydrophobic coatings are not easily achievable with only low surface energy materials, mainly because of their poor adhesion nature to solid surfaces. Low surface energy materials such as hexamethyldisiloxane (HMDSO, $\text{O}[\text{Si}(\text{CH}_3)_3]_2$), pentamethyldisiloxane (PMDSO, $\text{C}_5\text{H}_{16}\text{OSi}_2$), tetramethyldisiloxane (TMDSO, $[(\text{CH}_3)_2\text{SiH}]_2\text{O}$), tetramethylsilane (TMS, $\text{Si}(\text{CH}_3)_4$), trimethylsilane (TriMS, $\text{HSi}(\text{CH}_3)_3$) and tetraethyl orthosilicate (TEOS, $\text{Si}(\text{OC}_2\text{H}_5)_4$) are well-known organosilicon precursors capable of forming hydrophobic layers. Conventional chemical polymerizations have a drawback of poor adhesion on solid surfaces, and as well, the coating layers created do not function well after several scratches due to their chemical nature [40–42]. For industrial applications, wear resistance and adhesive properties are critical factors. The poor adhesive property may be improved by

incorporating aminopropylethoxysilanes that are silanating agents for modifying the surface of silica-based materials. The aminosilanes anchor to the surface, forming Si-O-Si covalent bond and hydrogen bonding with the amino group. Among aminosilanes, (3-aminopropyl)triethoxysilane (APTES, $\text{H}_2\text{N}(\text{CH}_2)_3\text{Si}(\text{OC}_2\text{H}_5)_3$) and 3-aminopropyl(diethoxy)methylsilane (APDMES, $\text{CH}_3\text{Si}(\text{OC}_2\text{H}_5)_2(\text{CH}_2)_3\text{NH}_2$) have widely been used along with low surface energy materials.

For the present work, an attempt has been made to produce stable superhydrophobic coating films on glass substrates with an atmospheric-pressure plasma jet generated by dielectric barrier discharge (DBD). The DBD plasma jet was created using a glass tube and stainless steel needles. The precursors for the coating were TMS and APDMES. TMS is the simplest tetraorganosilane with low surface energy, leading to hydrophobicity, and APDMES can a good promoter imparting robustness. The primary goal of the work is to find optimal condition that results in the formation of superhydrophobic coating layer with good stability.

5.2. Experimental

5.2.1. Materials

Two precursors TMS (≥ 99.0 (GC)) and APDMES (97%) were purchased from Sigma-Aldrich (USA), which were used without further purification. Argon (99.99%) was used to generate plasma discharge, and nitrogen (99.99%) was used as the shielding gas to protect the plasma jet from the interference of oxygen and water vapor diffused from ambient air.

5.2.2. Preparation of the plasma reactor and scratch tester

The schematic diagram of the plasma polymerization system is depicted in Figure 5.1.1. The DBD reactor creating plasma jet was made with a glass tube, in which three stainless steel needles arranged at 120° intervals to one another were inserted. The needles served as high voltage

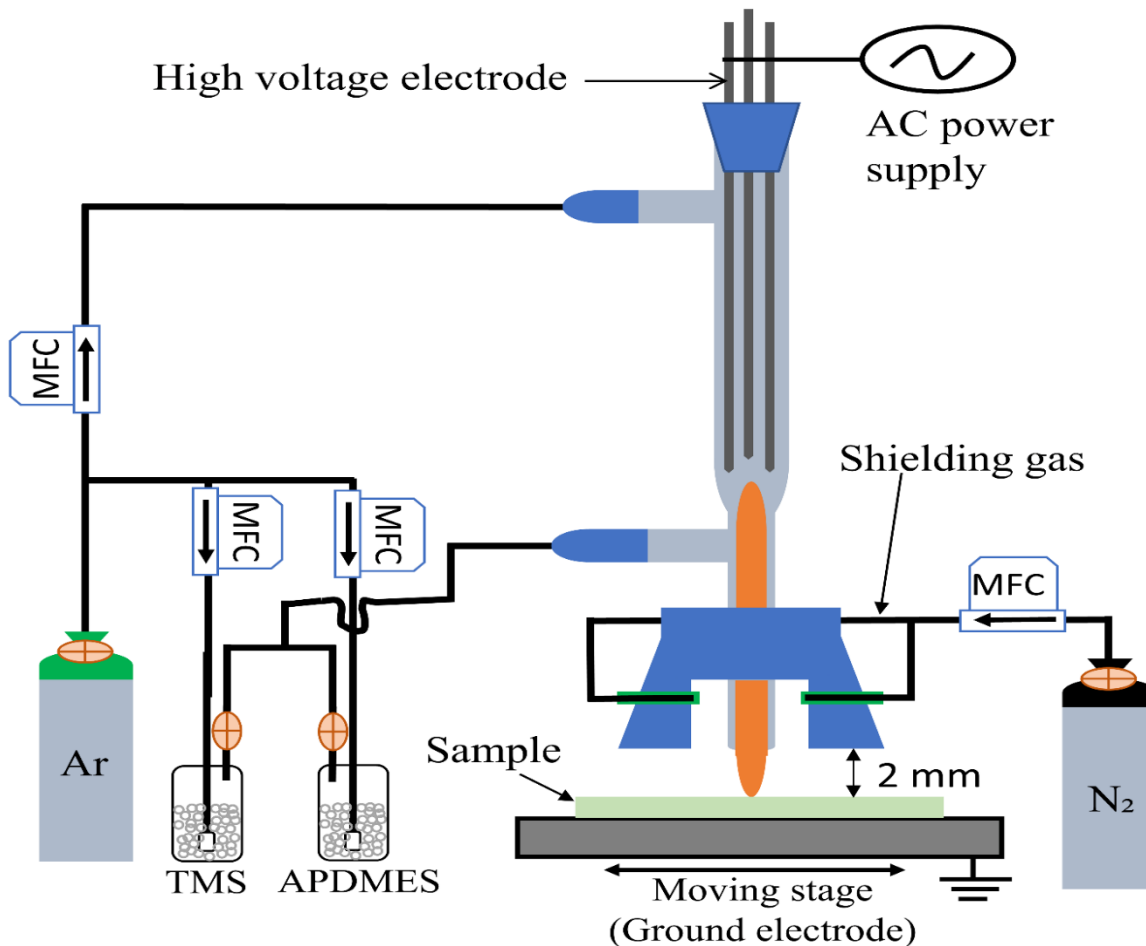


Figure 5.1.1. Schematic diagram of the plasma jet reactor system.

(HV) electrode. The plasma reactor was operated with a high-voltage alternating current (AC) power source (Korea Switching Co., Korea) whose frequency output was set to 11.5 kHz. The outer and inner diameter of the glass tube was 8.0 and 5.0 mm, respectively. The distance between the HV electrode tip and the end of the glass tube was kept constant at 75 mm. The gap between the end of the tube and the glass substrate was 2 mm. The substrate sample held on a Teflon plate reciprocated below the stationary plasma jet at a speed of 90 mm/s.

A home-made scratch tester shown in Figure 5.1.2 was employed to examine the mechanical stability of the coating layer. For a commercially available scratch test, a diamond tip

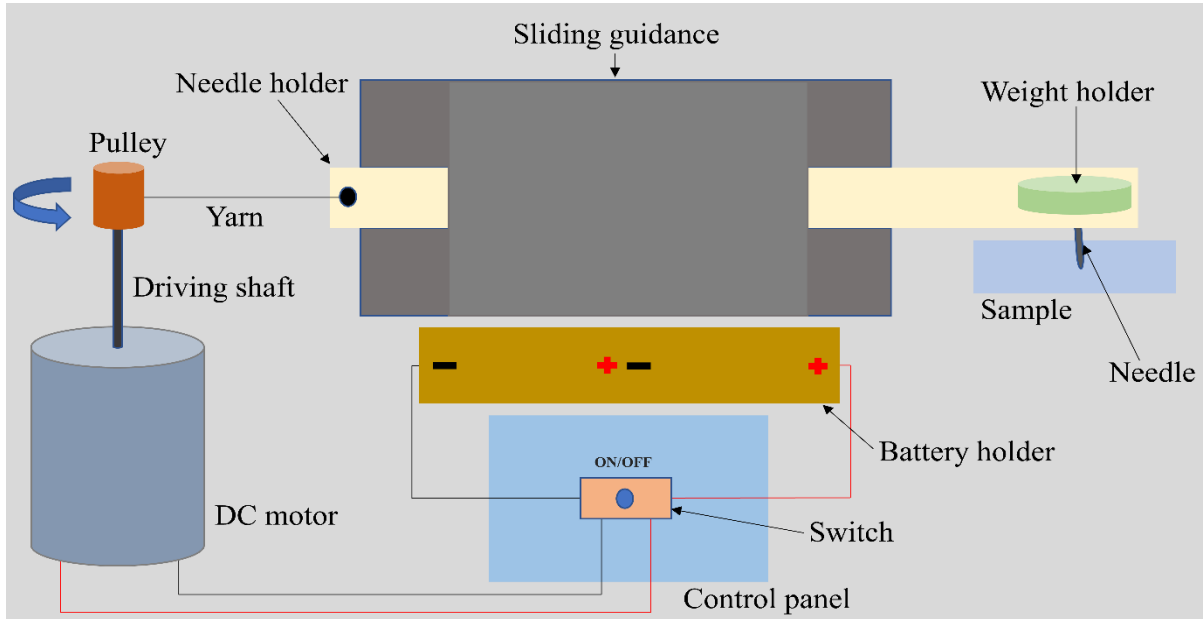


Figure 5.1.2. Schematic diagram of the home-made scratch tester.

moves on the surface to make a scratch with either constant or progressively increasing load [43]. Usually, the normal force, tangential force, friction coefficient, acoustic emission, and penetration depth are measured continuously during the scratch test [43]. The scratch tester in Figure 5.1.2 was mainly composed of a dc motor driving a needle (tip radius: 0.25 mm) to move on the sample's surface for creating a scratch with predetermined vertical loads. The yarn was used to connect the motor's driving shaft to the needle holder. The needle holder guided by a sliding guide traveled horizontally back and forth. The sample for testing was put under the tip of the needle and fixed by a double-sided tape so that the samples did not move during scratching. Before and after a scratch test, the needle tip was cleaned with ethanol and tissue wiper. The moving speed of the tip was set to 37 mm/s and the length of the scratch was around 10 mm. The breakdown force of the coating layer was measured by varying the load applied to the sample.

5.2.3. Preparation of coating

The plasma-induced polymerization of TMS and APDMES was performed on soda-lime glass substrates with the dimensions of 75 mm × 27 mm × 1.2 mm. The flow rate of argon was typically 2.5 L/min, and that of nitrogen was also 2.5 L/min. Thus, the total gas flow rate was 5 L/min. Argon and nitrogen were separately fed into the system. The mass flow controllers (MFCs) were used to control the flow rates of the feed gases. APDMES and TMS contained in Pyrex flasks were delivered to the plasma reactor by bubbling them with argon. The concentration of APDMES was changed from 135 to 324 ppm (parts per million, volumetric) using its vapor pressure varying according to the temperature, while the concentration of TMS was kept constant at 135 ppm. The effects of the addition of APDMES on the stability and hydrophobicity of the coating were examined at the APDMES/TMS (A/T) ratios of 1, 1.4, 1.7, and 2.4. The area of the coating was estimated to be around 1500 mm².

5.2.4. Characterizations

The surface morphology and roughness of the coatings were analyzed by a field emission scanning electron microscopy (FESEM, JSM-6700F, JEOL, Japan) at an operating voltage of 15 kV and a 3D nano-profiling system (3D Optical Surface Profiler, NV-2200, Nanosystem, Korea). Static WCAs of the coatings were measured by a goniometer (Phonix 300, Surface & Electro-Optics Co., Ltd., Korea) using the sessile drop technique by dropping about 5 μL of distilled water on the surface. The composition of the deposited thin film and chemical properties were investigated by Fourier transform infrared spectroscopy (FTIR, FTIR-7600, Lambda Scientific, Australia) and X-ray photoelectron spectroscopy (XPS). The mechanical stability of the coating layer was examined by the scratch tester depicted in Figure 5.1.2. The wear tracks were observed

by an optical microscope (2MP 1000X 8 LED USB Digital Microscope Endoscope Zoom Camera, A4Tech, Taiwan).

5.3. Results and discussion

5.3.1. Water contact angle measurements

The quality of the thin film produced by the plasma jet depends on the parameters such as the treatment time, the applied voltage (or plasma intensity), the A/T ratio, and the gas flow rate. Figure 5.1.3 shows the dependence of the WCA on these parameters. First, the treatment time was varied from 10 to 60 s with keeping the A/T ratio, the applied voltage and the gas flow rate constant at 1.7, 7.5 kV, and 5 L/min (Ar: 2.5 L/min; N₂: 2.5 L/min), respectively. As seen in Figure 5.1.3 (a), the WCA was changed from 128 to 162° with increasing the treatment time from 10 to 60 s. As well known, the WCA is closely related to the surface roughness and thickness. With a short treatment time of 10 to 20 s, the surface roughness and coverage were relatively poor. Longer treatment time allowed more deposition of APDMES-TMS copolymer on the surface, leading to thicker coating layer with more roughness and surface coverage. However, after a certain limit, further increase of WCA was not observed because the thickness increased but surface roughness and coverage remained almost similar. It should also be noted that the thicker the thin film, the lower the transparency of the coated sample. In consideration of both WCA and transparency, 40 s was chosen for the treatment time. At this treatment time, the WCA was 163°. As a next step, an appropriate applied voltage was determined with fixing the treatment time at 40 s.

The effect of the applied voltage on the WCA was examined at voltages up to 8 kV with the H/A ratio, the treatment and the flow rate kept constant at 1.7, 40 s and 5 L/min, respectively. Figure 5.1.3(b) shows the variations of the WCA according to the changes in the voltage applied

to the plasma reactor. Basically, the higher the applied voltage, the more intense the plasma jet was, leading to the enhancements of the deposition rate and the formation of particulates in the gas

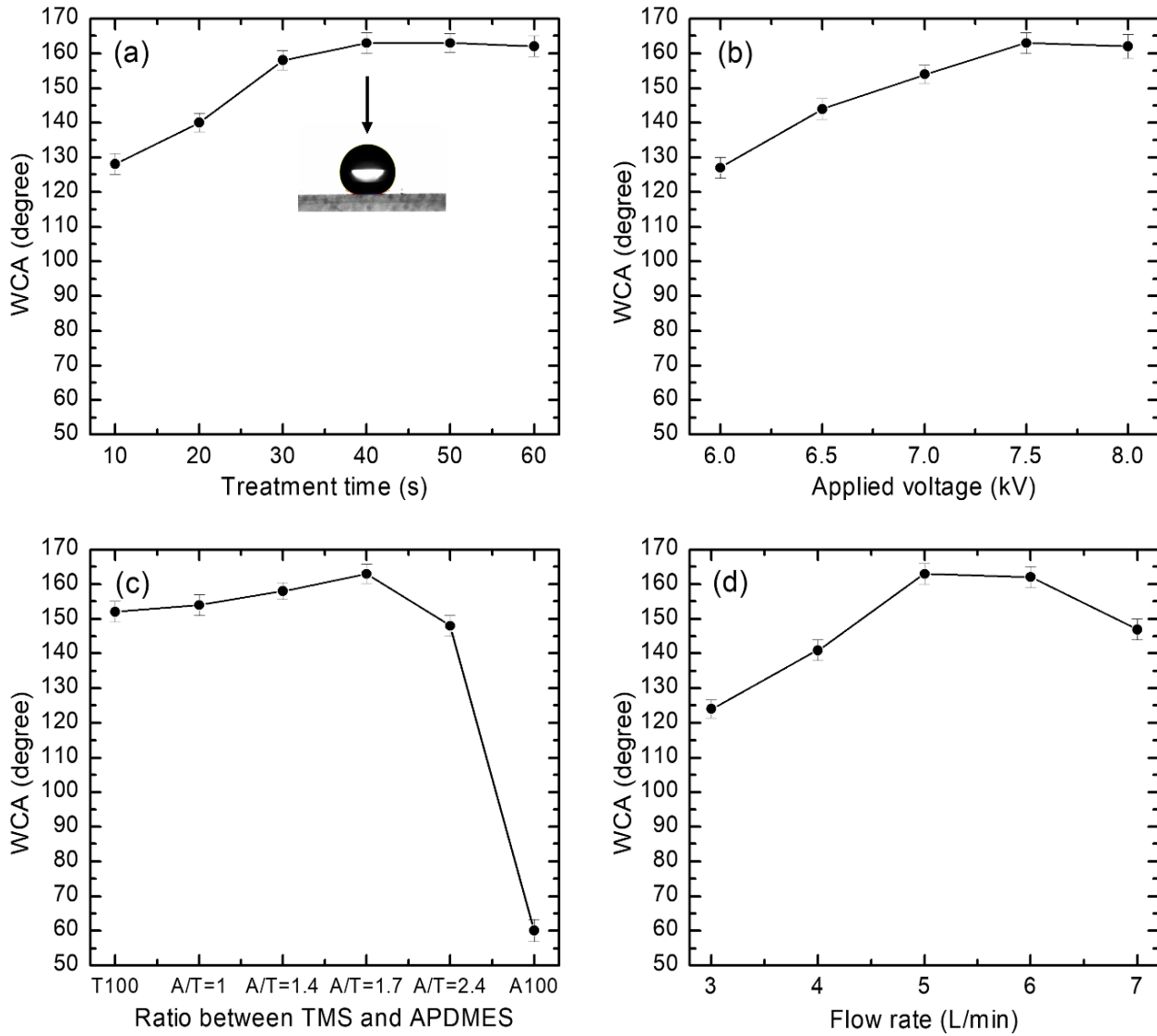


Figure 5.1.3. Dependence of WCA on (a) the treatment time, (b) the applied voltage, (c) the A/T ratio and (d) the total flow rate of the carrier gases.

phase. The formation of particulates from APDMES and TMS, called dusty plasma, is prerequisite to obtain rough surfaces. The WCA increased with increasing the voltage from 6 to 7.5 kV, but there was no significant change in the WCA when the voltage was further increased to 8 kV. Thus, 7.5 kV was selected for the appropriate applied voltage.

With the treatment time of 40 s and the voltage of 7.5 kV determined above, a set of experiments were carried out to find out an appropriate A/T ratio. The dependence of WCA on the A/T ratio is presented in Figure 5.1.3 (c), when the total gas flow rate was 5 L/min (Ar: 2.5 L/min; N₂: 2.5 L/min). For the purpose of comparison, the WCA obtained with APDMES alone (A100) and TMS alone (T100) are also given in this figure. Due to the hydrophilic nature of APDMES, the A100 sample exhibited a low WCA of 60°. On the other hand, the TMS-alone sample showed superhydrophobicity with a WCA of 152°. Despite the hydrophilic nature of APDMES, however, the coatings prepared with the mixture of these two precursors exhibited increases in the WCA from 154 to 163° as the A/T ratio was increased from 1 to 1.7. But, further increase in the A/T ratio to 2.4 led to a decrease in the WCA, suggesting that the coating layer begins to change toward hydrophilic at around this A/T ratio. From the results in Figure 5.1.3 (c), the appropriate A/T ratio was determined to be 1.7.

Finally, the total gas flow rate of argon and nitrogen was varied from 3 to 7 L/min to understand its effect on the WCA. Even if the total flow rate was changed, argon and nitrogen were supplied at the same flow rate. The treatment time, the applied voltage, and the A/T ratio were kept constant at 40 s, 7.5 kV, and 1.7, respectively. Figure 5.1.3 (d) shows the effect of the gas flow rate on the WCA. From 3 to 5 L/min, the plasma jet was observed to be more intense, increasing the WCA from 124 to 160°. But after 5 L/min, the WCA started to decrease, implying that there is not enough time for the formation of particulates from APDMES and TMS when the

flow rate is too high (i.e., decrease in the residence time). As understood from Figure 5.1.3 (d), the best result was obtained at a total flow rate of 5 L/min.

5.3.2. Surface morphology and roughness

The 3D nano-profiler and FESEM analyses were conducted to investigate the surface morphology, roughness, and the coating thickness. The root-mean-square (RMS) roughness and thickness of the coating are summarized in Table 5.1.1. The 3D nano-profiler images of the selected samples (A100, T100, and A/T=1.7) are presented in Figure 5.1.4, where it can be seen that the number of needle-like peaks corresponding to the surface roughness is different from one another, depending on the precursor composition. The 3D nano-profiler images showed that the A100 sample had the lowest surface roughness. When the precursor mixture of APDMES and TMS was used, the roughness substantially increased, leading to an increase in WCA, which agrees well with the results given in Figure 5.1.3. The formation of rough surfaces having nano-scale

Table 5.1.1. Thickness and RMS roughness of each sample.

Sample	Thickness (nm)	RMS roughness (nm)
A	207	30.45
T	385	111.32
A/T=1	422	118.92
A/T=1.4	451	134.21
A/T=1.7	470	137.62
A/T=2.4	494	105.32

topographic features results from the generation of particulates through gas-phase condensation reactions of the precursor fragments produced by the plasma jet. The deposition of the particulates on the surface forms a thin coating layer.

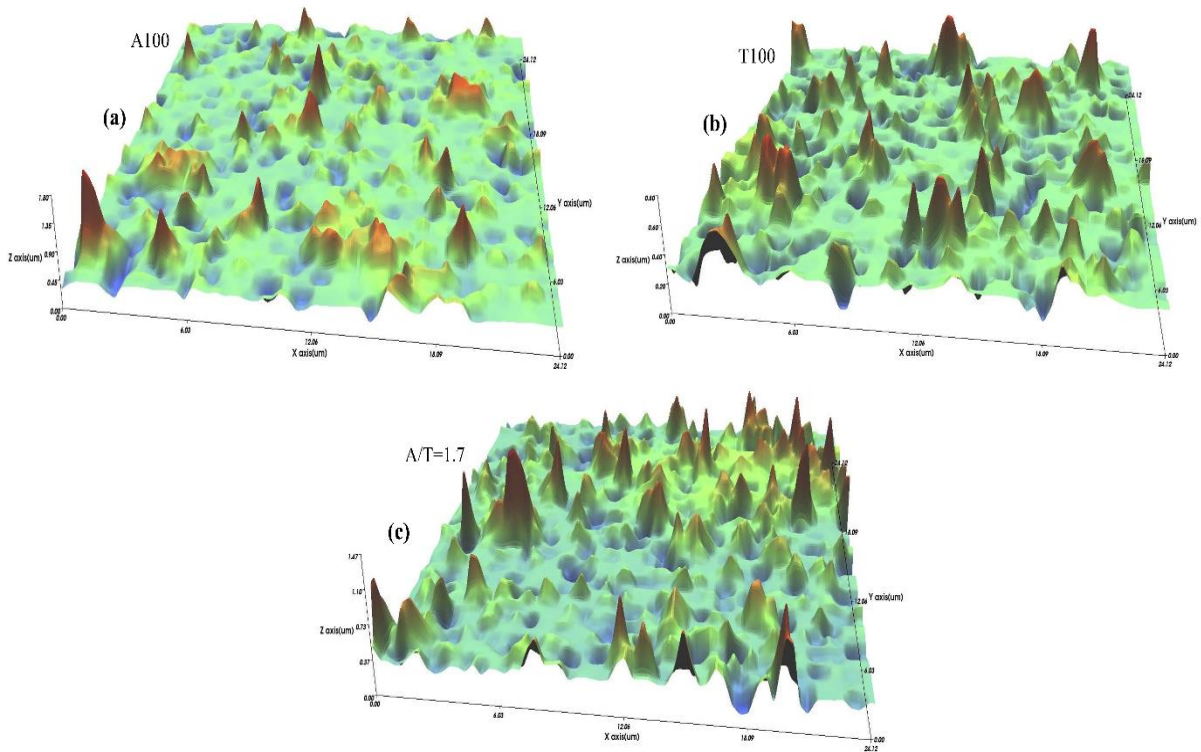


Figure 5.1.4. 3D nano-profiler images of the selected samples. (a) A100; (b) T100; and (c) A/T=1.7.

The FE-SEM images of the selected samples (A100, T100, and A/T=1.7) are shown in Figure 5.1.5, where nano-structure particles of different sizes in the range of 70 to 200 nm can be observed. In case of the A100 sample (Figure 5.1.5 (a)), the nanoparticles deposited on the surface

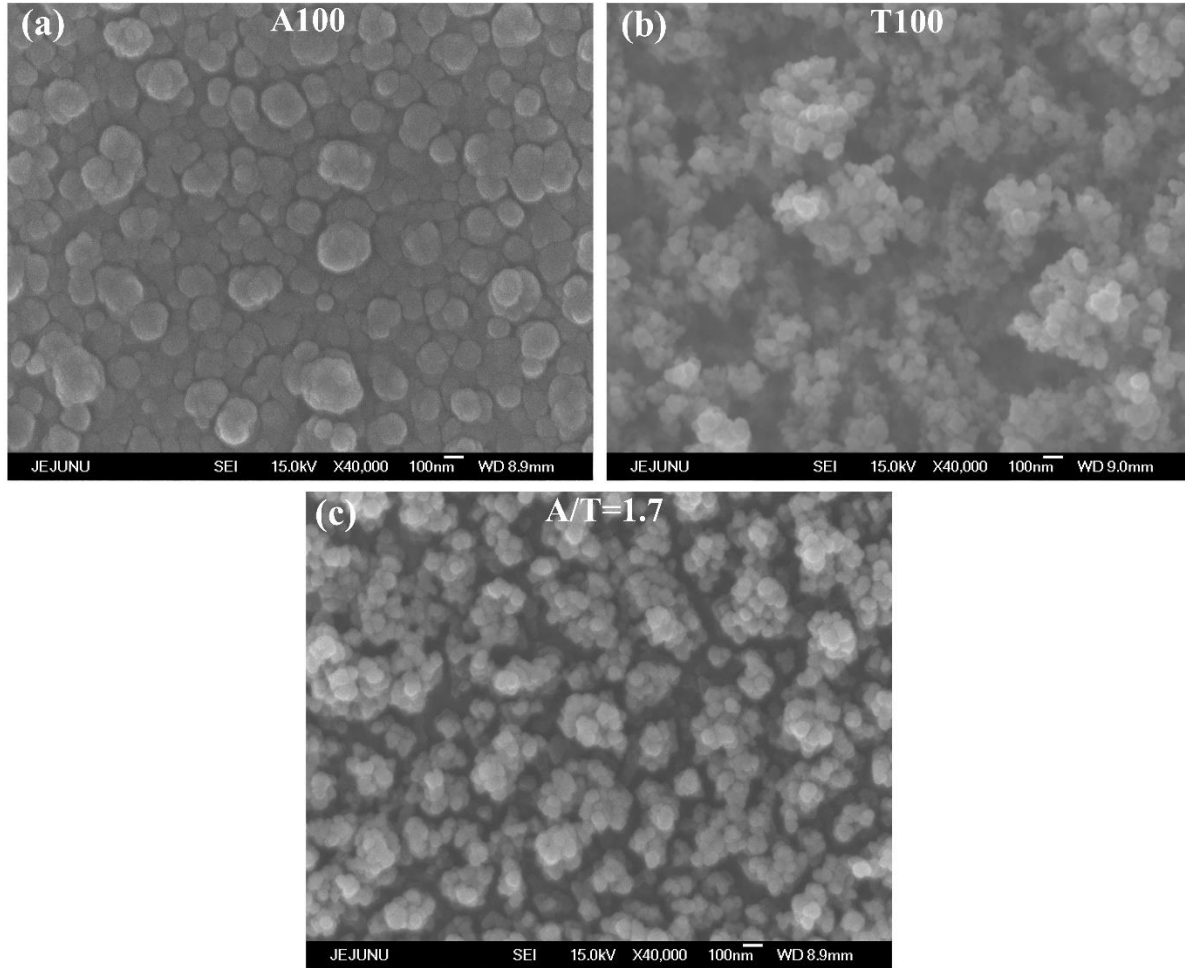


Figure 5.1.5. FE-SEM images of the selected samples. (a) A100; (b) T100; and (c) A/T=1.7.

look like smooth circular islands of different sizes. The surface anchoring mechanism of APDMES on the surface with silanol groups can be explained by the formation of bonds between the amino group and the hydroxyl group [44,45]. Each APDMES occupies two silanol sites: one hydroxyl group in silanol forms a Si-O-Si bridge and the other forms H-bonding with the amine group in APDMES. Different from the surface morphology of A100, the samples T100 and A/T=1.7 exhibited rougher surface structures, which are consistent with the 3D nano-profiler images.

5.3.3. Stability tests

The stability of the coating was examined by performing natural and thermal aging. All the samples were stored in centrifuge tubes at room temperature. Aging time may have a significant effect on WCA for the powder coating. Trinh et al. [46] reported that the WCA could increase by 15° to 40° within 30-day natural aging after the hydrophobic coating was carried out on the phosphor powder substrate. Unlike the power substrate coating, the WCA of the glass surface was hardly affected by the aging (15 days, 30 days, and 90 days) (Figure 5.1.6 (a)), indicating that the coating formed on the glass surface has physicochemical stability. The thermal stability of the

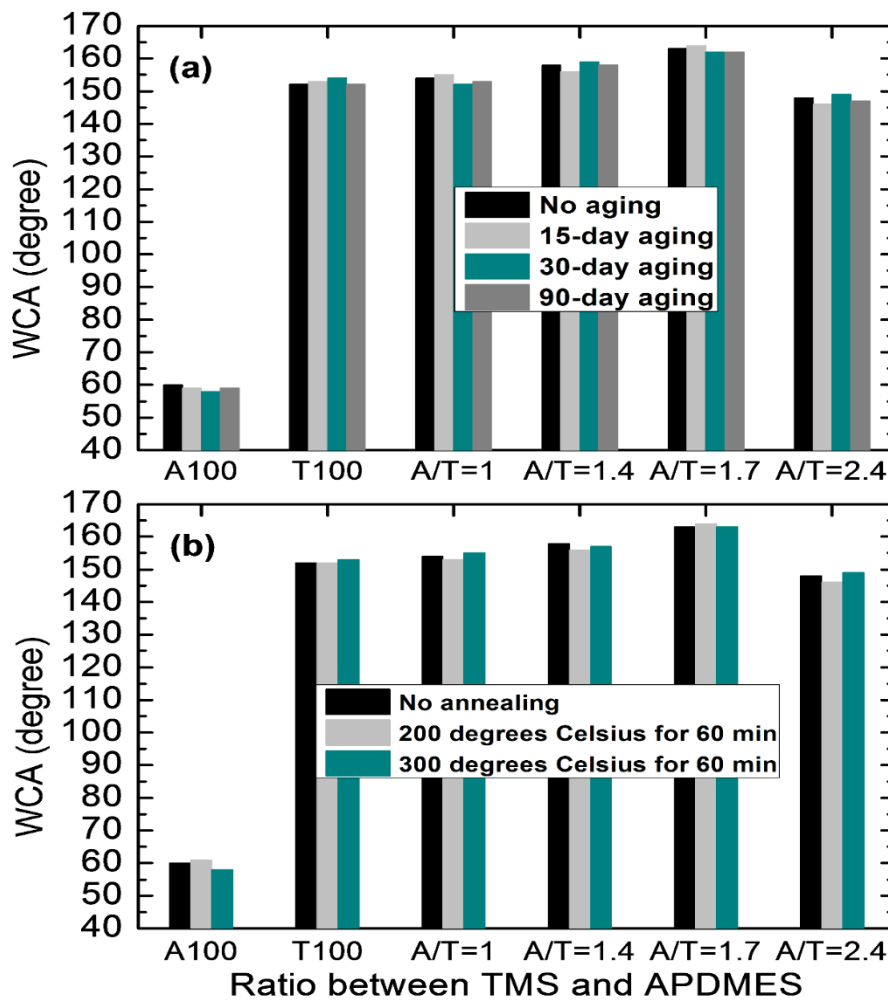


Figure 5.1.6. Effect of (a) aging time and (b) annealing temperature on the WCA.

coating was examined by annealing tests at 200 and 300°C for 1 h. As can be seen in Figure 5.1.6 (b), the annealing did not nearly affect the WCA for all the samples.

5.3.4. Spectroscopic analyses

The FTIR analyses were conducted for the chemical characterizations of the coating layers, and the results are presented in Figure 5.1.7. Since the soda-lime glass is not transparent to infrared, potassium bromide (KBr) disks were used to deposit the polymer thin films under the same experimental condition. The infrared spectra were collected by taking an average of 10 scans at 1 cm^{-1} resolution in the range of 500 to 3500 cm^{-1} using the absorbance mode. The backbone of the

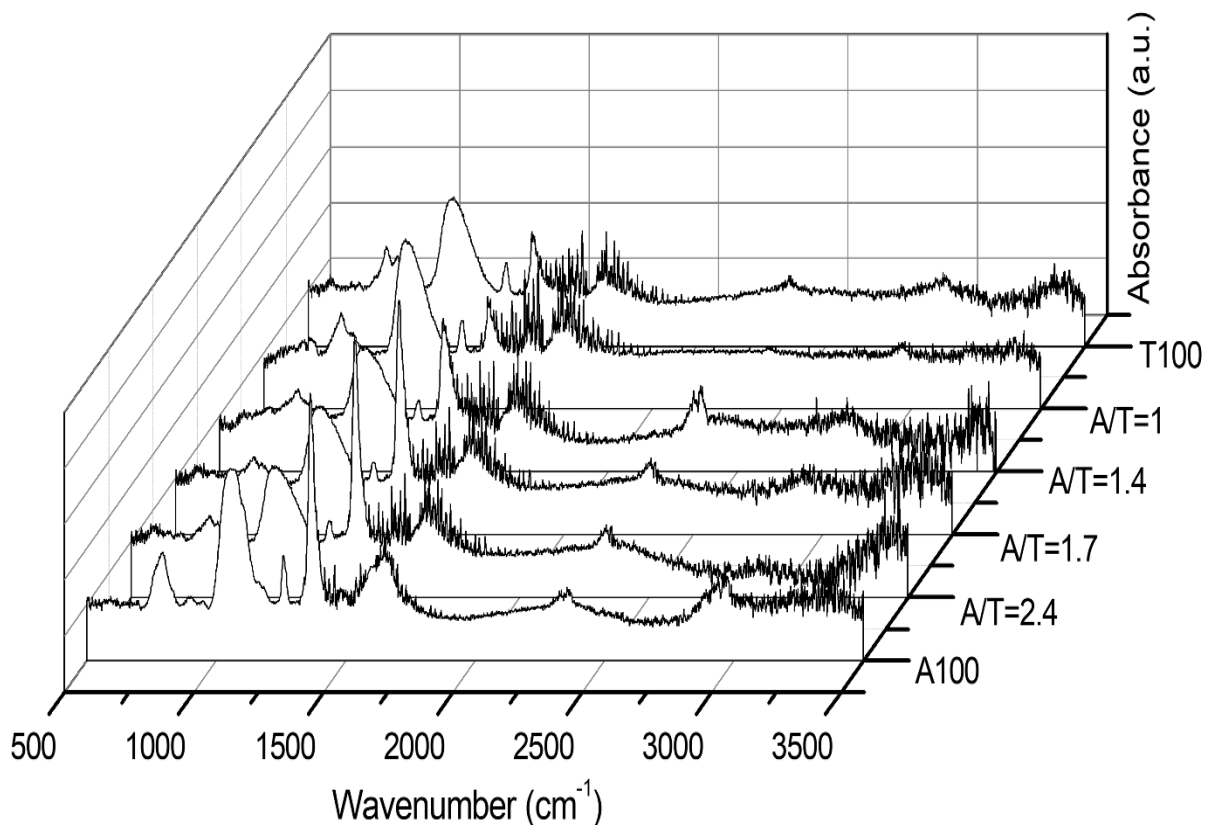


Figure 5.1.7. FTIR spectra of the samples prepared at different A/T ratios.

coating Si-O-Si is found at 1047 cm^{-1} [47,48]. Si-O-Si is often related to the improvement in wear resistance. Si-C stretching appears at 800 cm^{-1} [48], and Si-O stretching in Si-OH is seen at 825 to 940 cm^{-1} [48–50]. The Si-CH₃ symmetric deformation is related to the absorption bands at 1260 cm^{-1} , 1350 cm^{-1} , 1366 cm^{-1} and 2966 cm^{-1} ; the absorption bands at 1260 cm^{-1} , 1350 cm^{-1} and 1366 cm^{-1} are medium in intensity and that at 2966 cm^{-1} is weak in intensity [47,51]. These peaks grew as the amount of APDMES increased. The noisy peaks at around 1600 cm^{-1} are due to the moisture attached to the KBr substrate. The peaks of CO₂ from $2340\text{--}2360\text{ cm}^{-1}$ are seen due to the presence of CO₂ in the ambient environment [52].

The XPS analyses were performed on three representative samples, namely, T100, A100, and A/T=1.7 (Figure 5.1.8). All the three samples contain silicon (Si), carbon (C), oxygen (O), and nitrogen (N) in different atomic compositions. The T100 sample exhibited 38% of carbon, 32.5% of oxygen, 28.1% of silicon, and 1.4% of nitrogen. The low nitrogen content of this sample is due to no nitrogen atom in TMS. In comparison, the sample A100 contained 49.7% of oxygen, 21.3% of carbon, 24.5% of silicon, and 4.5% of nitrogen, while the atomic composition of the sample A/T=1.7 is 37.2% of oxygen, 40.8% of carbon, 18.8% of silicon, and 3.2% of nitrogen. Figure 5.1.9 shows the C1s spectra deconvolution results for the three samples (T100, A100, and A/T=1.7), and Table 5.1.2 summarizes the peak positions of C1s with the corresponding functional groups. The peak at 284.7 eV corresponds to the presence of H-C or C-C [53,54]. The peaks located at around 286 eV and 287.5 eV appeared in all the samples due to the presence of C-O or C-N and C=O bond [53,54]. In Figure 5.1.9 (b) and (c), the peak at 288.7 eV accounts for the chemical bonding of O-C-O [53,54]. It is obvious that the intensities of C-O, C=O and O-C-O bonds increased when APDMES precursor was used together with TMS.

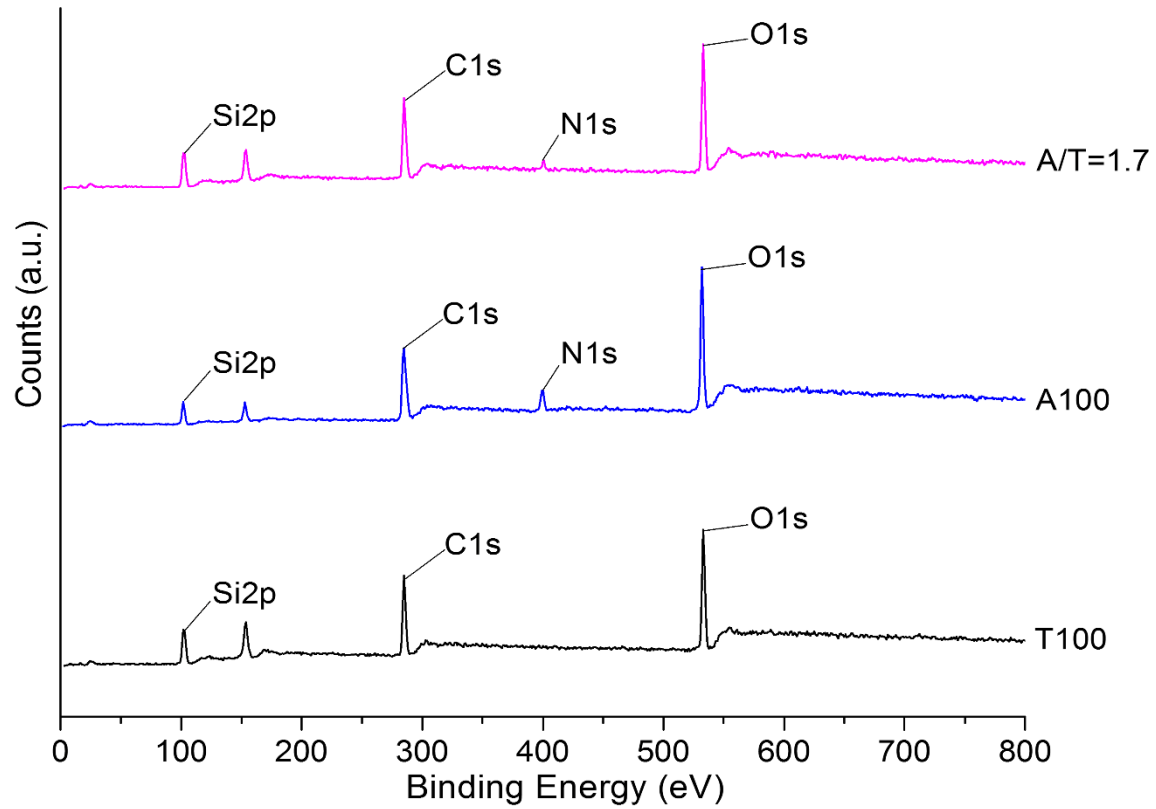


Figure 5.1.8. Surface elemental composition of the selected samples.

Table 5.1.2. Thickness and RMS roughness of each sample.

Sample	Thickness (nm)	RMS roughness (nm)
A	207	30.45
T	385	111.32
A/T=1	422	118.92
A/T=1.4	451	134.21
A/T=1.7	470	137.62
A/T=2.4	494	105.32

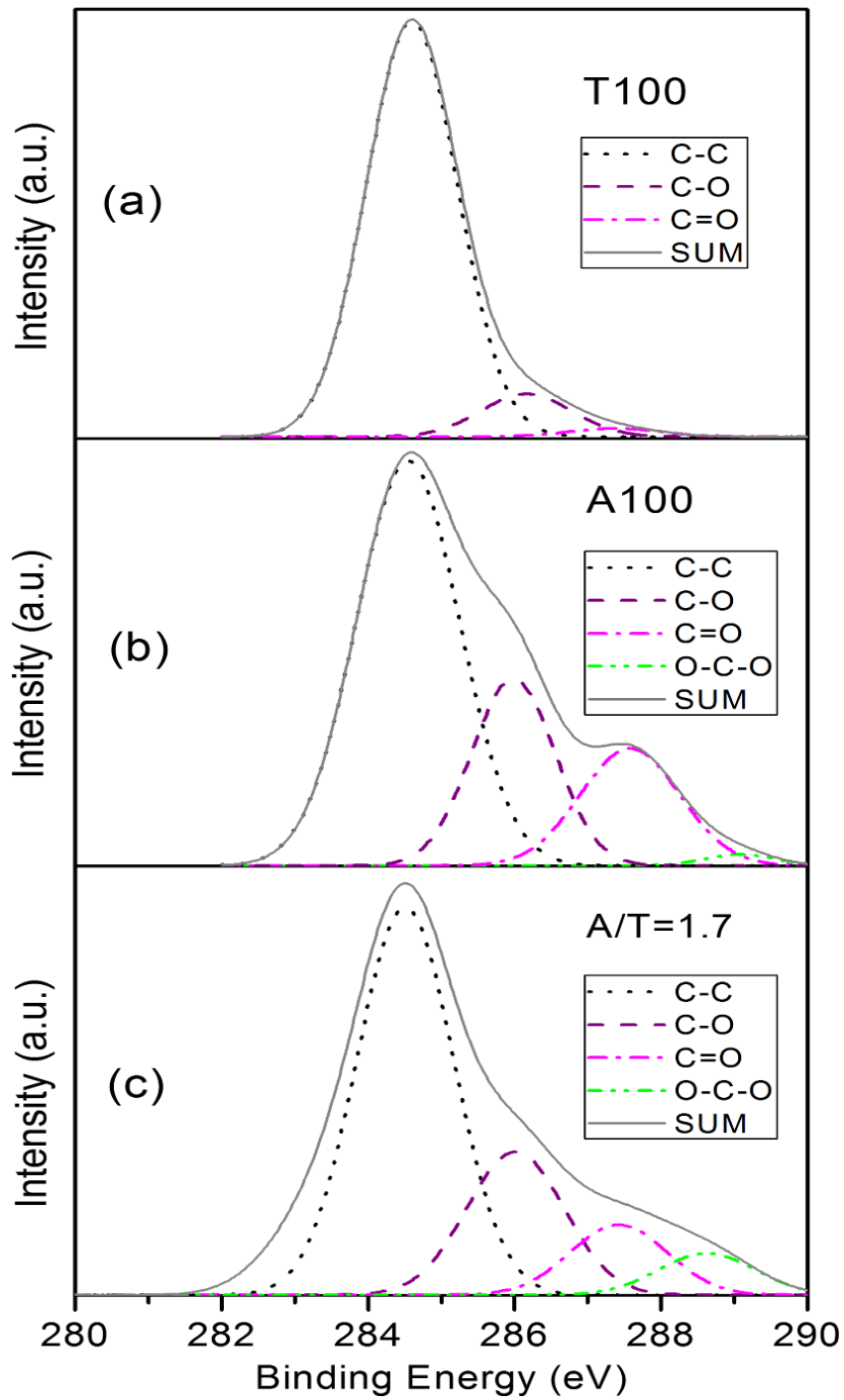


Figure 5.1.9. Deconvolution of C1s spectra of the selected coated samples.

The transparency of the sample before and after coating was examined by the UV-visible spectroscopy in the visible range (from 390 nm to 700 nm). Generally, the hydrophobicity and the transmittance have an inverse relationship because of their dependence on the surface thickness and roughness. As the coating thickness and roughness increase, the hydrophobicity increases but transparency decreases [55]. The UV-vis transmission spectra of the prepared samples are presented in Figure 5.1.10 (a). For information, the photographic image of the side and top view of the sample (A/T=1.7) is given in Figure 5.1.10 (b). The transmittance of the bare glass itself is

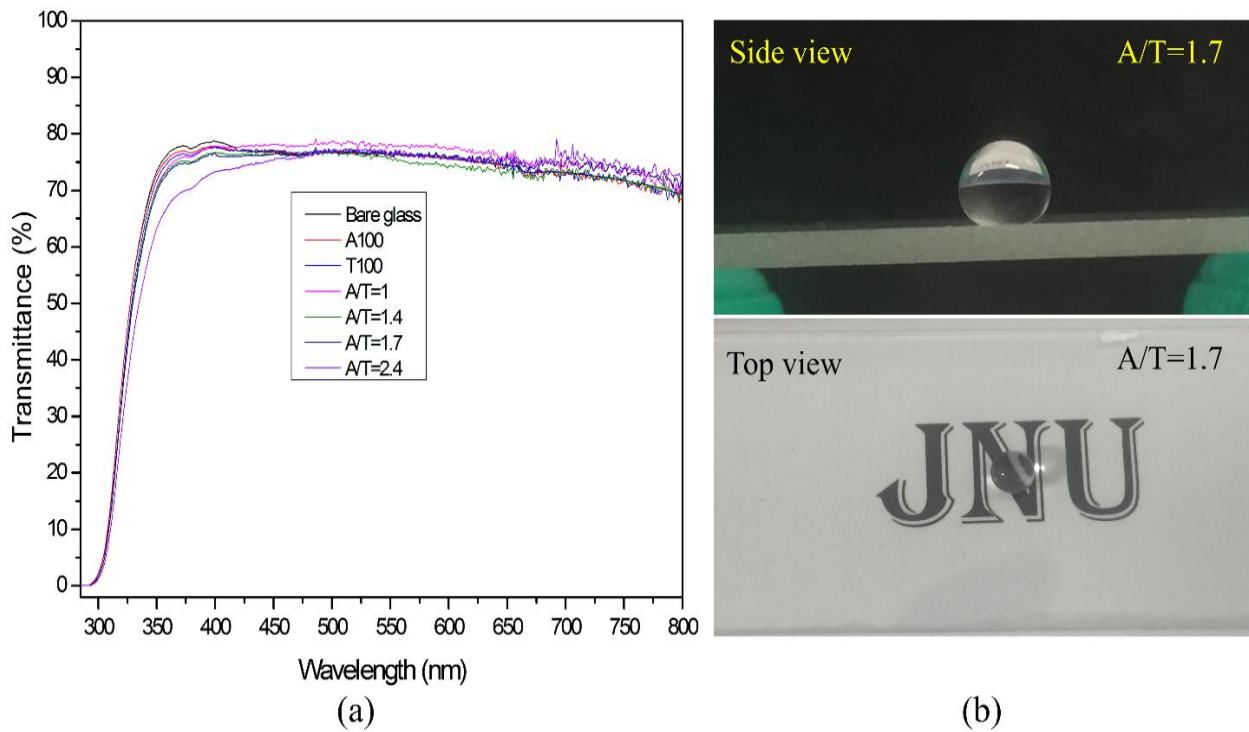


Figure 5.1.10. (a) UV-visible spectra of the samples prepared at different A/T ratios, and (b) top and side view of the selected sample (A/T=1.7).

less than 80% in the visible region. From Figure 5.1.10 (a), it can be seen that the coating film did not significantly decrease the transparency of the glass. Only the sample prepared at A/T=2.4

slightly decreased the visibility in the range of 390 to 450 nm. The WCA of this sample (A/T=2.4) was not good either, compared to the samples prepared at other A/T ratios (Figure 5.1.3).

5.3.5. Scratch test

The mechanical strength of the coating was analyzed using a home-made scratch tester after annealing the samples at 300°C for 1 h. The conditions for the scratch tests are summarized in Table 5.1.3, and the test results are shown in Figure 5.1.11. The weight of the needle and

Table 5.1.3. Scratch test results for each sample.

Sample	Applied force (dyne)
A100	16671
T100	3432
A/T=1	4216
A/T=1.4	5099
A/T=1.7	6080
A/T=2.4	7649

holder was 3432 dyne, and thus the minimum force applied to the sample was 3432 dyne. The sample prepared with TMS alone (T100) did not sustain the minimum force. For the other samples, the force gradually increased until the breakdown force was reached. Figure 5.1.12 shows the scratch test images taken by the digital microscope. As can be seen, increasing the A/T ratio resulted in good mechanical strength. This result is because APDMES forms Si-O-Si bridge and H-bonding through the interaction with the silanol group of glass, as discussed above. Even though the A/T=2.4 sample exhibited better mechanical strength than those prepared at lower A/T ratios,

the best condition to satisfy both superhydrophobicity and strength is $A/T=1.7$, considering all the other factors discussed above.

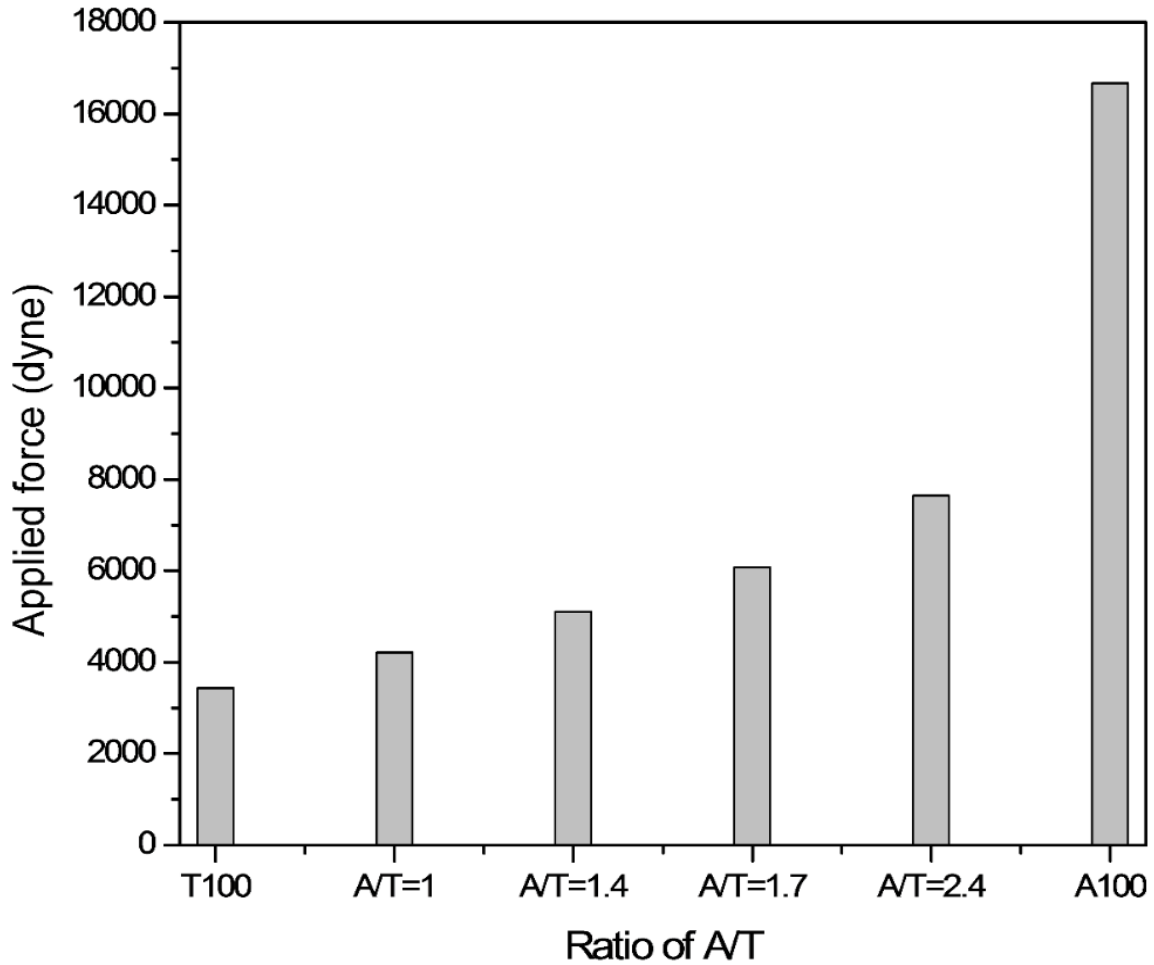


Figure 5.1.11. Breakdown forces of the samples obtained by the scratch tests.

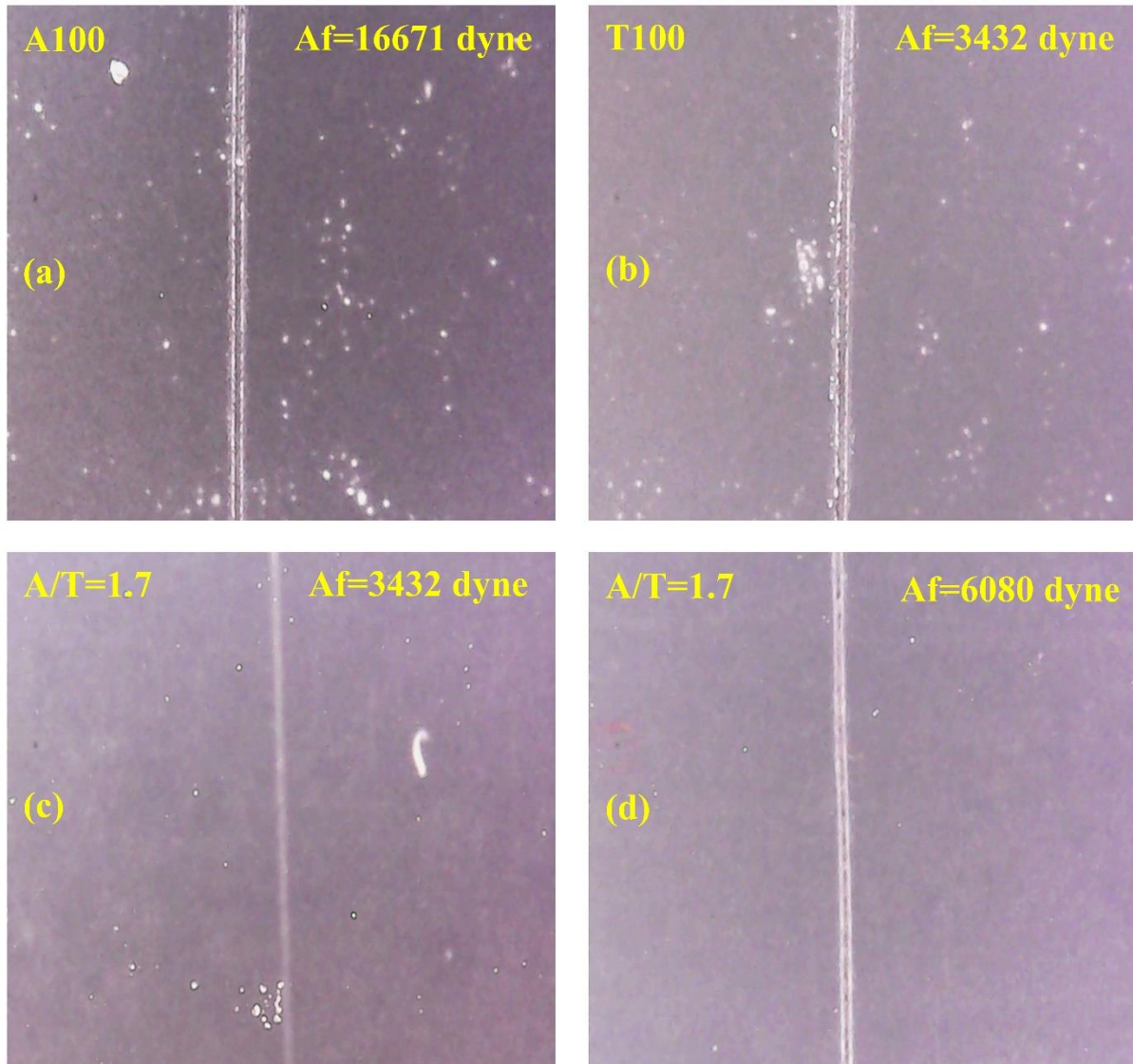


Figure 5.1.12. Microscope images of the selected samples.

5.4. Conclusions

A simple and convenient plasma-based method to produce stable superhydrophobic coating was demonstrated. The precursors TMS and APDMES were successfully copolymerized to form thin superhydrophobic film on the glass surface by the atmospheric-pressure plasma jet. The poor mechanical strength, which is a problem of TMS-alone coating, could be improved to some extent by using APDMES as the second precursor. Under an appropriate condition for the coating, namely, the treatment time of 40 s, the applied voltage of 7 kV, the A/T ratio of 1.7 and the total gas flow rate of 5 L/min, maximum WCA achieved was 163°. The superhydrophobicity resulted mainly from the surface roughness generated by the plasma jet, which was confirmed by the FE-SEM and the 3D nano-profiler. The aging and annealing test exhibited that the coating film prepared by the plasma jet had good stability, and as well, the UV-vis spectroscopic analysis showed that there was no significant loss in the transparency in the visible region. It is believed that the non-thermal atmospheric-pressure plasma jet could be one of the candidates that can be used to prepare superhydrophobic surfaces on various solid materials.

5.5. References

- [1] E.M. Liston, L. Martinu, M.R. Wertheimer, Plasma surface modification of polymers for improved adhesion: A critical review, *J. Adhes. Sci. Technol.* 7 (1993) 1091–1127.
- [2] P. Hamerli, T. Weigel, T. Groth, D. Paul, Surface properties of and cell adhesion onto allylamine-plasma-coated polyethylenterephtalat membranes, *Biomaterials.* 24 (2003) 3989–3999.
- [3] P.K. Chu, J.Y. Chen, L.P. Wang, N. Huang, Plasma-surface modification of biomaterials, *Mater. Sci. Eng. R Reports.* 36 (2002) 143–206.
- [4] B.D. Ratner, Surface modification of polymers: chemical, biological and surface analytical challenges, *Biosens. Bioelectron.* 10 (1995) 797–804.
- [5] J. Ryu, T. Wakida, T. Takagishi, Effect of Corona Discharge on the Surface of Wool and Its Application to Printing, *Text. Res. J.* 61 (1991) 595–601.
- [6] A. Pavlath, K.S. Lee, Glow Discharge Induced Graft Polymerization of Nonvolatile Monomers on Wool, *J. Macromol. Sci. Part A - Chem.* 10 (1976) 619–630.
- [7] W.J. Thorsen, R.Y. Kodani, A Corona Discharge Method of Producing Shrink-Resistant Wool and Mohair, *Text. Res. J.* 36 (1966) 651–661.
- [8] W.J. Thorsen, Improvement of Cotton Spinnability, Strength, and Abrasion Resistance by Corona Treatment, *Text. Res. J.* 41 (1971) 455–458.
- [9] T.L. Ward, R.R. Benerito, Modification of Cotton by Radiofrequency Plasma of Ammonia, *Text. Res. J.* 52 (1982) 256–263.
- [10] S.S. Latthe, C. Terashima, K. Nakata, M. Sakai, A. Fujishima, Development of sol–gel processed semi-transparent and self-cleaning superhydrophobic coatings, *J. Mater. Chem. A.* 2 (2014) 5548–5553.
- [11] T. Kamegawa, Y. Shimizu, H. Yamashita, Superhydrophobic surfaces with photocatalytic self-cleaning properties by nanocomposite coating of TiO₂ and polytetrafluoroethylene, *Adv. Mater.* 24 (2012) 3697–3700.
- [12] Y. Liu, J. Chen, D. Guo, M. Cao, L. Jiang, Floatable, Self-Cleaning, and Carbon-Black-Based Superhydrophobic Gauze for the Solar Evaporation Enhancement at the Air–Water Interface, *ACS Appl. Mater. Interfaces.* 7 (2015) 13645–13652.
- [13] C.-H. Xue, Y.-R. Li, P. Zhang, J.-Z. Ma, S.-T. Jia, Washable and Wear-Resistant Superhydrophobic Surfaces with Self-Cleaning Property by Chemical Etching of Fibers and

- Hydrophobization, *ACS Appl. Mater. Interfaces*. 6 (2014) 10153–10161.
- [14] D. Quéré, Non-sticking drops, *Reports Prog. Phys.* 68 (2005) 2495.
- [15] W. Barthlott, C. Neinhuis, Purity of the sacred lotus, or escape from contamination in biological surfaces, *Planta*. 202 (1997) 1–8.
- [16] A. Lafuma, D. Quéré, Superhydrophobic states, *Nat. Mater.* 2 (2003) 457.
- [17] H. Saito, K. Takai, G. Yamauchi, A study on ice adhesiveness to water-repellent coating, *Mater. Sci. Res. Int.* 3 (1997) 185–189.
- [18] T. Kako, A. Nakajima, H. Irie, Z. Kato, K. Uematsu, T. Watanabe, K. Hashimoto, Adhesion and sliding of wet snow on a super-hydrophobic surface with hydrophilic channels, *J. Mater. Sci.* 39 (2004) 547–555.
- [19] J. Chapman, F. Regan, Nanofunctionalized superhydrophobic antifouling coatings for environmental sensor applications-advancing deployment with answers from nature, *Adv. Eng. Mater.* 14 (2012) B175–B184.
- [20] C.-H. Xue, X.-J. Guo, J.-Z. Ma, S.-T. Jia, Fabrication of Robust and Antifouling Superhydrophobic Surfaces via Surface-Initiated Atom Transfer Radical Polymerization, *ACS Appl. Mater. Interfaces*. 7 (2015) 8251–8259.
- [21] A. Scardino, R. De Nys, O. Ison, W. O’Connor, P. Steinberg, Microtopography and antifouling properties of the shell surface of the bivalve molluscs *Mytilus galloprovincialis* and *Pinctada imbricata*, in: *Biofouling*. 19 (2003) 221–230.
- [22] M.P. Schultz, C.J. Kavanagh, G.W. Swain, Hydrodynamic forces on barnacles: Implications on detachment from fouling-release surfaces, *Biofouling*. 13 (1999) 323–335.
- [23] L. Wang, Q. Gong, S. Zhan, L. Jiang, Y. Zheng, Robust Anti-Icing Performance of a Flexible Superhydrophobic Surface, *Adv. Mater.* 28 (2016) 7729–7735.
- [24] X. Zhan, Y. Yan, Q. Zhang, F. Chen, A novel superhydrophobic hybrid nanocomposite material prepared by surface-initiated AGET ATRP and its anti-icing properties, *J. Mater. Chem. A*. 2 (2014) 9390–9399.
- [25] K. Liu, M. Zhang, J. Zhai, J. Wang, L. Jiang, Bioinspired construction of Mg-Li alloys surfaces with stable superhydrophobicity and improved corrosion resistance, *Appl. Phys. Lett.* 92 (2008) 183103.
- [26] N. Wang, D. Xiong, Y. Deng, Y. Shi, K. Wang, Mechanically robust superhydrophobic steel surface with anti-icing, UV-durability, and corrosion resistance properties, *ACS Appl.*

- Mater. Interfaces. 7 (2015) 6260–6272.
- [27] P. Wang, D. Zhang, R. Qiu, Y. Wan, J. Wu, Green approach to fabrication of a superhydrophobic film on copper and the consequent corrosion resistance, *Corros. Sci.* 80 (2014) 366–373.
- [28] D. Yu, J. Tian, J. Dai, X. Wang, Corrosion resistance of three-layer superhydrophobic composite coating on carbon steel in seawater, *Electrochim. Acta.* 97 (2013) 409–419.
- [29] S. Shibuichi, T. Onda, N. Satoh, K. Tsujii, Super water-repellent surfaces resulting from fractal structure, *J. Phys. Chem.* 100 (1996) 19512–19517.
- [30] I.P. Parkin, R.G. Palgrave, Self-cleaning coatings, *J. Mater. Chem.* 15 (2005) 1689–1695.
- [31] L. Feng, T. Sun, L.I.N. Feng, Bioinspired Surfaces with Special Wettability Bioinspired Surfaces with Special Wettability, *Acc. Chem. Res.* 38 (2005) 644–652.
- [32] X. Deng, L. Mammen, H.J. Butt, D. Vollmer, Candle soot as a template for a transparent robust superamphiphobic coating, *Science* (80-.). 335 (2012) 67–70.
- [33] H. Zhou, H. Wang, H. Niu, A. Gestos, T. Lin, Robust, self-healing superamphiphobic fabrics prepared by two-step coating of fluoro-containing polymer, fluoroalkyl silane, and modified silica nanoparticles, *Adv. Funct. Mater.* 23 (2013) 1664–1670.
- [34] H.Y. Sun, C.Y. Fang, T.J. Lin, Y.C. Chen, C.Y. Lin, H.Y. Ho, M.H.C. Chen, J. Yu, D.J. Lee, C.H. Chang, H.Y. Chen, Thiol-Reactive Parylenes as a Robust Coating for Biomedical Materials, *Adv. Mater. Interfaces.* 1 (2014) 1400093.
- [35] W. Zeng, J. Chen, H. Yang, L. Deng, G. Liao, Z. Xu, Robust coating with superhydrophobic and self-cleaning properties in either air or oil based on natural zeolite, *Surf. Coatings Technol.* 309 (2017) 1045–1051.
- [36] H. Zhou, H. Wang, H. Niu, A. Gestos, X. Wang, T. Lin, Fluoroalkyl silane modified silicone rubber/nanoparticle composite: A super durable, robust superhydrophobic fabric coating, *Adv. Mater.* 24 (2012) 2409–2412.
- [37] Y. Lu, S. Sathasivam, J. Song, C.R. Crick, C.J. Carmalt, I.P. Parkin, Robust self-cleaning surfaces that function when exposed to either air or oil, *Science* (80-.). 347 (2015) 1132–1135.
- [38] J. Zeng, B. Wang, Y. Zhang, H. Zhu, Z. Guo, Strong Amphiphobic Porous Films with Oily-self-cleaning Property beyond Nature, *Chem. Lett.* 43 (2014) 1566–1568.
- [39] K. Tu, X. Wang, L. Kong, H. Chang, J. Liu, Fabrication of robust, damage-tolerant

- superhydrophobic coatings on naturally micro-grooved wood surfaces, *RSC Adv.* 6 (2015) 701–707.
- [40] A.C. Miller, M.T. Knowlton, J.C. Berg, The use of UNIFAC for the estimation of adhesion enhancement between polymers and mineral surfaces treated with silane coupling agents, *J. Adhes. Sci. Technol.* 14 (2000) 1471–1484.
- [41] M.J. Shenton, G.C. Stevens, Surface modification of polymer surfaces: Atmospheric plasma versus vacuum plasma treatments, *J. Phys. D. Appl. Phys.* 34 (2001) 2761–2768.
- [42] M.R. Wertheimer, A.C. Fozza, A. Holländer, Industrial processing of polymers by low-pressure plasmas: the role of VUV radiation, *Nucl. Instruments Methods Phys. Res. Sect. B Beam Interact. with Mater. Atoms.* 151 (1999) 65–75.
- [43] L. Kilpi, O.M.E. Ylivaara, A. Vaajoki, J. Malm, S. Sintonen, M. Tuominen, R.L. Puurunen, H. Ronkainen, Microscratch testing method for systematic evaluation of the adhesion of atomic layer deposited thin films on silicon, *J. Vac. Sci. Technol. A Vacuum, Surfaces, Film.* 34 (2016) 01A124.
- [44] B.A. McCool, W.J. DeSisto, Amino-functionalized silica membranes for enhanced carbon dioxide permeation, *Adv. Funct. Mater.* 15 (2005) 1635–1640.
- [45] S.M. Kanan, W.T.Y. Tze, C.P. Tripp, Method to double the surface concentration and control the orientation of adsorbed (3-aminopropyl)dimethylethoxysilane on silica powders and glass slides, *Langmuir.* 18 (2002) 6623–6627.
- [46] Q.H. Trinh, S.B. Lee, Y.S. Mok, Hydrophobic Coating of Silicate Phosphor Powder Using Atmospheric Pressure Dielectric Barrier Discharge Plasma, *Am. Inst. Chem. Eng.* 60 (2014) 829–838.
- [47] F. Fanelli, S. Lovascio, R. D’Agostino, F. Arefi-Khonsari, F. Fracassi, Ar/HMDSO/O₂ fed atmospheric pressure DBDs: Thin film deposition and GC-MS investigation of by-products, *Plasma Process. Polym.* 7 (2010) 535–543.
- [48] J.H. Yim, V. Rodriguez-Santiago, A.A. Williams, T. Gougousi, D.D. Pappas, J.K. Hirvonen, Atmospheric pressure plasma enhanced chemical vapor deposition of hydrophobic coatings using fluorine-based liquid precursors, *Surf. Coatings Technol.* 234 (2013) 21–32.
- [49] F. Alba-Elías, J. Ordieres-Meré, A. González-Marcos, Deposition of thin-films on EPDM substrate with a plasma-polymerized coating, *Surf. Coatings Technol.* 206 (2011) 234–242.

- [50] J. Schäfer, R. Foest, A. Quade, A. Ohl, J. Meichsner, K.D. Weltmann, Carbon-free SiO_x films deposited from octamethylcyclotetrasiloxane (OMCTS) by an atmospheric pressure plasma jet (APPJ), *Eur. Phys. J. D.* 54 (2009) 211–217.
- [51] F. Rombaldoni, R. Mossotti, A. Montarsolo, M.B. Songia, R. Innocenti, G. Mazzuchetti, Thin film deposition by PECVD using HMDSO-O₂-Ar gas mixture on knitted wool fabrics in order to improve pilling resistance, *Fibers Polym.* 9 (2008) 566–573.
- [52] M. Gueye, T. Gries, C. Noël, S. Migot-Choux, S. Bulou, E. Lecoq, P. Choquet, K. Kutasi, T. Belmonte, Interaction of (3-Aminopropyl)triethoxysilane with Pulsed Ar–O₂ Afterglow: Application to Nanoparticles Synthesis, *Plasma Chem. Plasma Process.* 36 (2016) 1031–1050.
- [53] R. Múgica-Vidal, F. Alba-Elías, E. Sainz-García, J. Ordieres-Meré, Atmospheric plasma-polymerization of hydrophobic and wear-resistant coatings on glass substrates, *Surf. Coatings Technol.* 259 (2014) 374–385.
- [54] C.-W. Kan, C.-H. Kwong, S.-P. Ng, Atmospheric Pressure Plasma Surface Treatment of Rayon Flock Synthetic Leather with Tetramethylsilane, *Appl. Sci.* 6 (2016) 59.
- [55] Y. Li, J. Zhang, S. Zhu, H. Dong, F. Jia, Z. Wang, Z. Sun, L. Zhang, Y. Li, H. Li, W. Xu, B. Yang, Biomimetic surfaces for high-performance optics, *Adv. Mater.* 21 (2009) 4731–4734.

CHAPTER-6

Preparation of carbon materials for the supercapacitor using non-thermal atmospheric-pressure plasma jet

Highlights

- NTP is used to prepare graphitic carbon materials from n-heptane.
- Coating layer depended on the flow rate, applied voltage, treatment time.
- The prepared graphene confirmed by the Raman shift.
- Graphene layer shows uniform thickness.

6.1. Introduction

The civilization progress is directly related to the development in science and technology. Without energy storage devices we cannot imagine using electronic portable devices such as laptops, cellular phones, or iPods in our daily life. Electric vehicles, airplanes, and many other inventions which make our life easier and more comfortable cannot be run without energy storage devices. This world stands on energy which mainly coming from fossil fuel. Electrochemical devices are good options to store energy play a vital role in overcoming fossil fuel exhaustion [1–4]. There are several electrochemical energy storage devices, supercapacitor is one of them has attracted significant interest in both academia and industry during the past several decades owing to their superior power density, fast charge/discharge rate and long cycle life [5–9]. Supercapacitors and rechargeable batteries are similar systems with positive electrodes, negative electrodes, and separators that are soaked with electrolytes [1–4]. Supercapacitors can be considered as the intermediate between the conventional dielectric capacitor and the battery. Nowadays, supercapacitors have been utilized in many applications such as consumer electronics, military and aerospace, transportation, power backup, grid balancing, enhancing, and/or replacing batteries in these applications [10–15]. Supercapacitors can also be used along with rechargeable batteries to provide the additional power essential in many applications, such as electrical vehicles (EVs) and hybrid electric vehicles (HEVs). These devices can capture and store energy from regenerative braking and supplying vehicle acceleration power which can protect rechargeable batteries from high-frequency rapid discharge/charge processes.

Ceramic has been widely used to construct capacitors for radio receivers since 1930. These very early capacitors were mainly utilized as primary circuit elements in holding microfarad to picofarad charges of direct current or to filter the frequencies for alternating current circuits. The

earliest supercapacitors (1957), electrochemical double layer capacitors (EDLCs), were invented as an electrolytic capacitor for low voltage operation. For EDLCs, the energy storage is based on the adsorption of electrolyte ions on the large specific surface area of electrically conductive porous electrodes. Typically, carbon materials and their derivatives are used in EDLCs, including carbon nanotubes (CNTs), activated carbon, porous carbon, and graphene. For increasing the capacitance and energy density of supercapacitors, some electrochemically active materials have been explored as electrode materials of pseudocapacitors. Energy storage in pseudocapacitance comes from reversible surface faraday redox reactions occurring at the interface between electrolytes and electroactive materials.

If supercapacitors are able to meet all the requirements for next-generation electronic devices, everything will be simple and perfect. Regrettably, the traditional supercapacitor has a rigid bulky or planar structure and which has a little possibility of achieving future applications. To accomplish future goal, supercapacitor should be weaveable, or miniature, or smart, or large-scale [16–22]. To overcome the limitations, various novel devices of supercapacitors need to be designed such as lighter, thinner, smart or even transparent supercapacitors to achieve special properties for increasingly multifunctional consumer electronics.

For electrochemical applications, carbon materials have drowned the attention of researchers, especially for fabricating of energy storage devices due to their good conductivity, well polarizability, and more environmentally friendly. Moreover, these carbon materials have got much attention while applied as electrode material because of their accessibility, easy to be processed and relatively low cost. Based on these issues, this study is focused on the development of graphitic carbon material for supercapacitor electrode from hydrocarbon-rich precursors. This material can be produced using a relatively simple method of plasma deposition and pyrolysis. For

this study, n-heptane was used as a source of carbon. Argon (Ar) gas was used to form plasma using kHz power source and nitrogen used as a shielding gas to reduce oxidation for the plasma coatings.

6.2. Experimental methodology

6.2.1. Deposition of plasma polymer coatings

This study has shown the processing of n-heptane using dielectric barrier discharge (DBD) plasma. Figure 6.1.1 shows atmospheric-pressure dielectric barrier discharge (AP-DBD) plasma configuration which was used in this experiment. The reactor was made of by copper sheet and ceramic. Two copper sheets with 80 mm × 30 mm dimension each were used as electrodes. Ceramic plate was used as a dielectric barrier and the gap between plate to plate was 5 mm. The plasma reactor was operated with a high-voltage alternating current (AC) power source (Korea Switching Co., Korea) whose frequency output was set to 11.5 kHz. Ar was used as a discharge gas at 1.6 L/min and applied voltage was 8 kV. Nickel foam with 75 mm × 25 mm × 1.5 mm dimension was used to deposit hydrocarbon. Normal n-heptane was used as a source of hydrocarbon at the rate of 2000 ppm controlled by the mass flow controller. It was the optimal ppm level for this case. The treatment time was varied from 5 min to 120 min. Figure 6.1.2 shows the photographic images of the sample prepared by the conventional planar DBD configuration after pyrolysis. The pyrolysis process was done under nitrogen environment at 800 °C for 6 hours. The plasma treatment time of the sample was 120 min.

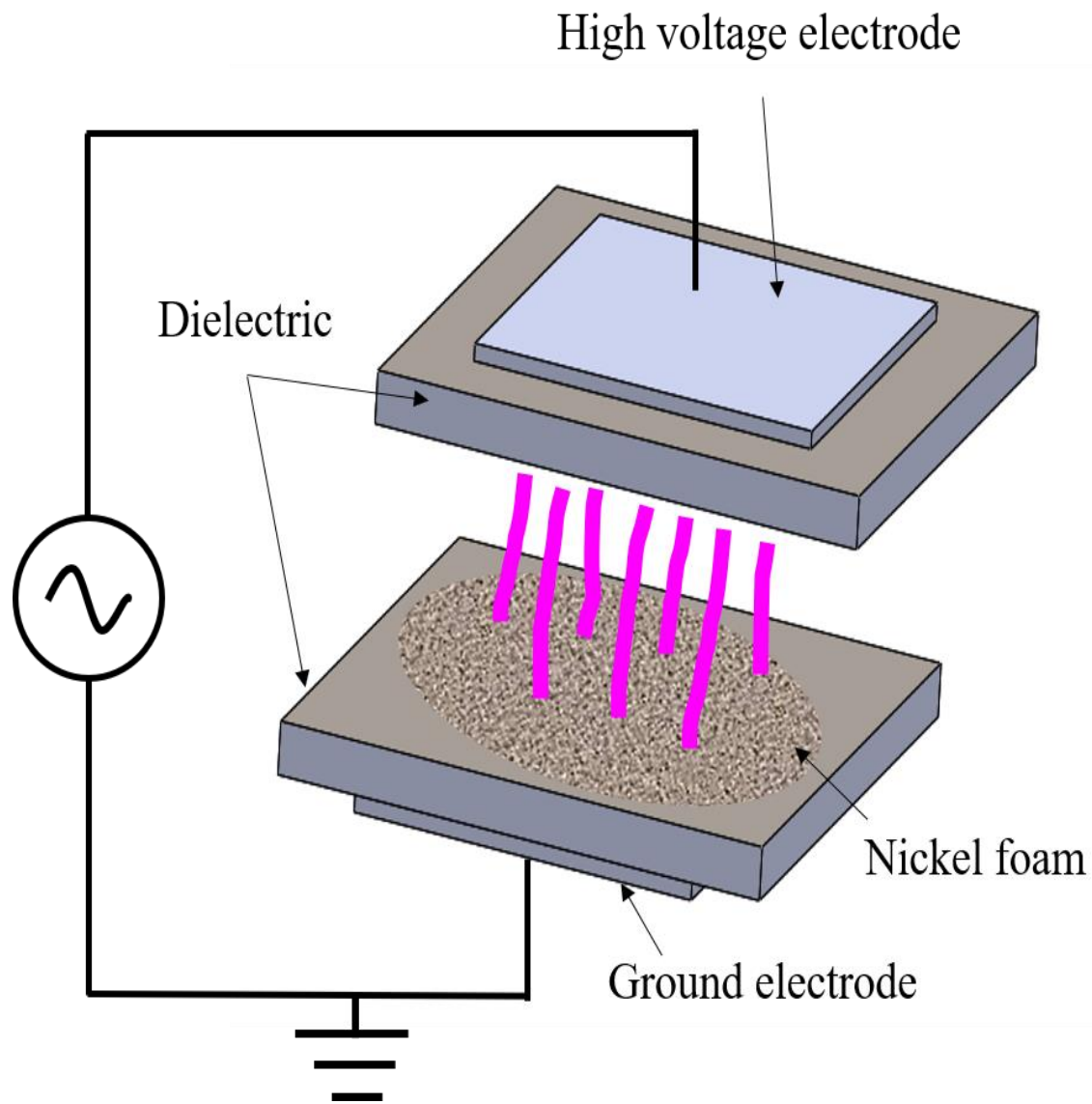


Figure 6.1.1. Conventional planar DBD configuration.

6.2.2. Characterizations

The surface morphology and roughness of the coatings were analyzed by a field emission scanning electron microscopy (FESEM, MIRA3, TESCAN, USA) at an operating voltage of 15 kV. The Raman spectroscopy was used to reveal what kind of carbon was formed over the surface.

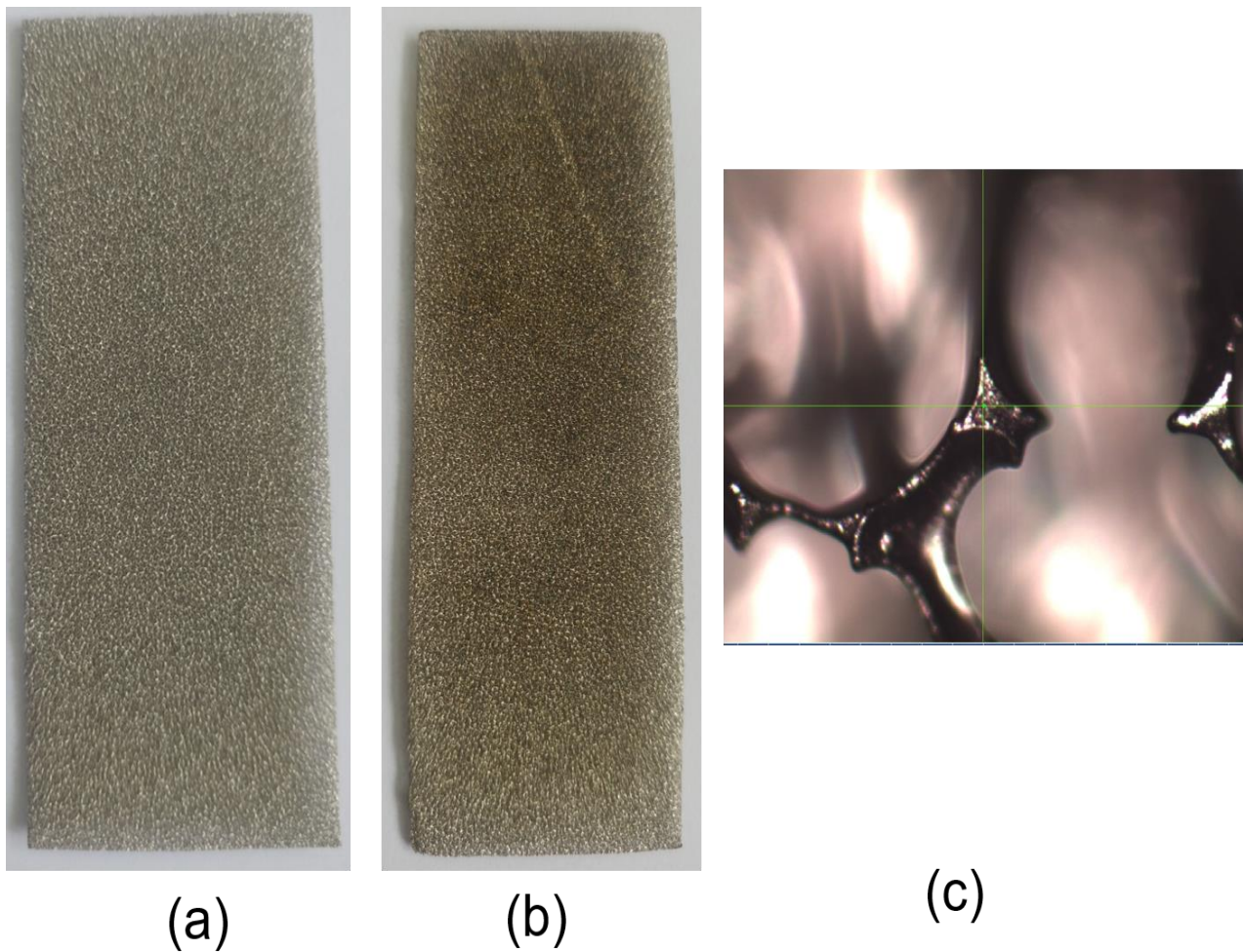


Figure 6.1.2. Photographic images of (a) bare nickel foam (b) after coating and thermal pyrolysis (carbon/nickel foam) and (c) microscopic image of carbon/nickel foam at 100X magnification from Raman spectroscopy

6.3. Results and Discussion

5.3.1. Surface morphology and roughness

FE-SEM analyses was conducted to investigate the surface morphology, and the coating thickness. Figure 6.1.3 shows results of the nickel foam sample prepared by the conventional rectangular planar DBD configuration. From the figure, it can be seen (Figure 6.1.4 (b)) that the coating adhesion to the nickel foam surface is poor and it is due to no chemical bonding between nickel foam and deposited carbon material. The polymer deposited on the surfaces is not well attached to the surface of nickel foam, and a lot of cracks are also present there. The thickness of the coating shows in Figure 6.1.3 (c).

6.3.2. Raman shift

Figure 6.1.4 shows the Raman shift of graphene prepared by the plasma deposition and pyrolysis process. Raman spectrum of carbon nanomaterials is characterized by two main shifts ranged from 1000 to 1700 cm^{-1} . The first peak at 1604 cm^{-1} is a graphene mode (G band) associated to the first order Raman scattering of the E_{2g} phonon at the Brillouin zone center of SP^2 carbon atoms, which reflect the in-plane stretching of graphene lattice. The second peak at 1345 cm^{-1} which has a small intensity for raw graphite attributing to diamondoid mode (D band) arising from the breathing mode of k-point phonons of A_{1g} symmetry, which originating from defects, disordered in hexagonal graphitic layers and amorphous carbon species. The intensity ratio of D and G bands (I_D/I_G) is used to determine the quality of graphitization or defective disorders on the crystalline graphite.

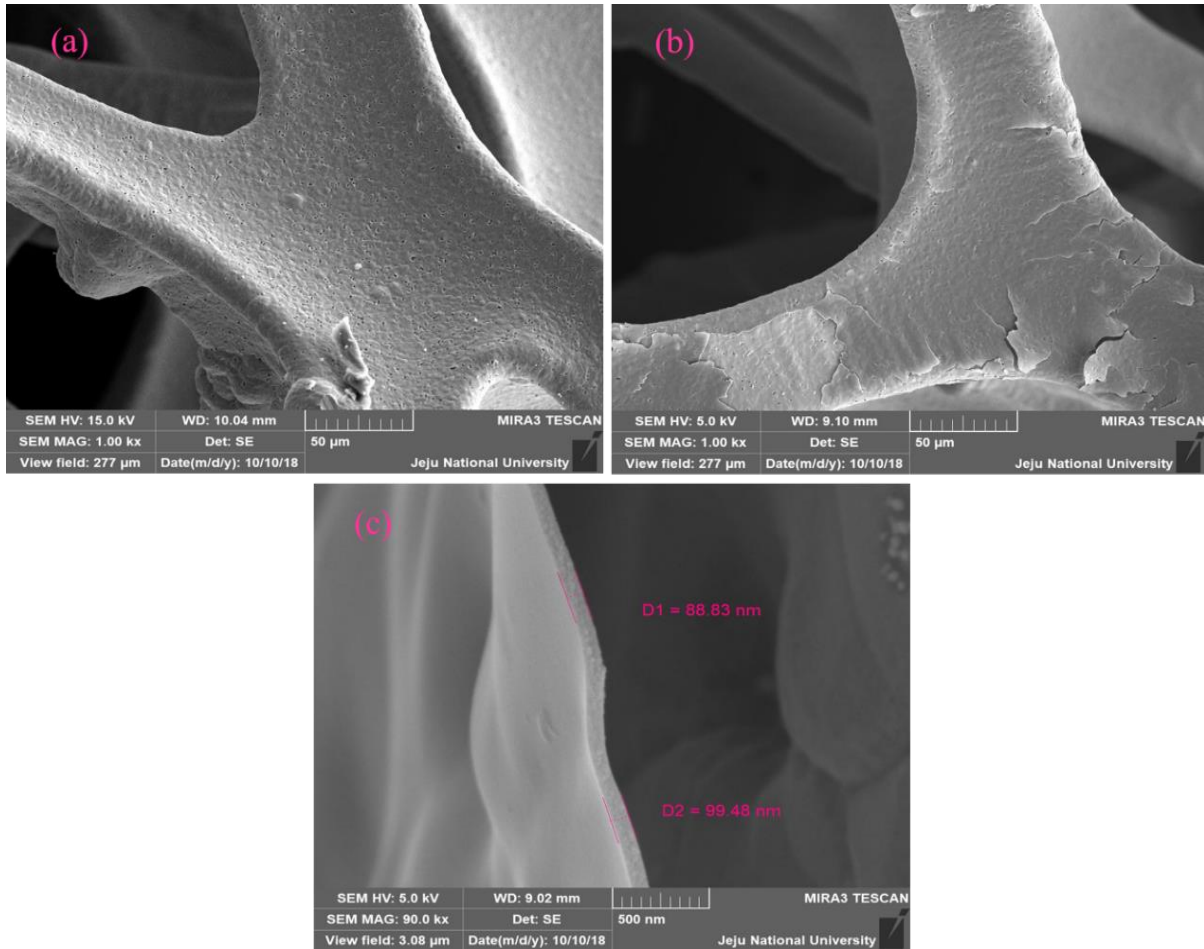


Figure 6.1.3. FE-SEM image of (a) bare nickel foam, (b) 120 min coated nickel foam, and (c) thickness of the coated thin film.

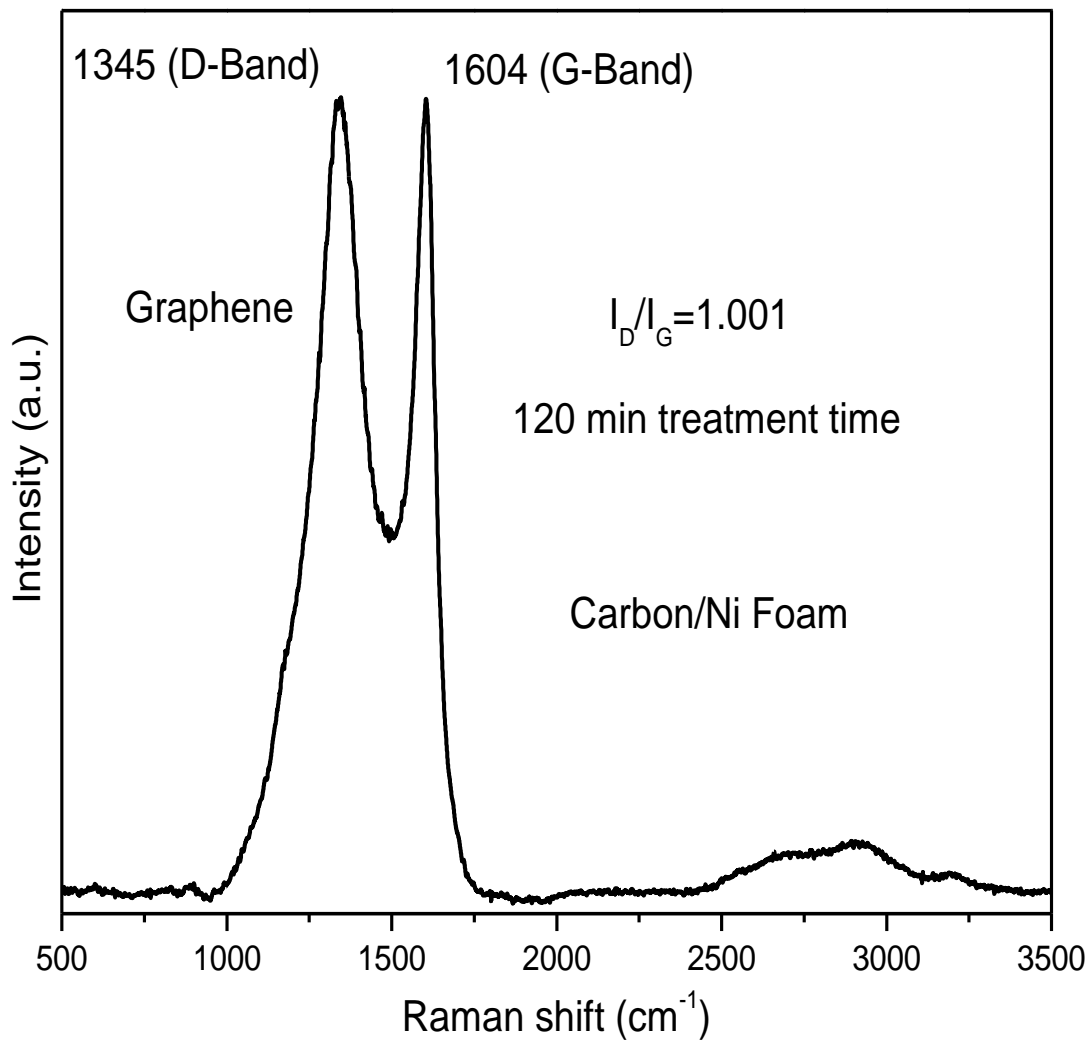


Figure 6.1.4. Raman spectra result of coated sample. [Treatment time 120 min, n-heptane concentration 2000 pmm and Ar gas flow rate 1.6 L/min]

6.4. Conclusions

The purpose of this work was to prepare carbon material using plasma deposition which was an easy and cost-effective method. Recent research and development clearly indicate that high-performance supercapacitors can be prepared by using electrodes based on carbon nanotubes, graphene sheets, and graphene-carbon nanotube. We have demonstrated how to produce graphene with less effort. Normal n-heptane used as a source of carbon and thermal pyrolysis helped to convert graphene-like carbon from plasma deposited hydrocarbon. Raman shift was used to identify the nature of carbon after pyrolysis. This graphitic carbon can be a good candidate to make supercapacitors.

6.5. References

- [1] Zhong C, Deng Y, Hu W, et al. A review of electrolyte materials and compositions for electrochemical supercapacitors. *Chem. Soc. Rev.* 2015;44:7484–7539.
- [2] Tang W, Zhu Y, Hou Y, et al. Aqueous rechargeable lithium batteries as an energy storage system of superfast charging. *Energy Environ. Sci.* 2013;6:2093–2104.
- [3] Wang F, Wu X, Li C, et al. Nanostructured positive electrode materials for post-lithium ion batteries. *Energy Environ. Sci.* 2016;9:3570–3611.
- [4] Li R, Lin Z, Ba X, et al. Integrated copper-nickel oxide mesoporous nanowire arrays for high energy density aqueous asymmetric supercapacitors. *Nanoscale Horizons.* 2016;1:150–155.
- [5] Augustyn V, Simon P, Dunn B. Pseudocapacitive oxide materials for high-rate electrochemical energy storage. *Energy Environ. Sci.* 2014;7:1597–1614.
- [6] Lukatskaya MR, Dunn B, Gogotsi Y. Multidimensional materials and device architectures for future hybrid energy storage. *Nat. Commun.* 2016;7:12647–12659.
- [7] Wang Y, Song Y, Xia Y. Electrochemical capacitors: Mechanism, materials, systems, characterization and applications. *Chem. Soc. Rev.* 2016;45:5925–5950.

- [8] Liu Y, Zhang B, Wang F, et al. Nanostructured intercalation compounds as cathode materials for supercapacitors. *Pure Appl. Chem.* 2014;86:593–609.
- [9] Bonaccorso F, Colombo L, Yu G, et al. Graphene, related two-dimensional crystals, and hybrid systems for energy conversion and storage. *Science* (80-.). 2015;347:1246501.
- [10] Kyeremateng NA, Brousse T, Pech D. Microsupercapacitors as miniaturized energy-storage components for on-chip electronics. *Nat. Nanotechnol.* 2017;12:7–15.
- [11] Yang S, Bachman RE, Feng X, et al. Use of organic precursors and graphenes in the controlled synthesis of carbon-containing nanomaterials for energy storage and conversion. *Acc. Chem. Res.* 2013;46:116–128.
- [12] Wu H Bin, Zhang G, Yu L, et al. One-dimensional metal oxide–carbon hybrid nanostructures for electrochemical energy storage. *Nanoscale Horizons.* 2016;1:27–40.
- [13] Qi D, Liu Y, Liu Z, et al. Design of Architectures and Materials in In-Plane Micro-supercapacitors: Current Status and Future Challenges. *Adv. Mater.* 2017;29.
- [14] Wang G, Zhang L, Zhang J. A review of electrode materials for electrochemical supercapacitors. *Chem. Soc. Rev.* 2012;41:797–828.
- [15] Yang Z, Ren J, Zhang Z, et al. Recent Advancement of Nanostructured Carbon for Energy Applications. *Chem. Rev.* 2015;115:5159–5223.
- [16] Naoi K, Ishimoto S, Miyamoto JI, et al. Second generation “nanohybrid supercapacitor”: Evolution of capacitive energy storage devices. *Energy Environ. Sci.* 2012;5:9363–9373.
- [17] Zhai T, Lu X, Wang F, et al. MnO₂ nanomaterials for flexible supercapacitors: Performance enhancement via intrinsic and extrinsic modification. *Nanoscale Horizons.* 2016;1:109–124.
- [18] Aravindan V, Gnanaraj J, Lee YS, et al. Insertion-type electrodes for nonaqueous Li-ion capacitors. *Chem. Rev.* 2014;114:11619–11635.
- [19] Chang Z, Yang Y, Li M, et al. Green energy storage chemistries based on neutral aqueous electrolytes. *J. Mater. Chem. A.* 2014;2:10739–10755.
- [20] SIMON P, GOGOTSI Y. Materials for electrochemical capacitors. *Nanosci. Technol.* 2008;7:845–854.
- [21] Wang F, Wang X, Chang Z, et al. Electrode materials with tailored facets for electrochemical energy storage. *Nanoscale Horizons.* 2016;1:272–289.
- [22] Dubal DP, Ayyad O, Ruiz V, et al. Hybrid energy storage: The merging of battery and

supercapacitor chemistries. Chem. Soc. Rev. 2015;44:1777–1790.

CHAPTER-7

Conclusion

This chapter describes the general conclusions of the overall thesis. This thesis mainly focuses on the improvement of thin film for various purpose such as making hydrophobic surface, preparation of carbon materials for energy storage devises. First, two chapters described the introduction of hydrophobicity and the energy storage devices and their fabrication processes.

Chapter three has described how the robust hydrophobic coating on glass surface by an atmospheric-pressure plasma jet was formed. In this study, the HMDSO was used to promote hydrophobicity and the APTES to promote robustness and durability owing to the presence of amines capable of promoting the adhesion of the coating layer. In terms of hydrophobicity and robustness of the coating, the applied voltage of 7 kV, treatment time of 60 s, and the H/A ratio of 3/1 were chosen as optimal condition. The WCA of 143° and reasonable mechanical strength were obtained under this condition.

Chapter four was the next work to improvement of mechanical strength of hydrophobic coating on glass surfaces by an atmospheric pressure plasma jet. The purpose of this work was to prepare a robust coating with good hydrophobic character as well as wear resistance by using non-thermal plasma jet with the mixture of two precursors. TMS was to promote hydrophobic character and APTES to increase the mechanical strength and durability owing to the presence of amines capable of promoting adhesion. The appropriate operating condition in terms of both hydrophobicity and mechanical strength was found to be the TMS/APTES ratio of 4.8, the applied voltage of 7.5 kV, and the treatment time of 300 s. At this condition, the WCA achieved was 139°.

Formation of plasma-polymerized superhydrophobic coating using an atmospheric-pressure plasma jet was studied in chapter five. In this chapter, a simple and convenient plasma-based method to produce stable superhydrophobic coating was demonstrated. The precursors TMS and APDMES were successfully copolymerized to form a thin superhydrophobic film on the glass surface by the atmospheric-pressure plasma jet. The poor mechanical strength, which is a problem of TMS-alone coating, could be improved to some extent by using APDMES as the second precursor. Under an appropriate condition for the coating, namely, the treatment time of 40 s, the applied voltage of 7 kV, the A/T ratio of 1.7 and the total gas flow rate of 5 L/min, maximum WCA achieved was 163°. And finally, chapter six has described about the preparation of carbon material that can be used to make anode for the supercapacitor which is also prepared by the NTP.

In this thesis, NTP has been used successfully for various purpose such as making hydrophobic surface, preparation of carbon materials for energy storage devises. The experimental results have confirmed the enormous potential of NTP as a useful tool for chemical deposition to make thin film over the various surfaces.

APPENDIX A: List of Publications

- 1 **Hossain MM**, Trinh QH, Nguyen DB, et al. Robust hydrophobic coating on glass surface by an atmospheric-pressure plasma jet for plasma-polymerisation of hexamethyldisiloxane conjugated with (3-aminopropyl) triethoxysilane. Surf. Eng. 2018;1–10.
- 2 **Hossain MM**, Trinh QH, Sudhakaran MSP, et al. Improvement of mechanical strength of hydrophobic coating on glass surfaces by an atmospheric pressure plasma jet. Surf. Coatings Technol. 2019;357:12–22.
- 3 Trinh QH, **Hossain MM**, Kim SH, et al. Tailoring the wettability of glass using a double-dielectric barrier discharge reactor. Heliyon. 2018;4.
- 4 M.S.P S, Sultana L, **Hossain MM**, et al. Iron–ceria spinel (FeCe₂O₄) catalyst for dry reforming of propane to inhibit carbon formation. J. Ind. Eng. Chem. 2018;61:142–151.
- 5 Sudhakaran MSP, Trinh HQ, **Hossain MM**, et al. Plasma Catalytic Removal of p-Xylene from Air Stream Using γ -Al₂O₃Supported Manganese Catalyst. Top. Catal. 2017;60:944–954.

List of submitted papers

1. **Md. Mokter Hossain**, Quang Hung Trinh, Duc Ba Nguyen, Sudhakaran M.S.P, Mok, Y.S., “Formation of plasma-polymerized superhydrophobic coating using an atmospheric-pressure plasma jet” – Thin Solid Films
2. Duc Ba Nguyen, Quang Hung Trinh, **Md. Mokter Hossain**, Won Gyu Lee, and Young Sun Mok, “Improvement of Electrical Measurement of a Dielectric Barrier Discharge Plasma Jet” - Surface Engineering
3. Quang Hung Trinh, Duc Ba Nguyen, **Md. Mokter Hossain**, and Young Sun Mok, “Deposition of superhydrophobic coatings on glass substrates from hexamethyldisiloxane using a kHz powered plasma jet”- Surf. Coatings Technol
4. Sudhakaran M.S.P, **Md. Mokter Hossain**, “Dry reforming of propane over γ -Al₂O₃ and nickel foam supported novel SrNiO₃ perovskite catalyst”- Catalysts

APPENDIX B: List of Conferences

1. **Md Mokter Hossain**, Quang Hung Trinh, Sudhakaran M.S.P., Lamia Sultana, Young Sun Mok, “Improving of Mechanical Strength of Hydrophobic Coating by Using Plasma Torch at Atmospheric Pressure” (November 8-10, 2017) **KSIEC 2017**, Busan, Republic of Korea (**ORAL -Excellent Presentation Award**).
2. **Mokter Md Hossain**, Duc Ba Nguyen, Sudhakaran M.S.P, Young Sun Mok, “Atmospheric pressure plasma polymerization to investigate robust hydrophobic coating on glass surface by using Tetramethylsilane conjugated with 3-Aminopropyl(diethoxy)methylsilane” (May 3-5, 2018) **KSIEC 2018**, Daegu, Republic of Korea (**ORAL -Excellent Presentation Award**).
3. **Md. Mokter Hossain**, Quang Hung Trinh, Duc Ba Nguyen, M.S.P. Sudhakaran, Young Sun Mok, “Investigation of robust superhydrophobic surface using atmospheric pressure plasma jet” (November 1-4, 2018) **KSIEC 2017**, Jeju-do, Republic of Korea (**ORAL -Excellent Presentation Award**).
4. **Md. Mokter Hossaina**, Duc Ba Nguyena, M.S.P. Sudhakarana, Bhattarai Roshan Mangala, and Young Sun Mok, “A study of seawater sterilization by ozone treatment for aquaculture” (November 1-4, 2018) **KSIEC 2017**, Jeju-do, Republic of Korea (**POSTER**).
5. **Md. Mokter Hossain**, Quang Hung Trinh, Duc Ba Nguyen, Sudhakaran M.S.P, Mok, Y.S., “Atmospheric pressure plasma polymerization to investigate robust hydrophobic coating on glass surface by using Tetramethylsilane conjugated with 3-Aminopropyl(diethoxy)methylsilane” (July 24-28, 2018) **ICMAP 2018**, Incheon, Republic of Korea (**POSTER**).
6. **Md. Mokter Hossain**, Quang Hung Trinh, Duc Ba Nguyen, Sudhakaran M.S.P, Young Sun Mok, “Investigation of robust hydrophobic coating on glass surface by an atmospheric pressure plasma jet for plasma-polymerization of Hexamethydisiloxane conjugated with (3-Aminopropyl)triethoxysilane” (March 28-30, 2018) **SurfCoat Korea 2018**, Incheon, Republic of Korea (**POSTER**).
7. **Md. Mokter Hossain**, Quang Hung Trinh, Sudhakaran M.S.P, Lamia Sultana, Young Sun Mok “Improving of mechanical strength of hydrophobic coating on glass surface by using plasma torch at atmospheric pressure” (September 11-15, 2017) **AEPSE 2017**, Jeju, Republic of Korea (**ORAL**).

8. **Md. Mokter Hossain**, Quang Hung Trinh, Sudhakaran M.S.P, Lamia Sultana, Y.S. Mok, “Improving of Mechanical Strength of Hydrophobic coating by using dielectric barrier discharge at atmospheric pressure” (May 10-12, 2017) **KSIEC 2017**, Gwangju, Republic of Korea (**POSTER**).
9. **Md Mokter Hossain**, Duc Ba Nguyen, M.S.P. Shdhakaran, Young Sun Mok, “Highly stable robust superhydrophobic coating deposited on glass substrate using atmospheric pressure plasma jet” (September 12-14, 2018) **KSCT 2018**, Gwangju, Republic of Korea (**POSTER**).
10. **Md Mokter Hossain**, Quang Hung Trinh, M.S.P. Shdhakaran, Lamia Sultana, Young Sun Mok, “Investigation of robust hydrophobic coating on glass surface by an atmospheric pressure plasma jet for plasma-polymerization of Hexamethyldisiloxane conjugated with (3-Aminopropyl) triethoxysilane” (November 24, 2017) **BK21+ 2017**, Jeju, Republic of Korea (**POSTER**).
11. Sudhakaran M.S.P, **Md. Mokter Hossain**, Sultana Lamia, Young Sun Mok, “SrNiO₃ perovskite catalyst for dry reforming of propane with heterogeneous support to produce syngas” (July 19-21, 2017) **ANM 2017**, Portugal (**POSTER**).
12. Sudhakaran M.S.P, **Md. Mokter Hossain**, Sultana Lamia, Young Sun Mok, “FeCe₂O₄ catalyst for dry reforming of propane to inhibition of carbon formation” (May 10-12, 2017) **KSIEC 2017**, Gwangju, Republic of Korea (**POSTER**).
13. Sudhakaran M.S.P, **Md. Mokter Hossain**, Sultana Lamia, Young Sun Mok, “FeCe₂O₄ catalyst for dry reforming of propane to inhibition of carbon formation” (May 10-12, 2017) **KSIEC 2017**, Gwangju, Republic of Korea (**POSTER**).
14. Sultana Lamia, Sudhakaran M.S.P, Md Shahinur Rahman, **Md Mokter Hossain**, Y.S. Mok, “Syngas production via dry reforming of propane over Ni supported on γ -Al₂O₃ modified with CeO₂ catalysts” (May 10-12, 2017) **KSIEC 2017**, Gwangju, Republic of Korea (**POSTER**).
15. Sudhakaran M.S.P, Duc Ba Nguyen, **Md. Mokter Hossain**, Sultana Lamia, Young Sun Mok, “SrNiO₃ perovskite catalyst for dry reforming of propane with heterogeneous support to produce syngas and physical-chemistry study” (November 24, 2017) **BK21+ 2017**, Jeju, Republic of Korea (**POSTER**).

